Thesis

Local Flow Manipulation by Rotational Motion of Magnetic Micro-Robots and Its Applications

Zhou Ye

Submitted in partial fulfillment of the requirements
for the degree of
Doctor of Philosophy
in
Mechanical Engineering

Carnegie Mellon University
Pittsburgh, PA

September, 2014

To my family...

Abstract

Magnetic micro-robots are small robots under 1 mm in size, made of magnetic materials, with relatively simple structures and functionalities. Such micro-robots can be actuated and controlled remotely by externally applied magnetic fields, and hence have the potential to access small and enclosed spaces. Most of the existing magnetic micro-robots can operate in wet environments. When the robots are actuated by the applied magnetic field to move inside a viscous liquid, they invoke flow motions around them inside the liquid. The induced flows are relatively local as the velocity of these flows decays rapidly with the distance from a moving robot, and the flow patterns are highly correlated with the motions of the micro-robots which are controllable by the applied magnetic field. Therefore, it is possible to generate local flow patterns that cannot be easily done using other microfluidic techniques.

In this work we propose to use rotational motion of the magnetic micro-robots for local manipulation of flows. We employ electromagnetic techniques to successfully deliver actuation and motion control onto the micro-robots. Rotational magnetic field is applied to induce rotational motion of micro-robots both when they stay near a surface and are suspended in the liquid. Rotational flows are locally generated in the vicinity of micro-robots inside the viscous liquid. Implementation of three major applications using the flows generated by the rotating micro-robots are demonstrated in this work: 1) Two-dimensional (2D) non-contact manipulation of micro-objects. 2) Three-dimensional (3D) propulsion for the micro-robot to swim in a liquid. 3) Size-based sorting of micro-particles in microfluidic channels under continuous flow. The first two applications occur in otherwise quiescent liquid, while the third requires the presence of non-zero background flow.

For the first application, we propose two methods to achieve precise positioning of the micro-robots on a surface: 1) Using visual-feedback-control to adjust the rotation for one single micro-robot. Micro-robot can be precisely positioned at any location on a surface using this method. 2) Using a specially prepared surface with magnetic micro-docks embedded in it, which act as local magnetic traps for multiple micro-robots to hold their positions and operate in parallel. Physical models are established for both the micro-robot and the micro-objects present in the induced rotational flow. The rotational flows induced by rotating micro-robots are studied with numerical simulations. Experimental demonstrations are first given at sub-millimeter scale to verify the proposed method. Micro-manipulation of polymer beads is performed with both position-control methods. Automated micro-manipulation is also achieved using visual-feedback. Micro-manipulation at micron-scale is then performed to demonstrate the scalability and versatility of the proposed method. Non-contact manipulation is achieved for various micro-objects, including biological samples, using a single spherical micro-robot.

Inspired by flagellated microorganisms in nature, we explore the hydrodynamics of an elastic rod-like structure - the artificial flagellum, and verify by both simulation and experiments that rotation and deformation of such structure can result in a propulsive force on a micro-robot it is attached to. Optimization of flagellum geometry is achieved for a single flagellum. A swimming micro-robot design with multiple flexible flagella is proposed and fabricated via an inexpensive micro-fabrication process involving photolithography, micro-molding and manual assembly. Experiments are perform to characterize the propulsive force generation and the resulting swimming performance of the fabricated micro-robots. It is demonstrated that the swimming speed can be

improved by increasing the number of attached flagella.

For the size-based sorting application, we integrate the micro-robots into microfluidic channels by using the substrate embedded with magnetic micro-docks, which are capable of holding the robots under continuous flow inside the channels while the robots spin. Numerical analysis is carried out of the flows inside the microfluidic channel in the presence of rotating micro-robots, and a physical model is established and discussed for size-based lateral migration of spherical micro-objects inside the induced rotational flows. Experimental demonstrations are performed for using the induced rotational flows to divert the trajectories of micro-particles based on their sizes under continuous flow.

In addition, we propose the method of using the two photon polymerization (TPP) technique to fabricate magnetic micro-robots with complex shapes. The method could also achieve fabrication of arrays of micro-robots for more sophisticated applications. However, experimental results prove that the TPP is insufficient to achieve magnetic micro-robots that meet our needs for size-based sorting application due to physical limitations of the materials. Despite that, it is potentially powerful and suitable for fabrication of micro-robots with complex structures at small scales.

Acknowledgments

I would like to thank my advisor and committee chair Metin Sitti for his support and advice during my pursuit of this PhD. He helped me develop the skills for research and provided opportunities for my PhD study. I would also like to thank my committee members Alan Russell, Gary Fedder and Anirban Jana for their time and guidance.

I first started my work at the NanoRobotics Lab under the guidance of Eric Diller. He provided great support when I encountered problems on research. My colleagues Shuhei Miyashita, Joshua Giltinan and Xiaoguang Dong have had numerous inspiring discussions with me to develop this work. Current and past members of the NanoRobotics lab have provided constant critique and ideas throughout my PhD study. My collaborator Collin Edington worked closely with me on the size-based particle-sorting project.

Some portion of this work was supported by the National Science Foundation under NSF-NRI Award Number 1317477.

Finally, I thank my parents Zhengguang Ye, Bing Xie, and my love Mengyuan Ni, for their endless support and love for me. Their constant encouragement has helped me overcome difficulties both in my study and in my life. I cherish their support and love.

Contents

List of Figures

List of Tables

Nomenclature

α_m	Mass ratio of Neodymium-Iron-Boron (NdFeB) particles and polymer in magnetic mixture
β	Angle between magnetization of micro-robot and the applied magnetic field
$\boldsymbol{\omega}$	Rotation vector of micro-robot
$\boldsymbol{\omega}_{\parallel}$	Rotation component of micro-robot parallel to bottom surface (rolling component)
$\boldsymbol{\omega}_{\perp}$	Rotation component of micro-robot perpendicular to bottom surface (spinning component)
$\boldsymbol{B}$	Magnetic field
$\boldsymbol{e}_{\theta}$	Unit vectors perpendicular to the vector from robot center to the point of interest in space
$\boldsymbol{e}_{l}$	Unit vector in the direction of l
$\boldsymbol{e}_{r}$	Unit vectors pointing in towards the point of interest in space
$\boldsymbol{f}_{\text{drag}}$	Viscous drag force on a translating cylinder inside liquid
$\boldsymbol{f}_{\text{vis}}$	Viscous drag force per unit length on a flagellum
$\boldsymbol{f}_{p}$	Propulsive force generated by a rotating flagellum
$\boldsymbol{F}_{bend}$	Bending force of a flagellum
$\boldsymbol{M}$	Magnetization vector of magnetic micro-robot
$\boldsymbol{M}_{\text{NdFeB}}$	Magnetization of a pure NdFeB material
$\boldsymbol{p}(s,t)$	Position vector at arc-length s and time t on a flagellum
$\boldsymbol{r}$	Distance from the robot center to the point of interest in space
$\boldsymbol{T}_{\text{drag}}$	Viscous drag torque on a rotating cylinder inside liquid
$\boldsymbol{T}_{\text{max}}$	Maximum applied magnetic torque
$\boldsymbol{T}_{\text{m}}$	Magnetic torque
$\boldsymbol{T}_{f}$	Viscous drag torque experienced by a rotating flagellum
$\boldsymbol{T}_{\text{d}}$	Drag torque from fluid
$\boldsymbol{T}_{\text{fric}}$	Spinning friction-based resistive torque
$\boldsymbol{u}_{\text{fg}}(s,t)$	Local instantaneous velocity of a flagellum
$\boldsymbol{v}_{\text{swim}}$	Swimming velocity of micro-robot

$\boldsymbol{v}_b$	Velocity of background flow
$\boldsymbol{v}_{flow}$	Flow velocity of a rotational flow field
ϵ	Gap between a particle and the near wall
γ_r	Shear rate along the radial direction of the flow
γ_z	Shear rate along the vertical direction of the flow
$\hat{\boldsymbol{z}}$	Unit vector in z-direction
μ	Dynamic viscosity of fluid
ω	Rotation speed of micro-robot
$\omega_\perp$	Magnitude of the rolling component
$\omega_\perp$	Magnitude of the spinning component
ϕ	Tilt angle of rotation axis from the horizontal plane
ρ_{NdFeB}	Density of NdFeB
ρ_{poly}	Density of polyurethane
ρ_{fl}	Density of fluid
ρ_{obj}	Density of an object
τ	Effective shear modulus between an object and the bottom surface
θ_f	Anchoring angle at the base of artificial flagella according to the long axis of the robot body
ξ^*	Drag coefficient for the flagellum including wall effects
ξ_∞	Drag coefficient for the flagellum without presence of walls
$\xi_\parallel$	Drag coefficient in the direction perpendicular to a slender body
$\xi_\perp$	Drag coefficient in the direction tangential to a slender body
A	Bending stiffness of a flagellum
a	Radius of an spherical object
a_f	Radius of a flagellum with circular cross-section
A_c	Contact area between an object and the bottom surface
a_{eff}	Effective radius of a flagellum with rectangular cross-section
b	Thickness of artificial flagella
$B_{\text{sept-out}}$	Magnetic field strength at step-out of micro-robot
c_{drag}	Drag coefficient on a cylindrical body
D	Diameter of cylindrical robot body
E	Young's modulus of material
f	Rotation speed of the micro-robot
F_{cp}	Centripetal force of an object orbiting a rotating micro-robot

F_f Surface friction between an object and the bottom surface

$F_{l(Poiseuille)}$ Lateral force experienced by a neutrally buoyant rigid spherical particle under a 2D Poiseuille flow inside a straight channel

$F_{l(wall)}$ Saffman force on a rigid spherical particle with the presence of a near wall

F_{lift} Inertia-induced lift force in vertical direction

F_{sl} Inertia-induced lift force due to Saffman effect

g Gravitational acceleration

G_b Buoyant weight of an object inside fluid

$G_{nominal}$ Nominal weight of a spherical object

gp Gap between micro-robot and the bottom surface

H Thickness of cylindrical robot body

L Length of artificial flagella

l Distance from the axis of the rotating cylinder to the point of interest

m Mass of an object

nu Kinematic viscosity of fluid

P Pull-off force for a sphere on a flat surface

R Radius of micro-robot

s Arc-length from the base on a flagellum

s_0 Offset distance from the base of artificial flagella to the long axis of the robot body

u^* Actual translational speed of micro-robot normalized by no-slip translational speed

$u_{\text{no-slip}}$ Ideal translational speed of a spherical micro-robot rolling on a surface without slippage

U_{cf} Maximum flow velocity inside the channel

u_c Local flow velocity at object center without presence of the object

u_{trans} Translational speed of micro-robot on a surface

V_{m} Volume of micro-robot

v_θ Flow velocity component of a rotational flow field in tangential direction

v_r Flow velocity component of a rotational flow field in radial direction

v_z Flow velocity component of a rotational flow field in vertical direction

v_{obj} Velocity of an object

w Width of artificial flagella

W_{adh} Work of adhesion

W_{ch} Width of the channel

x,y,z Cartesian coordinate directions

2D Two-dimensional

3D	Three-dimensional
Å	Length unit, equals to 10^{-10}m
A/m	SI unit of magnetic field strength or magnetization
FEA	Finite element analysis
MNP	Magnetic Nanoparticles
NdFeB	Neodymium-Iron-Boron alloy
Pa·S	SI Unit of dynamic viscosity
RMS	Root-mean-square
St	cgs unit of kinematic viscosity, Stokes
T	SI unit of magnetic flux density, Tesla
TPP	Two-Photon Polymerization

Chapter 1

Introduction

1.1 Motivation

Recent developments in microelectromechanical systems (MEMS) technology have enabled fabrication of mechanical structures that are only microns or even nanometers in size with various functionalities, such as actuation and sensing. With these functionalities at such small sizes, these structures enable many newly emerging applications in electronics, microfluidics and biomedicine. While most of such micro-devices have been designed to work without mobility, one exception - the untethered micro-robots, do have the capability to move themselves inside appointed workspaces to perform various tasks that cannot be achieved by others. Due to their high mobility and small size, these micro-robots could be potentially ideal for health care applications such as micro-surgery and targeted drug delivery inside human bodies.

While many existing micro-robots can work in both air and liquid, many of their poten-

tial applications happen in liquid environments, such as inside human bodies. Furthermore, liquids not only provide stronger damping to the motion of micro-robots than air to slow down their dynamics, but they also reduce impacts of stiction and adhesion, which together make real-time control of the robots' motion easier and more reliable. Therefore, most research efforts have been carried out for enabling micro-robots to perform various tasks inside liquids.

When a micro-robots moves in viscous fluidic environments, not only does it experience resistive drag forces and torques from the surrounding liquid, but in return it also disturbs the liquid by its motion, either creating flows in otherwise quiescent liquids or changing the existing flows from their original patterns near the robot's body. The flows generated by a micro-robot are highly correlated with the robot's motion, and hence it is possible to manipulate flows locally around the micro-robot by controlling its motion. Such interactions between robot's motion and the surrounding liquid can provide propulsion for the micro-robot equipped with specially designed propellers to translate inside the liquid. In addition, these interactions could affect objects appearing inside the disturbed flow region. Therefore, the micro-robots' overall functionality can be significantly enhanced by improving the capability of micro-robots to interact with liquid environments in a controllable manner to perform various tasks. While recent advances in related research have begun to explore the use of flows locally induced by robot's motion for object-manipulation and three-dimensional (3D) propulsion, a more comprehensive understanding of the underlying physics as well as real microfluidic and biomedical applications based on the mechanism are not yet developed.

Among various motions a micro-robot can possibly achieve, we are particularly inter-

ested in the rotational motion because it is straightforward to implement yet interesting from both actuation and fluid mechanics perspectives. This thesis concerns understanding the interactions between rotational motions of micro-robots and the surrounding Newtonian liquid, and based on such understanding further implementing micro-object manipulation, 3D micro-robot propulsion and biomedical and microfluidic applications such as particle-sorting.

1.2 Literature Survey

1.2.1 Micro-Robotics

Micro-robots are untethered, miniature robots that typically have characteristic lengths L less than 1 mm. The physics at such small scales is different from that at larger scales because surface effects begin to dominate volume effects. Surface effects are proportional to L^2 while volume effects to L^3. As L becomes smaller and smaller, the former decreases much less rapidly than the latter, and hence making surface effects more dominant. Due to such special physics at small scale, micro-robots require new approaches for actuation, power delivery and control that could be completely different from traditional robots at larger scales [1, 2]. Traditional untethered robots can be powered by various on-board batteries, while control of the robots is usually realized by a separate mechanism either on-board or off-board. However, the small size of micro-robots makes it currently impossible to fully integrate an actuation mechanism on the robot bodies with on-board power sources. The limited on-board space also makes it difficult to use a separate mechanism from actuation for motion-control purpose. Therefore, remote actuation methods have been chosen

as one of the most popular solutions for actuation of micro-robots while control of these robots is often integrated with actuation.

Different remote actuation methods have been developed for micro-robots to realize different motions. For operations on two-dimensional (2D) surfaces, micro-robots can be actuated and controlled by electrostatics [3, 4], electromagnetism[5, 6, 7, 8, 9], or laser thermal excitation[10, 11, 12]. All the above methods can achieve precise position control of individual micro-robots on planar surfaces while actuating the micro-robots. For 3D locomotion, micro-robots are often chemically[13, 14] or electromagnetically[15, 16, 17, 18, 19, 20, 21, 22] driven. Bacteria or other microorganisms can also be used to drive micro-robots both for 2D and 3D locomotions [23, 24, 25]. However, only electromagnetically driven micro-robots can be precisely steered to realize controllable 3D locomotion. The other actuation methods require additional control mechanisms to achieve fully steerable motions.

Potential applications of micro-robots can be found in various areas given their small size, high mobility and controllability, and the ability to access enclosed spaces. Micro-cargo transportation is one direct application that makes use of the mobility of micro-robots [26]. It could further lead to the medical application of targeted drug delivery inside human bodies [17]. Micro-robots can also perform micro-manipulation tasks [9, 12, 27, 28], or even built functional micro-structures from micro-parts [29]. Modular micro-robots themselves can also form larger, functional assemblies [30]. Besides these already mentioned applications, untethered micro-robots can be used to perform minimal-invasive micro-surgeries inside human bodies [20], which could potentially revolutionize medical surgeries in the future.

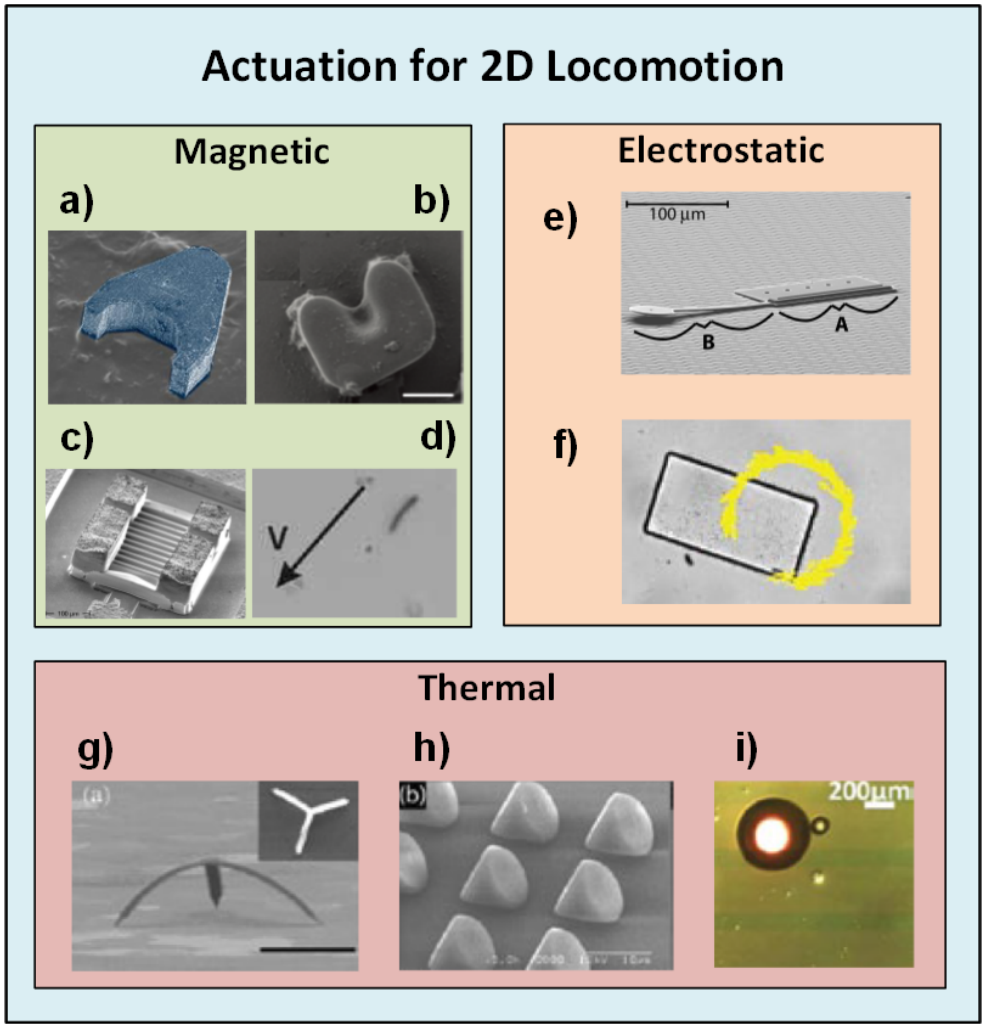

Figure 1.1: a) Mag-μBot [5]. b) Magnetic microtransporter [9]. c) Mag-Mite [6]. d) Magnetically-driven nano-wire [7]. e) Electrostatic scratch-drive micro-robot [3]. f) Electrostatic microrobot [4]. g) Thermal crawling micro-robot [10]. h) Light sailboat [11]. i) Optically controlled bubble microrobot [12]. Figures are reprinted from the references accordingly.

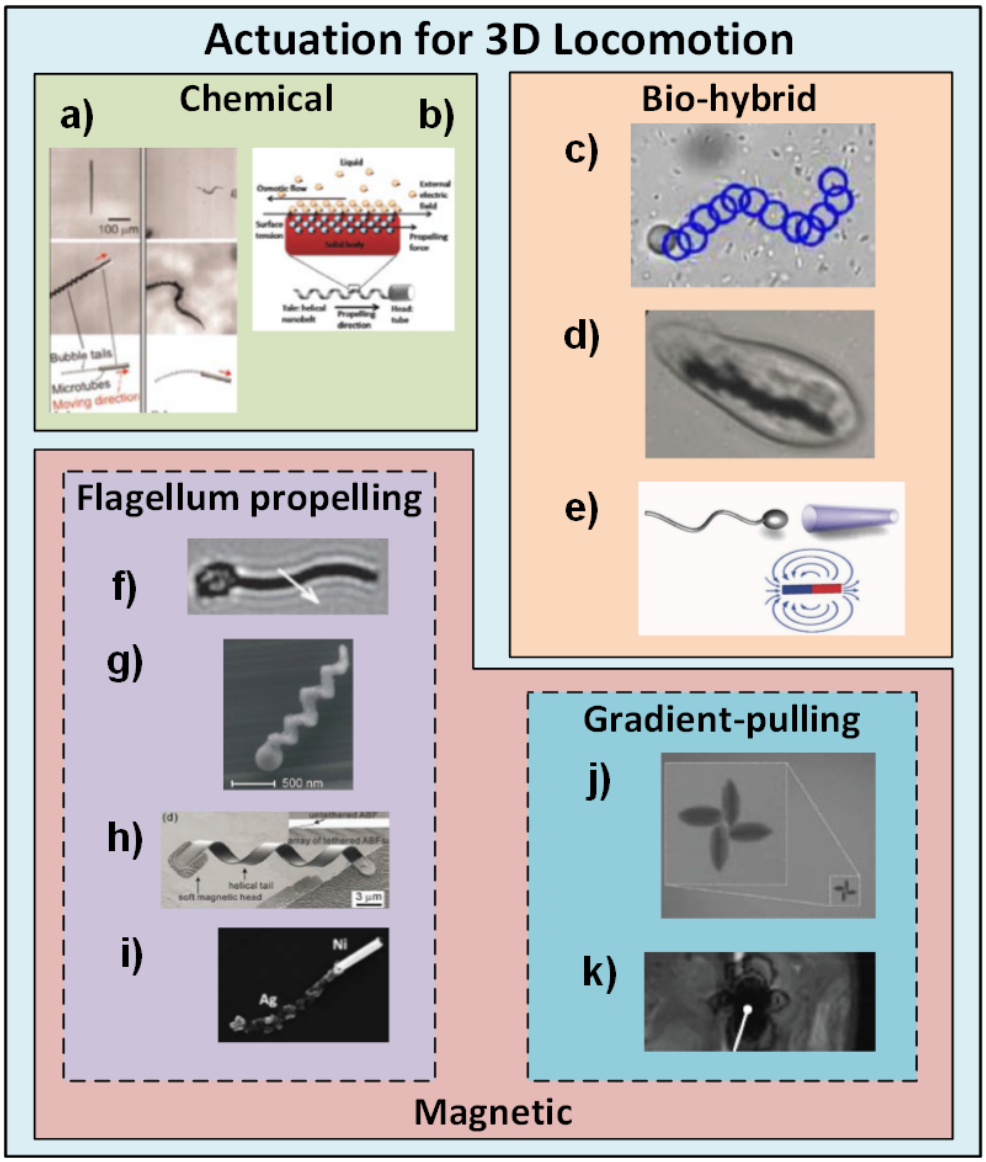

Figure 1.2: a) Microtubular jet engine [13]. b) Electro-osmotic swimmer [14]. c) Bacteria-propelled microbeads [23]. d) Artifically-magnetotactic bacteria [24]. e) Sperm-flagella driven micro-bio-robot [25]. f) Flexible artificial swimmer. [15]. g) Helical propeller [19]. h) Helical artificial flagella [18]. i) Flexible propeller [21]. j) Nickel micro-robot driven by OctoMag system in 3D [20]. k) MRI-powered and imaged magnetic bead [17]. Figures are reprinted from the references accordingly.

1.2.2 Non-Contact Micro-Manipulation

The ability to handle objects at the micron scale plays a crucial role in many fields including microfluidics, biological and colloidal science, lab-on-a-chip systems, and micro-assembly. To perform such micro-manipulation tasks, various techniques have been developed using different principles. Based upon whether or not physical contact occurs between the manipulator and the target micro-object during manipulation process, the existing manipulation methods can be classified into two fundamental categories: contact manipulation and non-contact manipulation. For contact-based manipulation, a manipulator needs to be physically present while micro-objects are handled by the manipulator via direct mechanical contact. Microgripper is the most commonly used device to perform contact-based manipulation [31, 32]. While conventional tethered microgrippers are widely adopted for many micro-manipulation tasks, new untethered micro-devices, such as micro-robots, have been developed for contact-based manipulation of micro-objects with much more flexibility and complexity [9, 29]. While high manipulation resolution can be achieved by contact-based manipulation, the mechanical contact between manipulator and object usually causes stiction, which could severely increases the difficulty for release of object. In addition, such mechanical contact could also cause advert effects or even physical damage to fragile objects such as some biological samples. Therefore, contact manipulation is generally applicable for micro-objects that will not be easily damaged or altered by any resulting contact forces during manipulation. Non-contact manipulation can overcome these disadvantages of contact-based manipulation. Instead of mechanical contact, non-contact manipulation is achieved by applying other forms of physical forces. Non-contact manipulation is necessary when relatively low to zero contact-forces are desired, or when the micro-objects are

fragile to physical contacts. For many biomedical applications in which fragile cells or tissues need to be handled, direct physical contact should be avoided. Therefore, non-contact manipulation methods would be more preferable for such applications.

Based on the various physical forces used, different non-contact manipulation techniques have been developed, including electrophoresis [33], dielectrophoresis [34], optical tweezer [35, 36], magnetic tweezer [37], acoustophoresis [38], vibration of surfaces [39, 40], bubbles [12, 41] and microfluidics [42, 43, 44]. Recently, magnetically driven micro-robots have shown potential capability of localized fluid flow control, which enables non-contact manipulation using these robots.[26, 27, 28] Many of these methods are performed in liquid environments due to physical constraints of the manipulation method. This would be a vital limitation if the micro-object cannot be immersed in a liquid. However, it is not an important drawback for bio-manipulation tasks as in such tasks the objects to be manipulated usually require a liquid environment.

Among all these non-contact manipulation methods, some can achieve fine manipulation resolution and selective manipulation of individual objects. These methods include optical tweezers, magnetic tweezers, bubbles and micro-robots. However, they are limited by their workspace, manipulation speed, and ability to manipulate many micro-objects in parallel. In addition, extra labeling on target objects is required to implement magnetic tweezers while photo-damage could occur on objects when using optical tweezers. The other methods can achieve simultaneous handling of a large number of micro-objects, but lack versatility due to their strict requirements for highly structured and specialized environments such as patterned surfaces or delicate 3D structures, which are not possible to reconfigure $in\ situ$ Further, it is usually difficult to use these methods for selective manip-

ulation of specific individual target micro-objects from a large sample.

1.2.3 Cell-Sorting

Separation of specific cell populations from a heterogeneous mixture plays an important role in biomedical research and cell-based diagnostics [45]. Many methods have been developed to achieve cell-sorting. Identifying cells by specific biological markers was mostly adopted in the earlier stages of development of cell-sorting techniques. Such methods that require additional markers include fluorescence-activated cell sorting (FACS) and magnetic-activated cell sorting (MACS). These label-based cell-sorting methods are relatively mature and can achieve very high throughput. Various FACS devices have been commercialized and hence are commonly used in many biomedical applications. The use of labels, however, introduces labeling and label-removal steps and can produce unintended adverse effects on the cellular phenotype [46].

On the other hand, recent development in microfluidic systems has enabled continuous flow manipulation at very small scales. This has given birth to many label-free cell-sorting methods which separate cells based on their intrinsic biophysical characteristics such as size, density, morphology and dielectric or magnetic susceptibility [47, 48, 49, 50]. In the microfluidic systems in which these methods are implemented, a separation force is usually applied at an angle to the direction of the flow. Cells in the heterogeneous mixture respond differently to this applied force based on their intrinsic properties, and hence can be separated continuously in the microfluidic systems. A wide variety of forces has been used for fractionation of the cell mixture. This includes the application of electric force (free-flow isoelectric focusing [51] and dielectrophoresis [52]), magnetic force (magnetophoresis

[53, 54]), acoustic force [55], and optical force [56, 57] The smart design of microfluidic channels [58, 59], and/or the introduction of flow obstacles [60] can also be used for sorting. These methods have demonstrated the capability to separate cells in a continuous manner based on their intrinsic properties, but are usually designed for separation of specific cells and thus are hard or even impossible to tune for other cells $in\ situ$.

1.3 Research Objectives

To utilize the rotational motion of magnetic micro-robots in liquids for various flow-manipulation applications, we first introduce the magnetic actuation methods to achieve controllable rotational motion of micro-robots both on a 2D surface and when suspended in liquid. Next, the hydrodynamics on the rotating magnetic micro-robots is analyzed using numerical simulations, as well as models of the induced rotational flows. We then further extend such numerical study to the fluidic forces experienced by micro-objects presented inside the induced rotational flow region. For 2D micro-manipulation tasks, we propose two methods to control position of the micro-robots, one for single spherical robot that takes advantage of the isotropy of spherical shape, the other using a specially prepared surface with local magnetic traps for both single and multiple robots. The behavior of the micro-objects in the rotational flows induced by a rotating micro-robot is analyzed theoretically and experimentally. To achieve size-based cell-sorting, we analyze the flow patterns inside microfluidic devices in the presence of spinning micro-robots by numerical simulations. Feasible micro-fabrication methods are proposed for the microfluidic devices and micro-robots. We demonstrate experimentally the applications of the rotating magnetic

micro-robots in 2D non-contact micro-manipulation, 3D propulsion generation in a liquid, and size-based micro-particle-sorting. In all these applications and explorations, we aim to understand the physical capabilities of the magnetic micro-robots to locally manipulate fluid using rotational motion.

The main objectives of this thesis work are:

• Implementing controllable rotational motion of magnetic micro-robots in wet environments based on the understanding of hydrodynamic interactions between rotating magnetic micro-robots, with or without artificial flagella attached, and the surrounding liquid.

• Understanding the rotational flows generated by the rotational motion of magnetic micro-robots without artificial flagella.

• Understanding the fluidic forces applied on the micro-objects by the rotational flows generated by rotating micro-robots without artificial flagella.

• Utilizing the above understandings as principles for implementation of non-contact micro-object manipulation, 3D micro-robot locomotion and micro-particle-sorting.

Thesis Organization

Chapter 2 introduces the concept of manipulating micro-objects using flows generated by rotational motions of micro-robots in liquid environments. Physical models are established to study the mechanism, and non-contact manipulation of various micro-objects at different scales are demonstrated by experiments. Chapter 3 introduces the use of rotating flexible artificial flagella as propeller to produce propulsion for 3D swimming of micro-robots in liquid. Both simulation and experimental results are presented. Chapter 4

introduces a size-based particle-sorting mechanism using the flow patterns induced by rotational motions of micro-robots. Simulations are carried out for disturbed flows inside microfluidic channel in the presence of rotating micro-robots, and experimental results of diverting polystyrene beads (PS) with different sizes into different trajectories are demonstrated. Finally, conclusions and future work are outlined in Chapter 5.

1.4 Contributions

The major contributions of this work lie in the development of method to locally manipulate fluid flows by rotating magnetic micro-robots. We incorporate small-scale physical theories and control methodologies to the micro-robotic system to achieve objectives for various applications. These objectives are explored through proof-of-concept experimental demonstrations.

In summary, this thesis provides contributions to the areas of micro-robotics, micromanipulation and microfluidics:

• Discovery of the object-trapping phenomenon inside rotational flows induced by rotating micro-robots at low Re regime.

▷ Numerical analysis of the flow field generated by rotational motion of micro-robots in a quiescent liquid.

▷ Theoretical analysis of the trapping force applied on the object by the induced rotational flows.

▷ Numerical analysis of the hydrodynamic interactions between the flows induced by robot's motion and any objects present in the flow region.

• Implementation of non-contact micro-manipulation using robot-motion-induced flows on a planar surface for various micro-objects at different scales.

▷ Characterization of the dynamic locomotion of mobile magnetic micro-robots induced by rotational motion.

▷ Development of a magnetic platform for powering and controlling untethered magnetic micro-robots with size less than 50 μm.

▷ Implementation of visual-feedback assisted automated non-contact micro-object delivery using robot-motion-induced flows on a planar surface.

• Implementation of 3D micro-robot locomotion using multiple rotating flexible flagella.

▷ Fabrication of magnetic micro-robots with multiple flexible artificial flagella attached via a new, two-step process involving photolithography, micro-molding and manual assembly.

▷ Modeling of magnetic micro-robot with an artificial flagellum attached swimming in viscous liquid.

▷ Design optimization for straight flagellum design to maximize propulsive force generation.

• Implementation of size-based particle-sorting using rotational flow induced by spinning magnetic micro-robots inside microfluidic channels.

▷ Numerical study of the flow patterns altered by rotational motion of micro-robots inside microfluidic channels in continuous flow.

▷ Development of magnetic docking substrate to hold magnetic micro-robots in place under flow during spinning.

Chapter 2

Rotational Flows Induced by Magnetic Micro-Robots for 2D Non-Contact Micro-Manipulation

2.1 Introduction

Recent development in micro-robotics have enabled new manipulation schemes in addition to the existing micro-manipulation methods [9, 12, 26, 28, 29]. Many of the currently available untethered micro-robotic systems can be used to manipulate micro-objects in their environments, and are usually operated in wet environments due to environmental requirements of the micro-robots themselves [12, 17, 18, 61, 62]. Because local flows can be generated in these environments, micro-object manipulations can be performed even without mechanical contact be-

tween the robots and objects, which can be useful for the manipulation of fragile objects and to achieve precise positioning. Previous work has successfully utilized flows induced by translational motion of magnetic micro-robots for serial non-contact micro-manipulation on planar surfaces [63]. However, such method lacks efficiency because the micro-object has to be carried to the destination in an iterative manner. Parallel manipulation is also difficult to achieve using this method. Therefore, a better non-contact micro-manipulation mechanism using magnetic micro-robots should be developed.

We notice that a rotational flow field can be induced by a micro-robot's rotation in otherwise quiescent liquids, which is possibly usable for non-contact micro-manipulation at low Reynolds number (Re). Based on the observation, we further develop a non-contact micro-manipulation method using a single spherical magnetic mobile micro-robot to enable fast, high precision, and long distance 2D non-contact manipulation of micro-objects with versatility in liquid environments. When an object with proper size and shape is present inside the rotational flow induced by the rotating magnetic micro-robot on a substrate, it will be trapped in the flow region and orbit around the rotating micro-robot. As long as such rotational flow is maintained while the micro-robot translates on a surface, the object will be carried along with the micro-robot and hence makes object-manipulation possible. This mechanism could be applicable for a wide range of micro-objects, including both biological and non-biological samples. Automated delivery of micro-objects based on this mechanism is also possible with the assistance of visual feedback.

In addition to micro-manipulation of individual micro-objects, multiple magnetic

micro-robots can work in a team to transport multiple objects simultaneously by introducing a specially prepared surface to hold the robots in place. Multiple micro-robots are fixed at prescribed positions on the surface by magnetic micro-docks embedded in the surface, and then rotate in synchrony by the externally applied magnetic field to generate rotational flow fields around each robot, which together form virtual fluidic channels (VFC's). Micro-objects present in the flow region can then be carried through these VFC's by the liquid. The pattern of VFC's are associated with the positions of the micro-robots, which can be adjusted $in\ situ$.

2.2 Concept

The magnetic micro-robot is capable of displacing micro-objects in wet environments by non-contact manipulation using rotational flow induced by its rotational motion. When the micro-robot rotates about an axis perpendicular to the underlying substrate, it generates a rotational flow field around it which has the same rotation axis. Such flow field applies drag forces to other objects in the disturbed liquid, pushing them to orbit around the rotating robot. For objects with proper sizes and distance from the robot, they will remain in relatively stable orbits around the micro-robot. When such a micro-robot translate on the substrate, the trapped micro-objects could possibly be carried along with the micro-robot if the induced rotational flow remains functional, which makes non-contact manipulation of micro-objects feasible.

2.2.1 Single Rotating Magnetic Micro-Robot

Control of the position of the micro-robot on a 2D surface can be achieved by varying the magnetic field rotation axis as shown in Fig. 2.1. Normally, the micro-robot rotates about an axis perpendicular to the substrate. To induce translational robot motion, the rotation axis is tilted from vertical by a small angle ϕ, creating a component of rotation $\boldsymbol{\omega}_{\parallel}$ parallel to the substrate. This parallel component results in translational locomotion of the magnetic micro-robot on the substrate via friction, while the remaining perpendicular component $\boldsymbol{\omega}_{\perp}$ generates the rotational fluid flow for micro-object manipulation. The perpendicular spinning rate $\omega_{\parallel}$ of the robot determines the rotational flow velocity of the surrounding flow field. Due to the low Re condition, the circulating speed of the micro-object around the robot is linearly proportional to the rotational flow velocity. In this way, coarse and fine manipulation of the object can be achieved by controlling the rotation speed of the micro-robot. After the object is placed at the target position, pure rolling is applied ($\omega_{\perp} = 0$) for the robot to slowly roll away from the object without disturbing the positioned object.

2.2.2 Magnetic Micro-Docks for Multiple Magnetic Micro-Robots

If multiple micro-robots can spin close to each other simultaneously and stably on a substrate, special flow patterns, which are defined as VFC's, can be generated to transport micro-objects. To achieve precise position control of multiple micro-

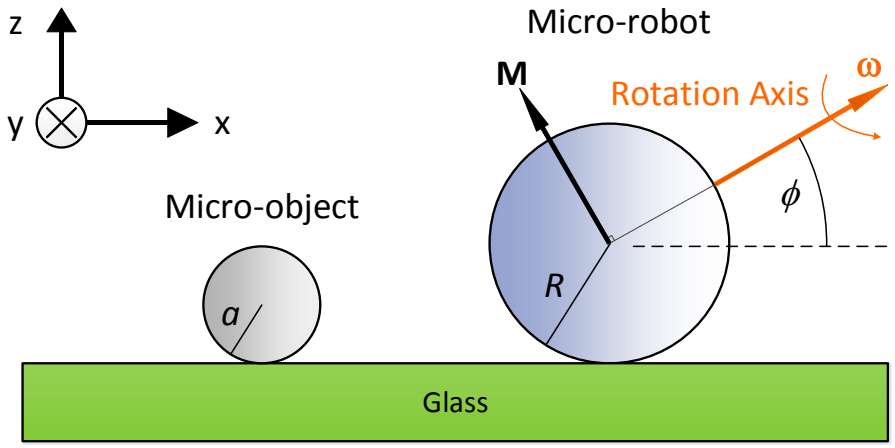

Figure 2.1: Schematic of a rotating micro-robot. The micro-robot rotates with speed ω about a rotation axis $\boldsymbol{\omega}$, which is tilted from the horizontal plane by a tilt angle ϕ. The rotation $\boldsymbol{\omega}$ is a combination of pure spinning ($\phi = 90°$) and pure rolling ($\phi = 0°$). $\boldsymbol{M}$ denotes the magnetization vector of the micro-robot, which rotates along with the robot body about the same rotation axis.

robots, a special substrate with magnetic micro-docks embedded in prescribed positions is used. The micro-docks act as magnetic traps for the magnetic micro-robots, as shown in Fig. 2.2. First, each magnetic robot, one after another, is moved towards a target micro-dock by a previously demonstrated method [5]. After multiple robots are trapped in fixed positions by the micro-docks, all robots are driven simultaneously by an applied rotating magnetic field to form the VFC's. Unlike the single micro-robot case, the micro-robots used here don't necessarily need to be spherical because the translation of micro-robots is a separate process from generation of the rotational flows in this case. Therefore, the trapped micro-robots can be independently addressed to new positions by a previously demonstrated multi-robot control method [64], and hence the virtual fluidic channels are reconfigurable during operation. In short, this method relies on micro-robots with slightly different magnetization values to achieve independent addressing using low-strength rolling magnetic fields. This relies on the unique magnetization values being separated at least by a factor of roughly 10%. In order to maintain a large level of magnetic torque for spinning actuation, the magnetization values are kept as high as possible while maintaining addressability. In low Re environments, the flow velocity of the flow field generated by multiple micro-robots can be approximated by the linear superposition of the flow fields generated by each single magnetic micro-robot. This means that results from the study of single robot can be straightly extended to the case of multiple robots without much modification.

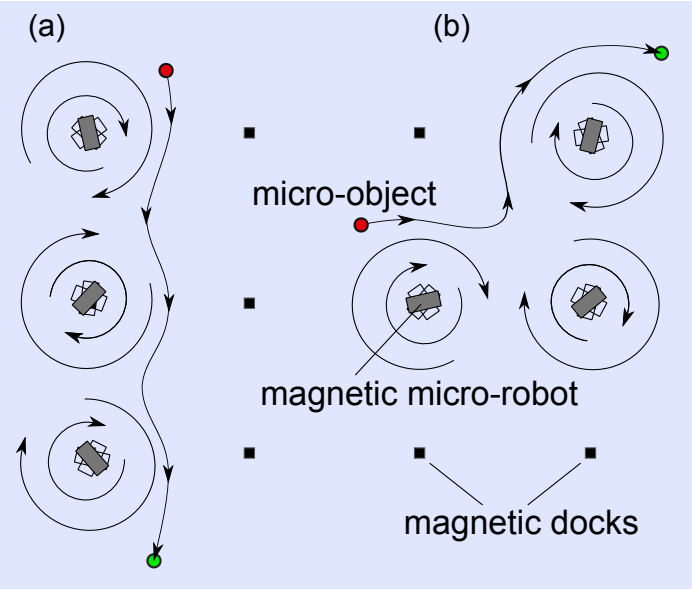

Figure 2.2: Magnetic dock concept to create reconfigurable virtual flow channels by multiple magnetic micro-robots. The array of docks is embedded in the surface and acts to trap spinning micro-robots at prescribed locations to achieve controlled parallel fluid-based manipulation of micro-objects along straight (a) or more complex (b) paths.

2.3 Experimental Setup

2.3.1 Experimental Platform for Magnetic Micro-Robots

Magnetic micro-robots are actuated by electromagnetic-coil systems. There are two sets of systems for micro-robots with different sizes.

The first system is used for actuation of micro-robots that have characteristic length larger than 50 μm. It consists of six electromagnetic coils that are independently powered by six motor drivers (Syren 25, Dimension Engineering LLC) (see Append. A.1). Imaging of the magnetic micro-robots and workspace is accomplished by a CCD camera (Foculus F0134SB) connected to a variable magnification microscope lens, providing up to a 26 mm×20 mm field of view. Magnetic flux densities of up to 15 mT can be generated in the workspace. For a 20 mm×20 mm workspace in the center of the coil system, the magnetic field is measured with a Hall effect sensor to be uniform within 6.0% of the nominal value. Sinusoidal current waves with the same intensity are passed through these coils with phase differences in each coil to generate an uniform rotating magnetic field inside the workspace. The magnetic micro-robot that is exposed to this rotating magnetic field will tend to orient its magnetization in the direction of the net magnetic field, and hence rotates with the field. The rotation rate of the magnetic micro-robots can be up to 120 Hz inside a liquid with dynamic viscosity of less than 50 cSt.

The second system is designed for actuation of micro-robots that have characteristic length less than 50 μm. It consists of three sets of electromagnets for in-plane and out-of-plane fields respectively (see Append. A.2). Two pairs of iron-cored elec-

tromagnets that are perpendicular to each other are used to generate in-plane fields, while the out-of-plane field is generated by a third vertically placed solenoid. The coil system is built onto a microscope stage insert so that it could be placed into an inverted microscope (Axio Observer, Carl Zeiss) rigidly. Each pair of the iron-cored electromagnets is powered by a motor driver (Syren 10, Dimension Engineering LLC), while the vertically placed solenoid is powered by a third motor driver with the same type. A maximum in-plane magnetic field of 3.5 mT can be achieved, with a maximum out-of-plane magnetic field of 8 mT. The in-plane magnetic field is measured to be uniform within 7.5% of the nominal value. The rotation rate of the magnetic micro-robots can be up to 150 Hz inside water.

Experiments for sub-millimeter scale micro-robots were carried out in a container of 50 mm×30 mm×1 mm filled with silicone oil. The container consists of a glass bottom substrate and sidewalls made of thermalplastic (ethylene-vinyl acetate hot-melt adhesive). Experiments using micro-robots less than 50 μm were performed in a 5 mm×5 mm×2 mm chamber constructed from a polydimethylsiloxane square frame sandwiched between two glass coverslips.

2.3.2 Preparation of Spherical Magnetic Micro-Robot

Two different methods have been used to obtain spherical magnetic micro-robots at different scale for different experimental purposes in this work.

For sub-millimeter spherical magnetic micro-robots, they were produced in a batch process using a micro-molding technique. The positive shapes for the spherical micro-robots were made from a small drop of solder dropped into water. Many

solder spheres ranging from 10 μm to 1000 μm were fabricated in this manner, and the desired sizes were selected from the batch. These solder spheres were glued to a glass substrate using a UV curable epoxy (Loctite 3761) and a moldmaking elastomer (PDMS, Dow Corning HS II RTV) was poured over to form a negative mold. The magnetic micro-robots used in this work were composed of a mixture of neodymium-iron-boron (NdFeB) particles (Magnequench MQP-15-7, refined in a ball mill to produce particles under 2 μm in size) suspended in a polyurethane (TC-892, BJB Enterprises) matrix. This magnetic slurry was poured into the negative rubber mold and allowed to cure into the final micro-robot shapes. The cured micro-robots were eventually magnetized individually by a magnetic field of 1 mT provided by a strong permanent magnet and ready for experiments. A spherical magnetic micro-robot used in this work is shown in Fig. 2.3 (a), with a diameter of 360 μm.

Spherical magnetic micro-robots that are a few to tens of microns in size were obtained via filtering the spherical NdFeB powder (MQP-S-11-9-20001-070, Magnequench International, Inc.) that were provided unmagnetized and ranging in size from 2-100 μm in diameter. First, a scoop of powder was passed through a series of sieves with decreasing meshes of 63 μm, 45 μm, 32 μm, and 20 μm (3 Inch Test Sieves, H&C Sieving Systems). The residuals on each sieve were collected as potential spherical micro-robots with a specific size range. To obtain even smaller spherical micro-robots, the particles that made their way through the 20 μm sieve were further filtered by membrane filters with pore size 5 μm (K50CP04700, Osmonics, Inc.) and 3 μm (K30CP02500, Osmonics, Inc.) sequentially. The residues on the 3-μm membrane filter were then collected as potential spherical micro-robots

with diameters of 4 ± 1 μm. The particles were kept unmagnetized before experiments to prevent aggregation. A sample of the filtered NdFeB particles is shown in Fig. 2.3 (b). When ready for experiments, a small amount of filtered NdFeB particles within a proper size range were injected into the experimental container and sparsely distributed in it. A magnetic field of 0.3 mT provided by a strong permanent magnet was then applied onto the whole container shortly to magnetize the particles so that they could respond to magnetic actuating signals and act as magnetic micro-robots.

Table 2.1: Material properties of NdPrFeCoTiZrB alloy powder, adapted from the Magnequench material data sheet available online (MQP-S-11-9-20001-070).

Material Property (NdFeB Microspheres)	Value	Units
Residual Induction, B_r	730-760	mT
Energy Product, $(BH)_{max}$	80-92	kJ/m^3
Intrinsic Coercivity, H_{ci}	670-750	kA/m
Coercive Force, H_c	440	kA/m
Magnetizing Field to $>95\%$ Saturation, H_s	$\geq$1600	kA/m
Density (theoretical)	7.43	g/cm^3
Apparent Density	3.6-4.2	g/cm^3

2.3.3 Fabrication of Magnetic Micro-Dock

A surface patterned with magnetic micro-docks is shown in Fig. 2.3 (c). This surface consisted of a 200 μm thick layer of SU-8 photoresist patterned on a glass substrate using photolithography to have a number of cylindrical cavities all the way to the

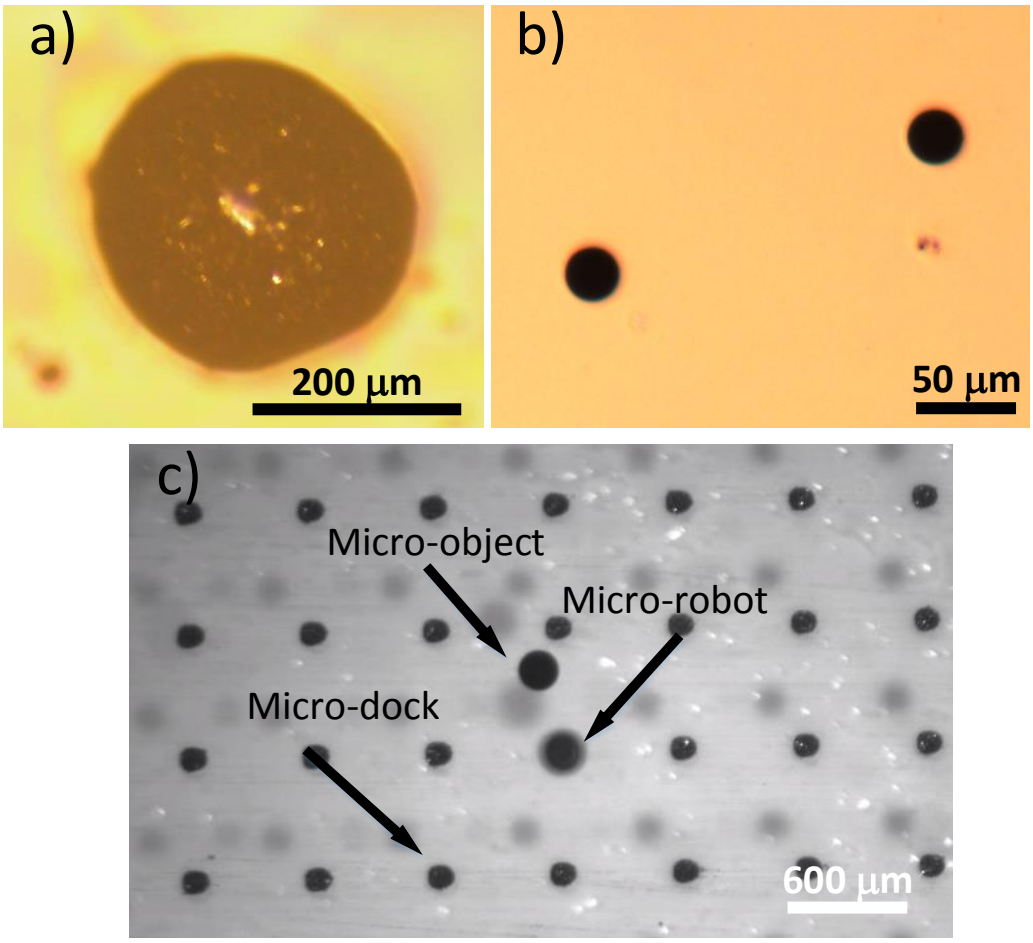

Figure 2.3: a) Optical microscope view of a molded spherical magnetic micro-robot. In this image, two images from two different focal planes are combined so that the entire sphere is in focus. b) Optical microscope view of a sample of filtered spherical NdFeB particles. c) Top view optical microscope image of a $200\times200\times200$ μm rectilinear spinning robot is shown manipulating a 200 μm diameter micro-sphere. The micro-robot is constrained on one of the cylindrical magnetic micro-docks which have a radius of 110 μm, depth of 200 μm and spacing of 600 μm.

glass. These holes are filled with the same magnetic slurry used to fabricate the robots and covered with a thin 10 μm layer of spin-on-glass (Filmtronics 21F) to ensure a flat surface. The cylindrical magnetic micro-docks used in this work each has a radius of 110 μm, depth of 200 μm, and spacing of 600 μm.

2.4 Modeling

2.4.1 Actuation of Spherical Magnetic Micro-Robots

Actuated by external magnetic fields, a magnetic micro-robot will potentially experience electromagnetic, gravitational, adhesive, frictional, and fluidic forces applied from the environment. The effects of these forces are explained in detail in [5, 27]. This subsection provides a brief derivation of the forces and torques relevant to the rotational motion of the spherical magnetic micro-robots.

The magnetic torque $\boldsymbol{T}_{\mathrm{m}}$ acting on a magnetic micro-robot drives it to rotate with the applied magnetic field. This torque is a function of volume V_{m} and magnetization $\boldsymbol{M}$ of the robot, as well as the applied magnetic flux density $\boldsymbol{B}$:

$$\boldsymbol{T}_{\mathrm{m}} = V_{\mathrm{m}} \boldsymbol{M} \times \boldsymbol{B}. \tag{2.1}$$

For sub-millimeter micro-robots, the robot body is made of a composite of magnetic NdFeB particles and polyurethane. Therefore, its magnetization would be different from a pure magnetic material. As the mass ratio of NdFeB particles and polymer in the mixture, α_m, can be adjusted during fabrication process, the magne-

tization can be determined as

$$\boldsymbol{M} = \frac{\boldsymbol{M}_{\text{NdFeB}}}{1 + \rho_{\text{NdFeB}} / \left(\alpha_m \rho_{\text{poly}}\right)}, \tag{2.2}$$

where ρ_{NdFeB} and ρ_{poly} are the densities of NdFeB and polyurethane, respectively, and $\boldsymbol{M}_{\text{NdFeB}}$ is the magnetization of a pure NdFeB material.

When rotating in a liquid, the spherical magnetic micro-robot also experiences viscous fluidic drag torque applied from the surrounding liquid, and the proximity of the substrate surface acts to increase the drag torque compared to the free liquid case [65]. Under the Stokes flow assumption and assuming the distance between the micro-robot and surface is very small, this drag torque T_{d} has been found to be [66]:

$$\boldsymbol{T}_{\text{d}} = -8\pi\mu R^3 \boldsymbol{\omega} \left[1.20 - 3\left(\frac{\pi^2}{6} - 1\right)\frac{gp}{R}\right], \tag{2.3}$$

where μ is the fluid viscosity, R is the micro-robot radius, $\boldsymbol{\omega}$ is the rotation rate vector in rad/s, and gp is the gap between the robot and the surface. For a spherical micro-robot in contact with the wall ($gp = 0$), this represents a 20% increase in torque over the free-liquid case.

A spherical micro-robot rotates synchronously with the applied field at a given ω when it is torque-free:

$$\boldsymbol{T}_{\text{m}} = \boldsymbol{T}_{\text{d}} + \boldsymbol{T}_{\text{fric}}, \tag{2.4}$$

where $\boldsymbol{T}_{\text{fric}}$ is the spinning friction-based resistive torque (only nonzero when $gp = 0$), analyzed in [67]. Because the magnetic micro-robot is assumed to contact with a point or very small contact area while spinning, the moment arm of this point of contact about the center of mass will be small, leading to a negligible $\boldsymbol{T}_{\text{fric}}$.

Using eqns. (2.1) and (2.4), a balance of torques can be determined for the steady-state case where the micro-robot magnetization lags the applied field $\boldsymbol{B}$ by the angle β. If $|\boldsymbol{B}|$ is too small, the critical value $\beta_{\mathrm{c}} = 90^{\circ}$ is exceeded and the torque balance (eqn. (2.4)) cannot be met, resulting in step-out of micro-robot at

$$B_{\text{step-out}} = \frac{|\boldsymbol{T}_{\mathrm{d}} + \boldsymbol{T}_{\text{fric}}|}{V_{\mathrm{m}} M \sin \beta_{\mathrm{c}}} = \frac{|\boldsymbol{T}_{\mathrm{d}} + \boldsymbol{T}_{\text{fric}}|}{V_{\mathrm{m}} M}. \tag{2.5}$$

For $|\boldsymbol{B}| > B_{\text{step-out}}$, the micro-robot will rotate synchronously with the field with a lag of β, but the micro-robot will exhibit erratic oscillating motion for $|\boldsymbol{B}| < B_{\text{step-out}}$. It can be seen from eqn. (2.5) that $B_{\text{step-out}}$ increases with ω due to the increase in T_{d}.

When a spherical micro-robot rotates in synchrony with the external rotating magnetic field with a tilt angle ϕ on a substrate, it will reach a steady-state translational speed. Such translational speed u_{trans}, assuming that the micro-robot does not slip on the surface is given by

$$u_{\text{no-slip}} = \omega_{\parallel} R = \omega R \cos \phi. \tag{2.6}$$

However, when a robot moves in a wet environment at small scales, slippage is very likely to occur, and could even be significant. A dimensionless micro-robot translational speed is defined by normalizing the actual speed by the no-slip velocity

$$u^{*} = \frac{u_{trans}}{u_{\text{no-slip}}} = \frac{u_{trans}}{\omega R \cos \phi}, \tag{2.7}$$

allowing direct comparison between all micro-robot sizes and rotation speeds, as well as providing a clear indication of the level of slippage.

2.4.2 Rotational Flows Induced by Spherical Micro-Robots

Understanding the flow field generated by a rotating magnetic robot, particularly in the steady-state, is crucial for implementing the micro-manipulation mechanism. Such understanding can be readily extended to multiple-robot cases by linear superposition given the linearity of fluid flows in the low Re regime. Stokes flow analytical solutions for the local flow velocity are available for the case of a sphere rotating in an unbounded liquid [68]:

$$\boldsymbol{v}_{flow} = \omega_{\perp} R \left(\frac{R}{r}\right)^2 \boldsymbol{e}_r \times \boldsymbol{e}_{\theta}, \tag{2.8}$$

where r is the distance from the sphere center to the point of interest and $\boldsymbol{e}_r$ and $\boldsymbol{e}_{\theta}$ are unit vectors pointing in towards and perpendicular to the point of interest, respectively.

However, the presence of the underlying substrate retards the fluid flow and thus significantly changes the flow field from the Stokes flow case. In such a case, no analytical solutions are available. Therefore, finite-element simulations (details in Append. B.1) were first carried out for the case of a 360 µm-diameter sphere spinning at $|\omega_{\perp|} = 60$ Hz on the bottom surface of a 50 mm×30 mm×1 mm container filled with liquid of kinematic viscosity 50 cSt (rotational Re of the robot was 0.24). High viscosity oil was chosen to satisfy the low Re requirement, as well as to keep the results valid for smaller size micro-robots. The results, presented in Fig. 2.4 (a), show a steady-state flow velocity taken from the equatorial plane of the rotating sphere with a power law flow velocity fall-off on the plane fitted from the data as

$$|\boldsymbol{v}| = \omega_{\perp} R \left(\frac{R}{r}\right)^{2.43}. \tag{2.9}$$

Results of multiple simulations with variations either in viscosity or sphere size validate this relationship and demonstrate that eqn. (2.9) is valid in the Re< 1 regime. Comparing eqns. (2.8) and (2.9), we notice that the exponent is larger in the bounded liquid case, which means a faster flow velocity decay. This reflects the retarding effect of the underlying substrate as well as the sidewalls of the container on the induced flows.

The streamlines of the rotational flows induced by the spinning sphere from the same simulation are shown in Fig. 2.5 (a). The streamlines are mainly circumferential, indicating that the tangential components of flow velocity are dominant. Non-tangential velocity components, the radial (v_r) or vertical (v_z) velocity components, can be significant when inertial forces becomes comparable to viscous forces for Re approaching unity and beyond. As shown in Fig. 2.5, the liquid in the neighborhoods of the poles of the sphere is drawn towards its equator following spiral paths [65], with the developed flows being ejected away from the sphere close to its equator. However, this equatorial flow ejection, which results from inertial effects, becomes small compared to the circumferential flow velocity v_θ as Re becomes smaller than unity. Finite element analysis shows that for the range of Re considered here in this work (Re< 1), the relative magnitude of the radial component is $v_r/v_\theta < 0.01$, indicating that the radial flow, and hence the corresponding radial fluidic viscous drag, is negligible when analyzing the behavior of the objects during manipulation.

When the micro-robot translates on the substrate, a tilt angle ϕ slightly deviated from 90° is required to simultaneously achieve translational motion and generation of local flows, and hence the flow field generated in this case would be different

from that induced by a purely spinning robot. To further investigate how the flow field would be modified by the translational motion of the micro-robot, another simulation was carried out (detailed in Append. B.2). In this simulation, a spherical micro-robot with a diameter of 5 μm rotated at 100 Hz with a tilt angle $\phi = 75^\circ$ near a bottom surface. A background flow velocity of $0.06\omega_\parallel R$ in negative y-direction was added to include the effect of translation of micro-robot. Due to the linearity of low Reynolds-number flows, the flow field could be treated as a linear superposition of the flows induced by $\omega_\parallel$, $\omega_\perp$, and the translational motion of the micro-robot. At large tilt-angles, the spinning component is more dominant. For example, at $\phi = 75^\circ$, $\omega_\parallel/\omega_\perp = \cos\phi/\sin\phi = 0.27$. Further, the translational speed resulting from $\omega_\parallel$, due to significant slippage, was much less than when there is no slippage, and hence the flows induced by such translational motion was far less significant than those induced by rotational motion of the micro-robot, especially at high rotation speeds. The simulation results shown in Fig. 2.5 (b) indicate that the flows are mostly circulating the rotating micro-robot, while there exist out-of-plane velocity components arising from the rolling component of rotation. However, these components are relatively insignificant compared to the circulating flows especially at distance about $1.5R$ from the robot, as shown by the normalized out-of-plane velocity components w^*. Therefore, the flows induced by the spinning component dominate in the flow field, which enables stable trapping of micro-objects during translation of micro-robot.

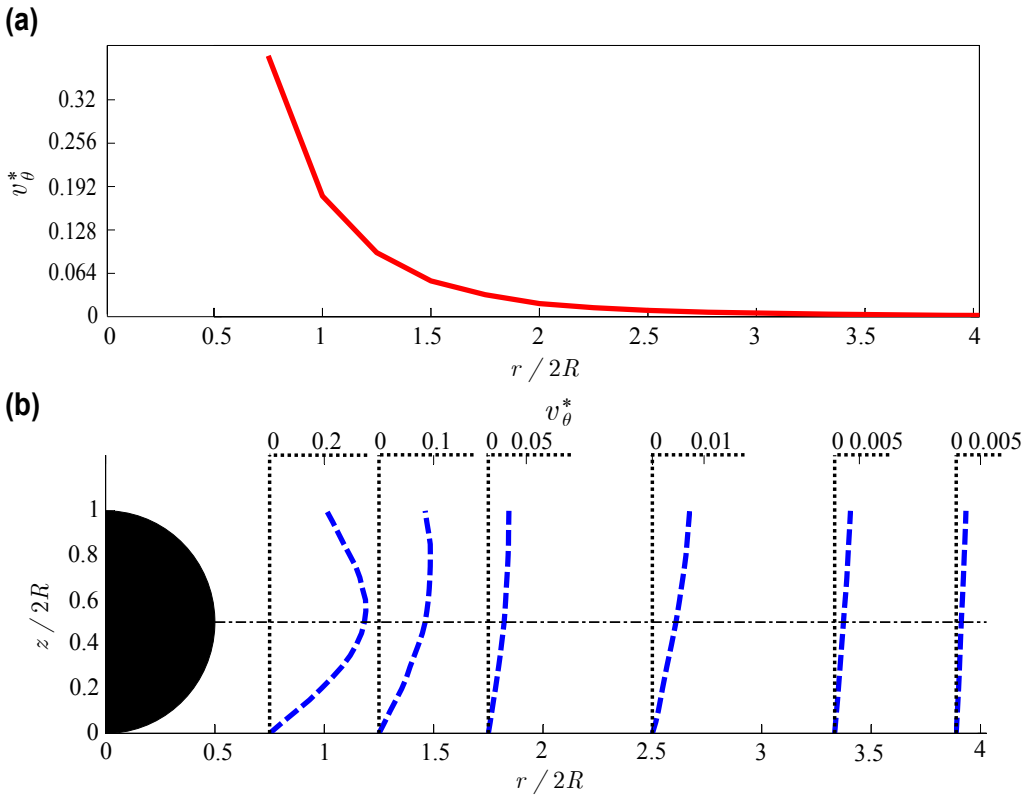

Figure 2.4: Tangential velocity (v_θ) data from finite-element simulations taken from a half $x-z$ plane ($z/2R \in [0,1]$) which cuts through the cross-section of the spinning sphere (represented by the solid dark semicircle in the figure). All velocities are normalized by the linear speed of the spinning sphere at its equator ($\omega_\perp R$) as v_θ^*. a) The solid curve shows v_θ^* as a function r at $z/2R = 0.5$ (the equator plane of the robot). The curve indicates a power law fall-off of v_θ^* with resp ect to r, and a fit to the data from the curve is given by eqn. (2.9). b) v_θ^* vs. height z , is given at some selected distances r, showing the profile evolving from highly nonlinear in the neighborhood of the sphere to linear far from the robot. The tangential velocity data used to plot the curves are scaled with different scaling factors, which is 20 at the smallest r, 40 at the larger two r's, and 200 at the largest three r's.

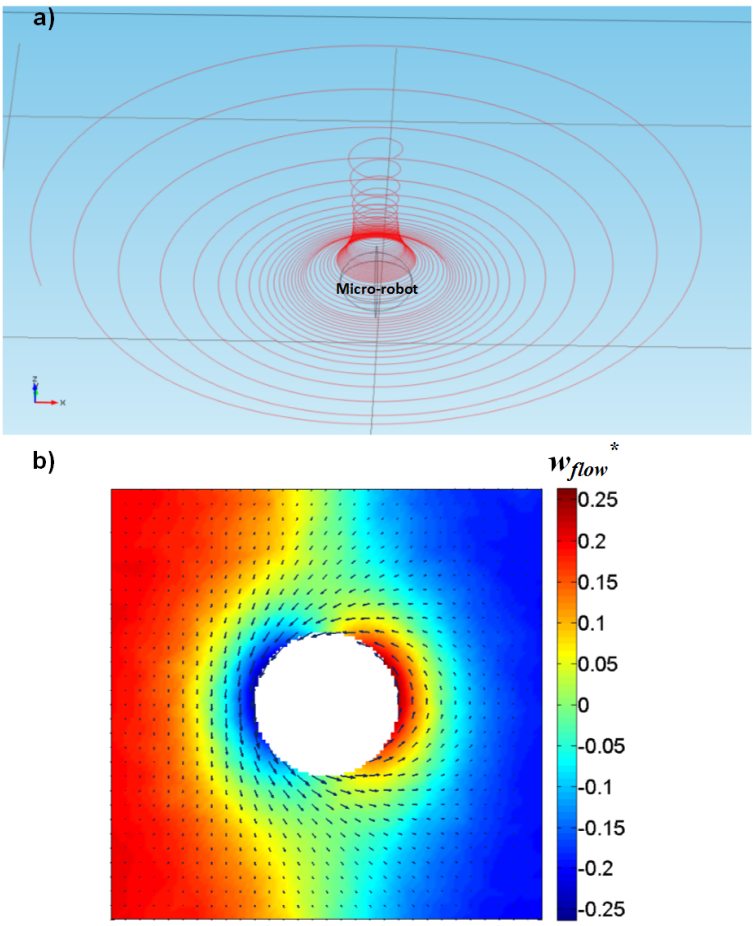

Figure 2.5: Rotational flow induced by rotating spherical micro-robot near a surface. a) Streamlines of rotational flow induced by a 360-µm-diameter sphere spinning at 60 Hz in a liquid with a viscosity of 50 cSt. b) Rotational flow induced by a 5-µm-diameter sphere rotating at 100 Hz with a tilt-angle of $\phi = 75°$ and a translational speed of $0.06\omega_{\|}R$ in y-direction in water. The plot is from a top-view of the cross-section taken at the equatorial plane of the sphere. The arrows indicate the in-plane flow velocity at selective positions, while the color map shows the distribution of out-of-plane flow velocity normalized by the magnitude of in-plane flow velocity at the same position.

2.4.3 Rotational Flows Induced by Non-Spherical Micro-Robots

Spherical micro-robot is ideal for dynamic non-contact micro-manipulation because its rotation can both induce rotational flows for object-manipulation and create translational motion of robot itself simultaneously. Besides spherical shape, micro-robots with other shapes can also be used to generate rotational flows by spinning. For non-spherical micro-robots, controllable translational motion of robots and generation of rotational flows for manipulation cannot be achieved at the same time. Therefore, other types of position control methods, such as the magnetic micro-dock concept introduced in previous section (Sec. 2.2.2), need to be applied to enable stable spinning of micro-robots at fixed positions. The resulting flow field induced by rotation of micro-robots is highly correlated with the shape of robot. Since analytical solutions are unavailable for the flows induced by spinning objects with any shapes close to a bottom surface, numerical simulation is necessary to study the correlation between the shape of micro-robot and the induced rotational flows. To simplify the problem, the simulations were all carried out under the assumption of Stokes flow condition, where inertia is fully negligible. This is a good approximation to low Re condition, where most of the targeted application of this study would occur. In addition, only steady-state flows were investigated.

A customized numerical solver was used for the simulations (details in Append. B.3). Three different robot shapes besides sphere are studied, including disk, five-pointed star and cylinder. In all the simulations, three parameters were kept constant: rotation speed, largest radial length from robot center to its edge, and the thickness of the robot. The first two parameters determines the maximum linear

velocity on the surface of the rotating robot, while the third has a significant impact on the flow velocity profile along $z-$axis, especially in the vicinity of the robot.

The streamlines of flows induced by the robots with different shapes are shown in Fig. 2.6. It is firstly noticed that there exist no pure out-of-plane or pure radial components in the flow fields induced by rotating robots under Stokes flow condition. This means that for any given fluid particle inside the flows, it will always return to its initial position after orbiting around the robot for one complete revolution. This is different from the case of finite Re discussed in Sec. 2.4.2. For rotationally-symmetric shapes such as sphere and disk, the flows induced are purely circumferential and hence are time-invariant. For shapes like cylinder and five-pointed star that are not rotationally symmetric, the induced flow fields conform to the robot shape in the vicinity of the robot. As the robot with such shapes rotates in steady-state, the flow field induced would look exactly the same as the ones shown in Fig. 2.6 at each instant. However, the flow velocity at each point inside the fields could vary significantly with time. For the purpose of manipulation, a timely invariant flow field would result in a manipulation force more consistent over time experienced by the target objects. Therefore, rotationally symmetric shapes, such as sphere and disk, would be more suitable for micro-manipulation application.

The tangential velocity profile along radial distance at the height of the robot center is investigated for each shape of robot, and the results are given in Fig. 2.7 (a). The tangential velocities for non-rotationally-symmetric shapes are velocities azimuthally averaged over one rotation cycle. The results show that the flow velocity decay rapidly with increasing radial distance for all shapes, but the decay is slowest

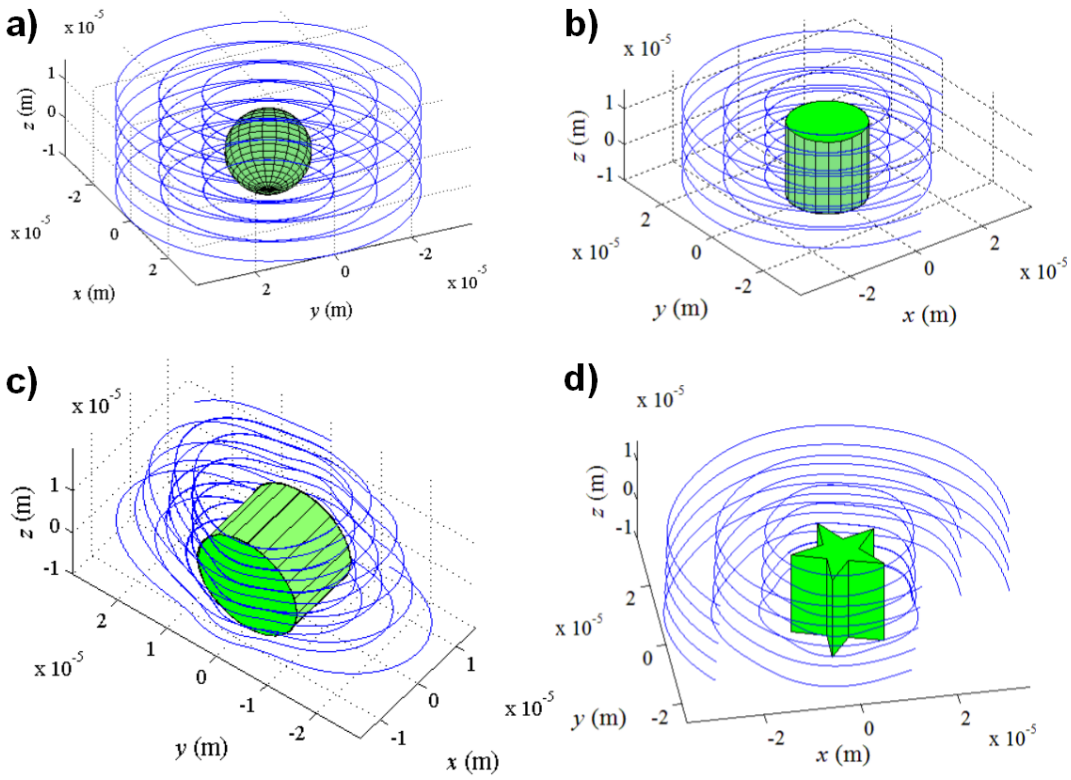

Figure 2.6: Streamlines of rotational flows induced by rotating micro-robots with different shapes near a surface. Rotation axis was perpendicular to the ground for each robot. All the robots had a thickness of 20 μm and a maximum radial distance from robot center to edge of 20 μm. Shapes include: a) Sphere; b) Disk; c) Horizontally-laid cylinder; d) Five-pointed star.

for the disk. This means a larger boundary layer possible for micro-manipulation at larger distances. Therefore, micro-robots with disk shape would be the most ideal from the perspective of generating rotational flows for micro-manipulation purposes.

Although rotationally symmetric robot shapes are ideal for micro-manipulation purposes, they might not be suitable for other applications. For example, for micro-mixing application, significant folding and twisting of flow streamlines could possibly result in more efficient mixing of different liquids. To generate such flows, non-symmetric shapes are desired. Therefore, it is possible to find optimal robot shapes for specific application purposes. This is a possible future extension of the current work.

2.4.4 Forces on a Micro-object

The behavior of non-neutrally buoyant micro-objects in the locally-induced rotational flow field is the result of contributions from viscous drag, buoyant weight, shear-induced forces (radial and vertical), wall-induced lift force, added mass force, and interaction between surfaces such as adhesion and surface friction [69]. The strong dependence of the hydrodynamic forces on the flow velocity distribution as well as the complex coupling between these forces in a non-uniform three-dimensional flow field makes it difficult to analytically model the precise behavior of micro-objects in the induced rotational flow field. For non-contact manipulation purposes, however, one significant motion bifurcation can be qualitatively analyzed: when an object circles in a stable manner within the neighborhood of the rotating robot rather than being ejected away. This bifurcation is important because the pro-

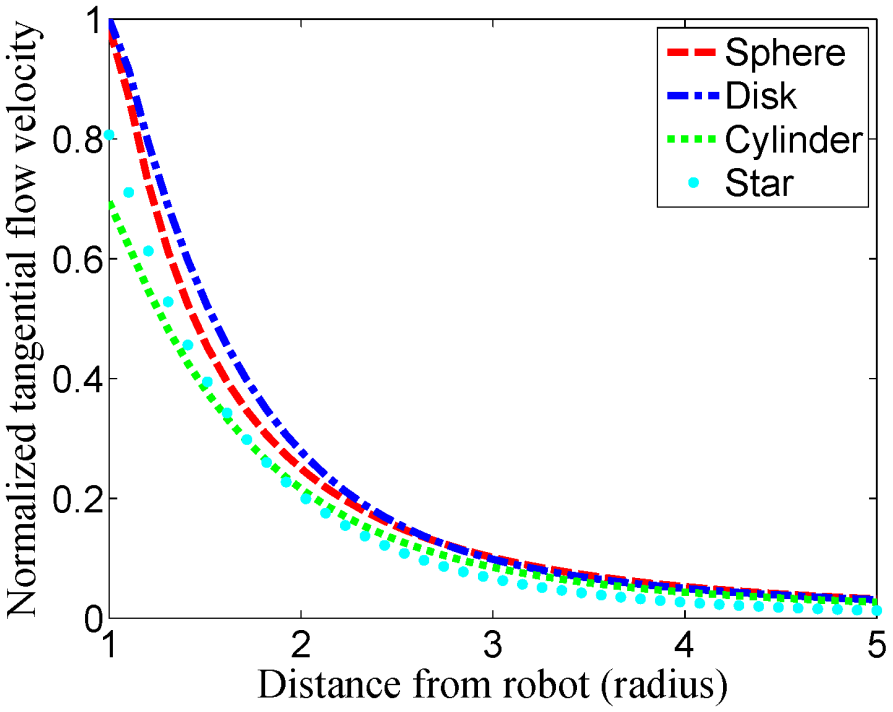

Figure 2.7: Profile of tangential flow velocity along radial distance at the height of robot center for different robot shapes. The tangential velocities for non-rotationally-symmetric shapes were averaged over one full rotation cycle. All velocities were normalized by the maximum linear velocity on the surface of the rotating micro-robots.

posed mechanism requires the objects being manipulated to be held in close vicinity of the robot. Based on a preliminary force balance analysis, we conclude that two criteria need to be met to enable stable orbiting behavior of the object in the rotational flows:

• $Motion\ criterion$: For an object resting on a substrate, mechanical contact with the underlying surface would occur when the surrounding liquid is at rest. When a rotational flow field is induced by a nearby rotating magnetic robot, a lifting effect is exerted onto the object due to a non-uniform distribution of flow velocity in the z-direction (see Fig. 2.4 (b)) [70]. If the rotational flow field is strong enough, such a lifting effect could overcome the buoyant weight of the object and the adhesion between the object and the substrate, and thus lift the object from contact with the substrate [71]. If such lift-off occurs, then the object would tend to move with the surrounding flow without surface contact; if lift-off does not occur, then to initiate micro-object movement, the propelling viscous drag force experienced by the object must overcome the surface friction.

• $Orbiting\ criterion$: To hold the object in a circular orbit rather than being ejected radially from the micro-robot, the required centripetal force must be satisfied by the total contribution from radial hydrodynamic forces and surface friction if the object is in contact with the substrate. Since the radial flow is negligible at low Re, drag force cannot be the main force to provide centripetal force. Therefore, some other types of force applied from the surrounding liquid must provide the centripetal force. A more detailed analysis is given in the following section.

It should be noticed that the $motion\ criterion$ is a necessary but not sufficient

prerequisite to the *orbiting criterion*.

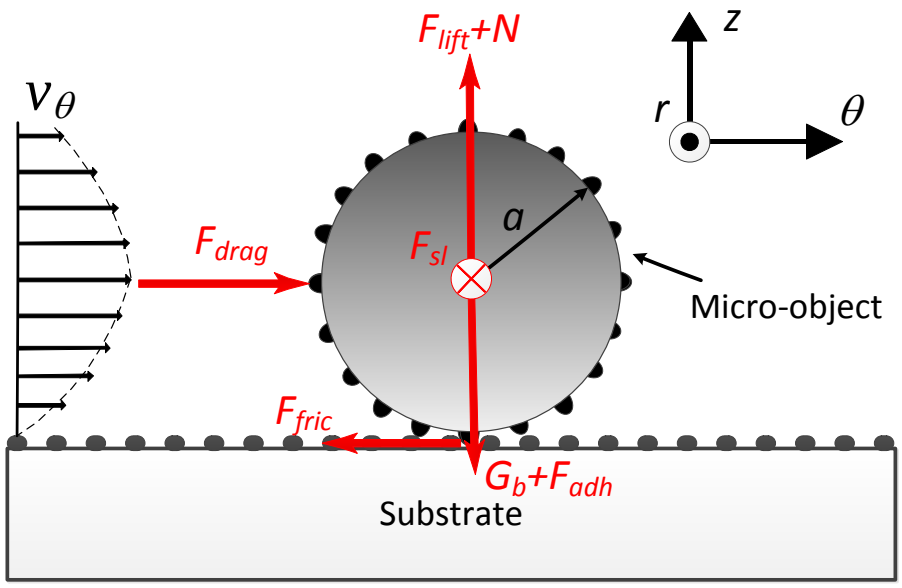

Figure 2.8: Free body diagram of a spherical micro-object in contact with the substrate in the induced rotational flows when viewed along the radial axis, ignoring radial and vertical fluidic drag forces. The microscopic roughness on the object and the substrate is enlarged.

The major forces acting on a micro-object in the induced rotational flow field are shown in the free body diagram of Fig. 2.8. While both the robot and object shapes studied in this section are spherical, the results are expected to apply roughly to other shapes through similar analysis. The following terms are pre-defined: ρ_{obj} and ρ_{fl} are the density of the object and the surrounding liquid, respectively. a is the radius of the micro-object a, R is the radius of the micro-robot, and r is the radial

distance between object and robot. ν is the kinematic viscosity of the fluid, u_c is the undisturbed flow velocity at the position of object's center, v_{obj} is the velocity of the object, γ_r is the shear rate along the radial direction of the flow field, and γ_z the shear rate along the vertical direction.

Propelling drag force

Finite-element simulations were performed to study the drag force applied by the induced rotational flows on micro-objects that propels them to follow the local streamlines (details in Append. B.4). The robot was modeled as a 30 μm-diameter sphere while the object was modeled as a second sphere fixed at certain distance from the robot. Both spheres were placed on a planar surface. Three parameters were investigated: rotation speed of the robot (f), radial distance between the robot and object (r), and the size ratio between the object and robot (a/R). The results from simulations were given in Fig. 2.9. It is observed that the drag force increases linearly with rotation speed, which is a direct result of the linear relationships between drag force, flow intensity and the rotation speed. For a given object, the drag force it experienced inside the rotational flows decreases rapidly with distance from the robot, making local manipulation possible. Figure 2.9 (c) reveals how the drag force changes with object size. For an object that is significantly smaller than the microrobot, the drag force increases slowly with the object size. For an object that has a radius $a = 0.3R$–$1R$, this force increases almost linearly with object size. Further increasing the object size results in a drag force that tends to saturate. Therefore, manipulating objects with size $a = 0.3R$–$1R$ using the proposed method would be

most efficient considering an object's weight is proportional to a^3. However, this does not limit the maximum size of objects that can be manipulated. One important note about the propelling drag force is that for an object traveling in steady-state with the local flow, such propelling drag force would be zero. This is a simple conclusion from the force-free requirement for an object to perform steady-state motion.

Radial forces for trapping of objects

For any massless micro-objects present inside the rotational flows, they would simply follow the local streamlines. But, any real object, even if it is small, would have a non-zero, finite mass. Therefore, to maintain a stable orbit of a real object inside the rotational flows, a non-zero centripetal force needs to be provided from the surrounding flows. An estimation of the centripetal force with added mass effect required to hold a spherical object in a circular orbit is given as [72]:

$$F_{cp} = \frac{m v_{obj}^2}{r} = \frac{\left(\rho_{obj}\frac{4\pi}{3} + \rho_{fl}\frac{2\pi}{3}\right) a^3 v_{obj}^2}{r}. \tag{2.10}$$

Order of magnitude analysis with S.I. units gives $F_{cp} \sim 10^{-10}$ N for $r = 3R$ and $F_{cf} \sim 10^{-14}$ N for $r = 8R$.

Such a centripetal force needs to be provided from hydrodynamic forces in radial direction. Ignoring the radial drag force due to radial flow, there could be two possible sources for fluidic force in radial direction. The first is due to the curvature of the local streamlines. As discussed in Sec. 2.4.3, the streamlines of the rotational flow induced by a spherical micro-robot are basically concentric circles. The curvature of streamlines would force any object present in the flow to constantly change direction to follow the local streamlines. This effect is not associated with inertia, and would

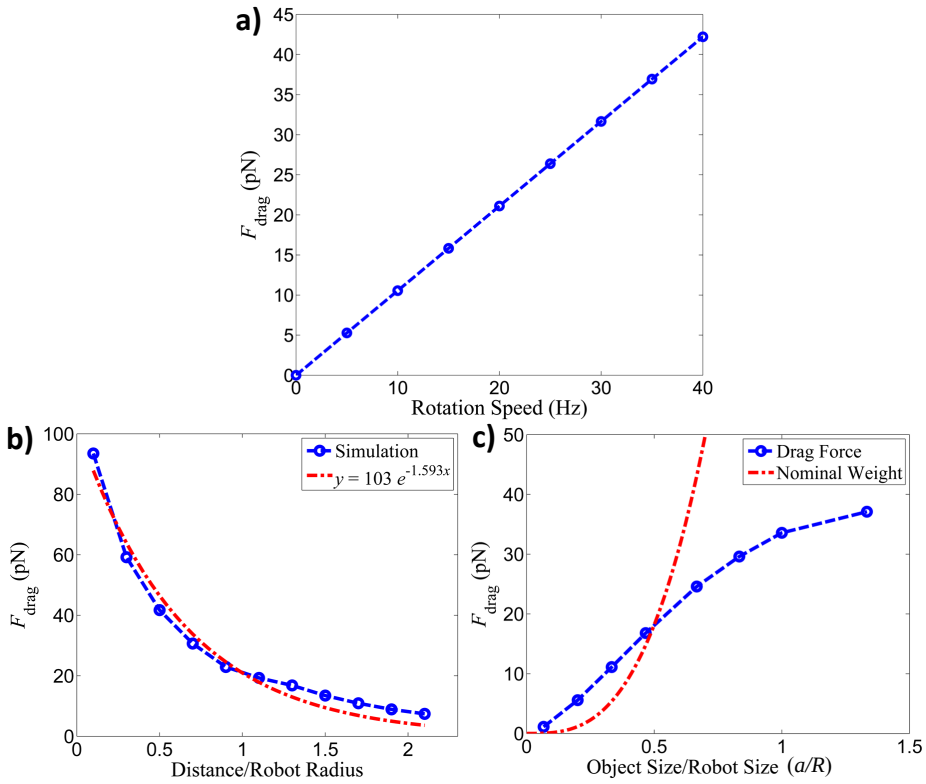

Figure 2.9: Drag force experienced by a spherical object in the presence of the rotational flow induced by a nearby spherical micro-robot. The micro-robot was modeled as a 30 µm sphere rotating on a flat surface with rotational axis perpendicular to the surface. a) The influence of rotation speed on the drag force. The object was modeled as a 20 µm sphere located 15 µm away from the robot (edge-to-edge) in this simulation. b) The influence of distance between robot and object on the drag force. The object was modeled as a 20 µm sphere, and the rotation speed was 20 Hz. c) The influence of ratio of object size over robot size on the drag force. The object was modeled to be 15 µm away from the robot which spun at a speed of 20 Hz. The nominal weight of object was calculated by $G_{nominal} = (4\pi/3)\rho_{obj} g a^3$ with $\rho_{obj} = 1.05\,\text{g/cm}^3$ and $g = 9.8\,\text{m/s}^2$.

exist even in Stokes flow regime where inertia vanishes. The second effect arises due to the convective acceleration of the flows. As shown in Fig. 2.4 (a), flow velocity drops drastically with increasing r, forming a varying shear gradient of flow velocity along r. Any object that is traveling with the local flow at a different velocity would experience a force perpendicular to direction of the flow in the presence of a shear gradient of flow velocity at non-zero Re [73]. This effect is due to inertia of the liquid, and would vanish in Stokes flow regime. To understand how these two effects contribute to the radial force on an object inside the induced rotational flow, finite-element simulations were performed with a model very similar to that introduced in Sec. 2.4.4. However, a surface velocity field perpendicular to radial distance r was specified on the object so that the net propelling drag force applied on it would be close enough to zero. For each set of given parameters, two simulation runs were carried out: one using the complete Navier-Stokes equations that include inertial effects, the other using Stokes equations that exclude inertial effects. The radial force applied on the object from these two cases was then compared to examine the contributions from inertial and non-inertial effects. Results from simulations were plotted as Fig. 2.10. An increase in viscosity decreases the overall Re and reduces inertia effects comparing to viscous effects. The results confirm that both effects contribute positively to the radial force to trap objects inside the induced rotational flow. It is also show that the radial force increases along with viscosity in both cases. The linear relationship in the Stokes flow case is a direct result of the linearity of the system. However, inertia could play an important, or even dominant role, in contributing to the radial force, especially at higher Re.

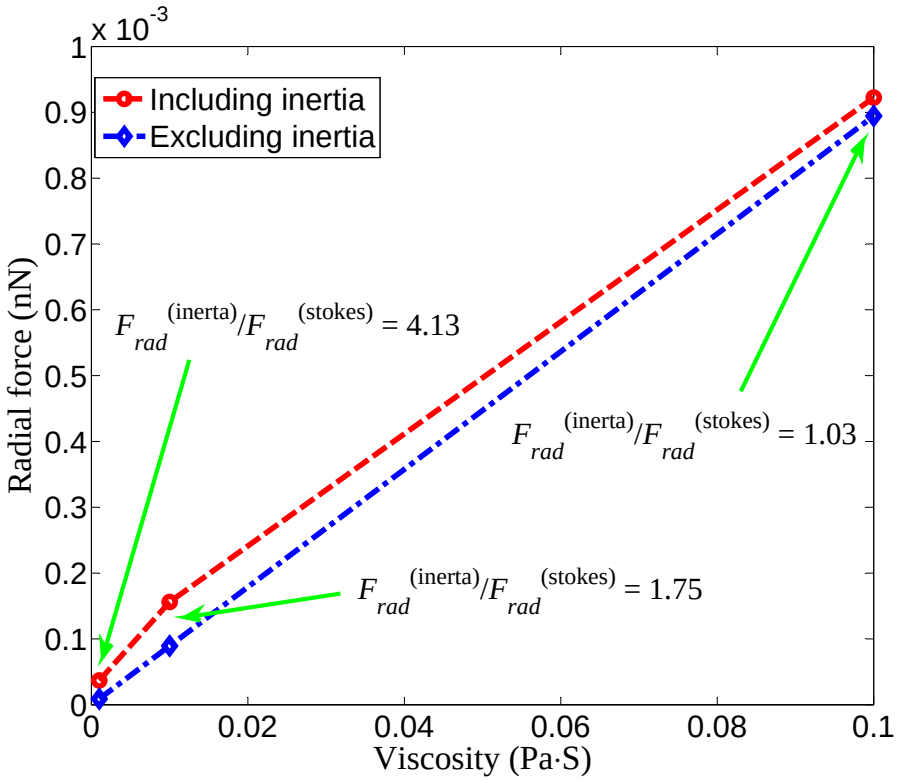

Figure 2.10: Comparison of influence of inertial and non-inertial effects on the radial force (centric) applied on a spherical object by induced rotational flow. The robot was modeled as a 30 μm-diameter sphere spinning a 20 Hz, while the object was modeled as a 20 μm-diameter sphere located 40 μm from the robot. A tangential velocity of 177 μm/s was found to give a drag force that was close enough to zero, and hence was specified on the surface of the object.

Precise modeling of the inertia-induced radial force is difficult when the object is in contact with the surface as the flows are highly non-linear functions of both r and z (see Fig. 2.4). For a qualitative analysis, the velocity gradient in the z-direction is neglected, while eqn. (2.9) is used for the radial gradient, as the derivative with respect to r gives the shear rate γ_r. The induced rotational flow then degenerates from a full 3D shear flow to a 2D shear flow. Because the flow velocity at the equator height gives the maximum shear force in the region, this result is interpreted as an upper bound. In a linear shear flow, the Saffman force that is perpendicular to shear gradient can be roughly approximated by [73]:

$$F_{sl} = 6.46\rho_{fl}\nu^{\frac{1}{2}}a^2\left(u_c - v_{obj}\right)\left|\gamma_r\right|^{\frac{1}{2}}, \tag{2.11}$$

which gives $F_{sl} \sim 10^{-8.5}$ N for $r = 3R$ and $F_{sl} \sim 10^{-11}$ N for $r = 8R$. Therefore, at any distance r within the discussed range ($3R$–$8R$), the upper limit of F_{sl} is shown to be several orders of magnitude larger than F_{cp}, suggesting that F_{sl} could possibly compensate for F_{cp}. It should be noticed that F_{sl} is a much simplified approximation of the actual inertia-induced radial force in the induced rotational flow. A more accurate formulation of such radial force is a highly complex fluid mechanics problem, and would be a future work. In addition, the actual radial force should equal F_{cp} to hold an object in a stable orbit in practice. At a given distance from the robot r, the required centripetal force F_{cp} is proportional to a^3 and v_{obj}^2, while the Saffman force $F_{sl} \propto a^2$. Because a smaller object has both smaller a and v_{obj} than a larger one, it is expected that smaller objects would more easily satisfy the $orbiting\ criterion$.

Vertical forces

As previously stated, lift-off plays an important role in the satisfaction of the $motion\ criterion$. Therefore, let us first consider a typical case of vertical forces experienced by a spherical object resting on the substrate. These forces include the object's buoyant weight, adhesion between surfaces and the hydrodynamic lifting effect. The buoyant weight is simply given by

$$G_b = (\rho_{obj} - \rho_{fl})\, g \frac{3}{4}\pi a^3, \tag{2.12}$$

and the hydrodynamic lifting effect can be approximated by [71]:

$$F_{lift} = 9.26\gamma_z \mu a^2 \left(\frac{\gamma_z a^2}{\nu}\right). \tag{2.13}$$

This approximation is formulated based on linear shear flow, which has a shear rate smaller than that of the actual induced rotational flow in the vertical direction, and thus should give a lower bound on the actual lifting effect. For an object at a given distance r, such a lifting effect would be the largest just before the object begins to move, because any translational or rotational motion of the object in a shear flow will significantly decrease the lift force [71]. Once the object starts moving, additional terms due to translation and rotation of the object should be added to eqn. (2.13) for proper approximation [71].

Given the same weights, spherical objects resting on a flat plane would experience smaller adhesion from the plane than objects with other shapes due to the smaller contact areas. According to the Johnson-Kendall-Roberts (JKR) model of elastic contact between a smooth sphere and a smooth flat surface, the pull-off force

required to lift a sphere from a flat surface is determined as [74]:

$$P = 1.5\pi a W_{adh}, \tag{2.14}$$

where W_{adh} is the work of adhesion between the object and the substrate immersed in the given liquid. Lift-off occurs only if

$$F_{lift} - G_b > P. \tag{2.15}$$

Due to typical micron scale roughness of the surfaces, the actual pull-off force required could be more than one order of magnitude smaller than P [75].

Once lift-off occurs and surface friction vanishes, an object will be driven at a non-zero translational speed by the rotational flow, determined by hydrodynamic effects. The flow field is highly non-uniform (see Fig. 2.4), which results in complex hydrodynamic interactions. However, Taylor's expansion technique can be used to approximate any general flow field with the presence of a wall by second-order polynomial flow fields, in which case the viscous drag forces and torques on a sphere near a wall have already been examined [76, 77].

In cases where lift-off does not occur, mechanical contact between the object and the substrate causes surface friction, which would be a constant resistive force F_f. Such force is directly related to the actual contact area A_c as $F_f = \tau A_c$, where τ is the effective shear modulus between the object and the substrate. The inclusion of this force would tend to prevent objects from moving, and hence result in a larger difference between the object speed and the effective speed of the surrounding flow. If the total effect of the hydrodynamic forces fails to overcome F_f, the motion criterion is not met and the object will remain stationary.

2.5 Experimental Results and Discussion

Experiments were performed using the containers and the actuating systems introduced in Sec. 2.3.1. Rotation rate was measured as frequency $f = \omega/2\pi$, in the unit of Hz, in all experiments. In all experiments, at least five trials were performed to determine repeatability and error, and the error bars in the plots indicate standard deviation over five trials. In every experiment, all measurements reported were taken in a single day. In the object speed characterization and parallel micro-manipulation experiments, micro-robots were operated on the specially prepared substrate with magnetic micro-docks embedded.

To track the micro-robot position and obtain its translational speed: A particle filter algorithm based on the gradient of the image was used to automatically track the positions of the micro-robots in real-time. The position differentiated over time is used to calculate the average velocity of a micro-robot over the entire experiment durations.

2.5.1 Sub-Millimeter Micro-Robots

Experiments were first carried out on micro-robots that were a few hundred microns in size to verify the validity of the proposed mechanism and characterize the system. Given the size of the sub-millimeter-scale system, a silicone oil of 50 cSt viscosity was used as the medium to achieve low enough Re. Therefore, the results from this larger scale experiments should still be useful for predicting the performance of the proposed micro-manipulation mechanism at smaller scales.

Motion Characterization of Spherical Micro-Robot

The high rotation rate of the magnetic micro-robot, which is a crucial parameter to characterize the robot's motion, can not be observed directly by our current experimental setup. However, according to eqn. (2.5), the robot rotates synchronously with the applied magnetic field $\boldsymbol{B}$ when $|\boldsymbol{B}| > B_{\text{step-out}}$. In such synchronization, the micro-robot rotation frequency f_{robot} equals the applied field rotation frequency f, which was precisely controllable in experiments.

Experiments were performed to examine the relationship between the micro-robot translational speed u_{trans} and $|\boldsymbol{B}|$ to determine the range of $|\boldsymbol{B}|$ for which the micro-robot rotates synchronously with the applied field for all the rotation frequencies f used in this paper. The results, shown in Fig. 2.11 for the pure rolling case ($\phi = 0°$), indicate that, as expected from eqn. (2.5), higher $|\boldsymbol{B}|$ values are required to saturate u^* for higher values of f. It is noted that $|\boldsymbol{B}| > 3.5\,\text{mT}$ results in u^* saturation for all frequencies up to 120 Hz, indicating that the rotation of the robot was synchronized with the applied field. Therefore, $|\boldsymbol{B}|$ values between 3.5 mT and 5.0 mT were used for all the rest experiments at sub-millimeter scale. A final note from Fig. 2.11 is that u^* is much less than unity for all experimental parameters, indicating that the micro-robot experiences significant slipping on the substrate during rolling.

The relationship between u_{trans} and f, shown in Fig. 2.12 for the pure rolling case ($\phi = 0°$) suggests that the response can be grouped into two linear regimes, separated at around f=5 Hz. The bifurcation possibly indicates a change in rolling conditions at this frequency from rolling with slipping at low frequency to a case of

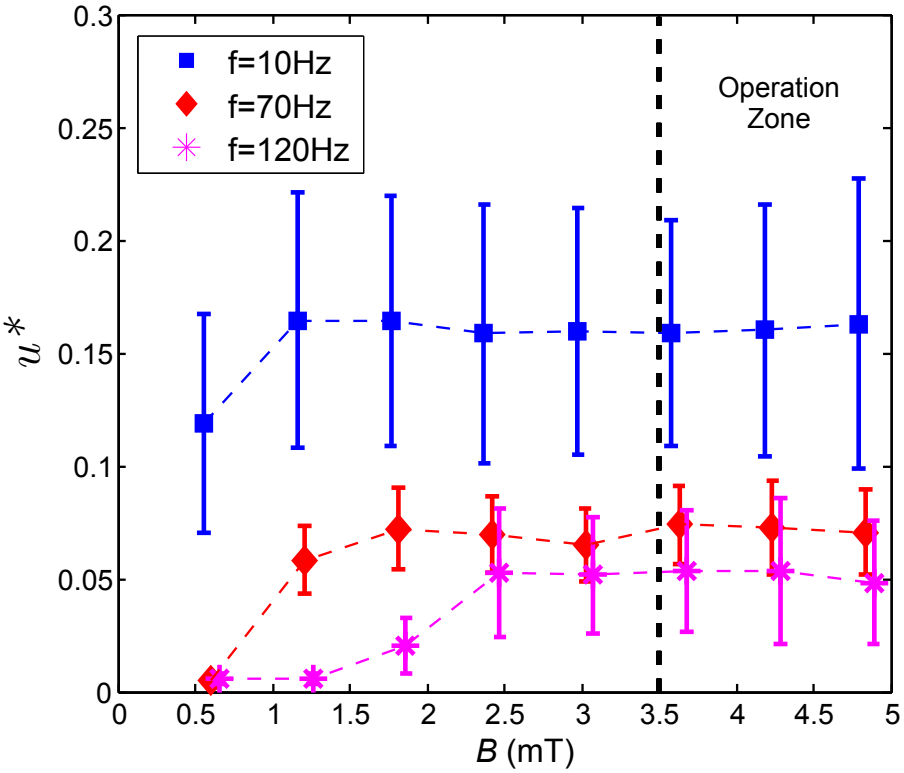

Figure 2.11: Measured dimensionless translational speed u^* versus magnetic flux density at f =10 Hz, 70 Hz and 120 Hz in pure rolling ($\phi = 0°$). The response at each rotation frequency displayed a saturation behavior with field strength, indicating that the micro-robot was rotating synchronously with the field once saturation was reached. All further experiments were conducted with flux density in the saturated operation zone, $|\boldsymbol{B}|$ >3.5 mT, indicated on the figure, to ensure synchronous micro-robot rotation.

no surface contact at higher frequencies.

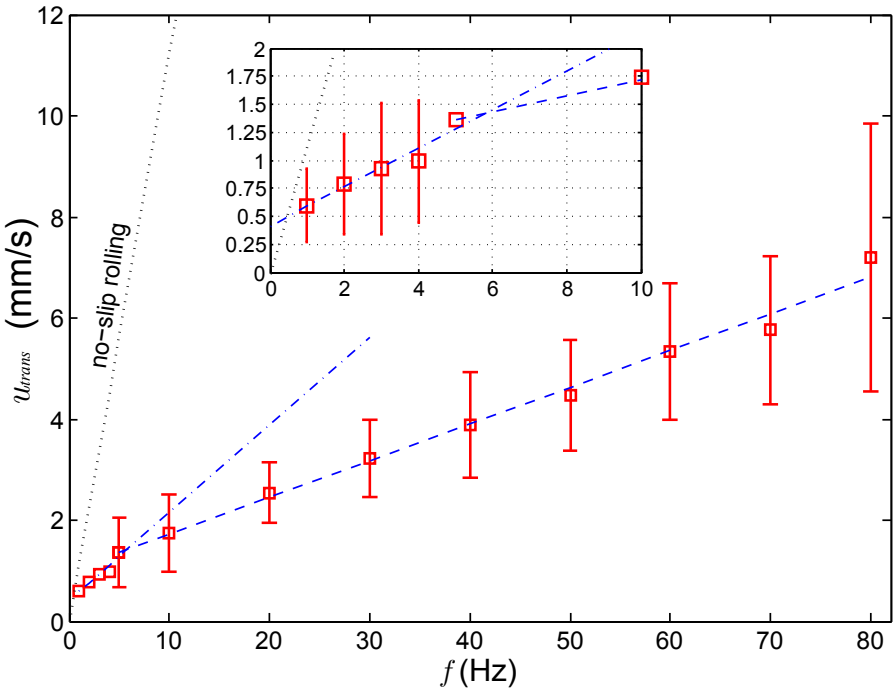

Figure 2.12: Measured micro-robot translational speeds u_{trans} as a function of the rotation frequency f with applied field magnitude $|\boldsymbol{B}| = 3.63\,\text{mT}$ in the pure rolling case ($\phi = 0°$). The dotted line shows the no-slip velocity from eqn. (2.6), and the dashed lines are linear fits to the two regimes of experimental data. The subplot expands the low frequency data, in which a bifurcation in the slope of the fitted results occurs at around $f = 5\,\text{Hz}$, indicating a change in rolling conditions at this frequency.

The dimensionless micro-robot translational speed u^* is plotted in Fig. 2.13 for values of tilt angle ϕ from 0° (pure rolling) to 90° (pure spinning) at several rotation frequencies. In comparison with eqn. (2.6) which gives the no-slip velocity of the micro-robot, the data presented showed a much lower velocity due to slip-

ping, especially at high frequencies. It is interesting to note that the reduction in u^* with frequency shows a saturation behavior as f approaches 120 Hz. An anomaly is observed at small ϕ for $f = 120$ Hz where u^* increased with ϕ up to 25°. This inconsistency may be attributed to complex fluid flow effects at higher Reynolds numbers near a planar surface[65], which is out of the scope of this thesis work.

The u^* values at all frequencies were supposed to be zero at $\phi = 90°$ (pure spinning) for micro-spheres spinning on a smooth flat surface in liquids. The observed non-zero values also suggest the imperfection of the robot's geometry or non-flat topography/roughness of the substrate surface.

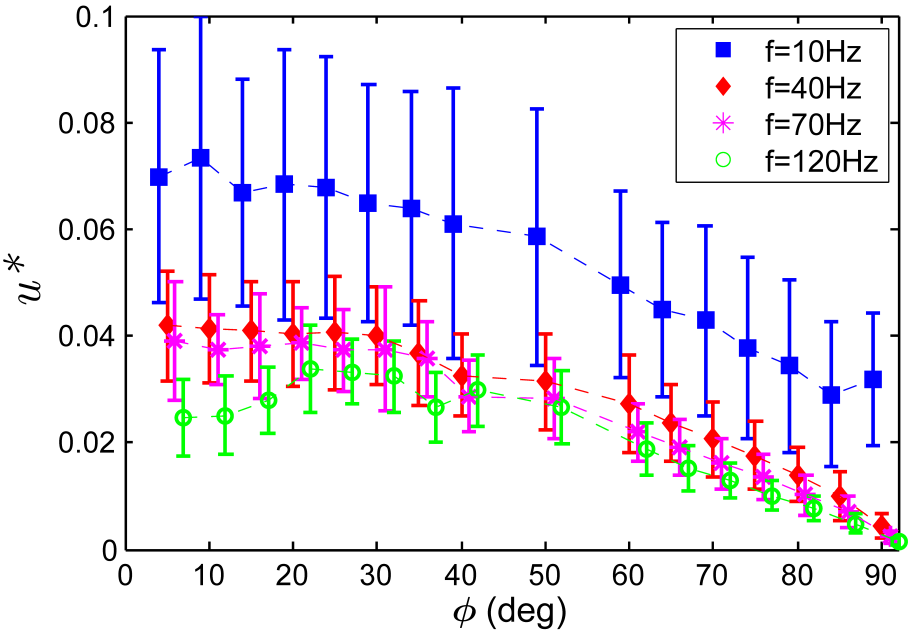

Figure 2.13: Measured dimensionless micro-robot translational speed u^* as a function of tilt angle ϕ with applied field magnitude $|\boldsymbol{B}|$ =4.40 mT.

Characterization of Micro-Object Speed

By spinning a micro-robot in place, many particles can be manipulated simultaneously. To characterize the pushing velocity of the micro-objects as a function of distance from the micro-robot, an experiment was performed with seven 200 μm-diameter polystyrene beads which were manipulated by a 360 μm-diameter micro-robot on a micro-dock substrate, as seen in Fig. 2.14. The micro-object velocity is also plotted as a function of radial distance from the micro-robot for all seven micro-spheres, with an exponential fit superimposed. While eqn. (2.9) predicts an $r^{-2.43}$ falloff in flow velocity, the fit shows a $r^{-3.12}$ falloff. This discrepancy is mainly due to finite size of the micro-object, which made the object experience a non-uniform distribution of flow velocity over its surface. The presence of the underlying substrate also contributed to such discrepancy, as it retarded the object from moving along with the flows. The micro-sphere velocity fit can be used to accomplish accurate and complex manipulations of many objects by controlling the positions of magnetic micro-robots.

More experiments were performed to examine the influence of object size and shape on object speed inside the rotational flows. Besides the polystyrene beads of 200 μm used in previous experiment, another set of polystyrene beads of 116 μm diameter, 400 μm polyurethane arrows and 600 μm polyurethane blocks were tested. The largest distance r that gives a non-zero v_{obj} for a certain object, designated as r_m, defines the range within which the $motion\ criterion$ is satisfied for the corresponding object, whereas satisfaction of the $orbiting\ criterion$ can not directly be determined from the figure.

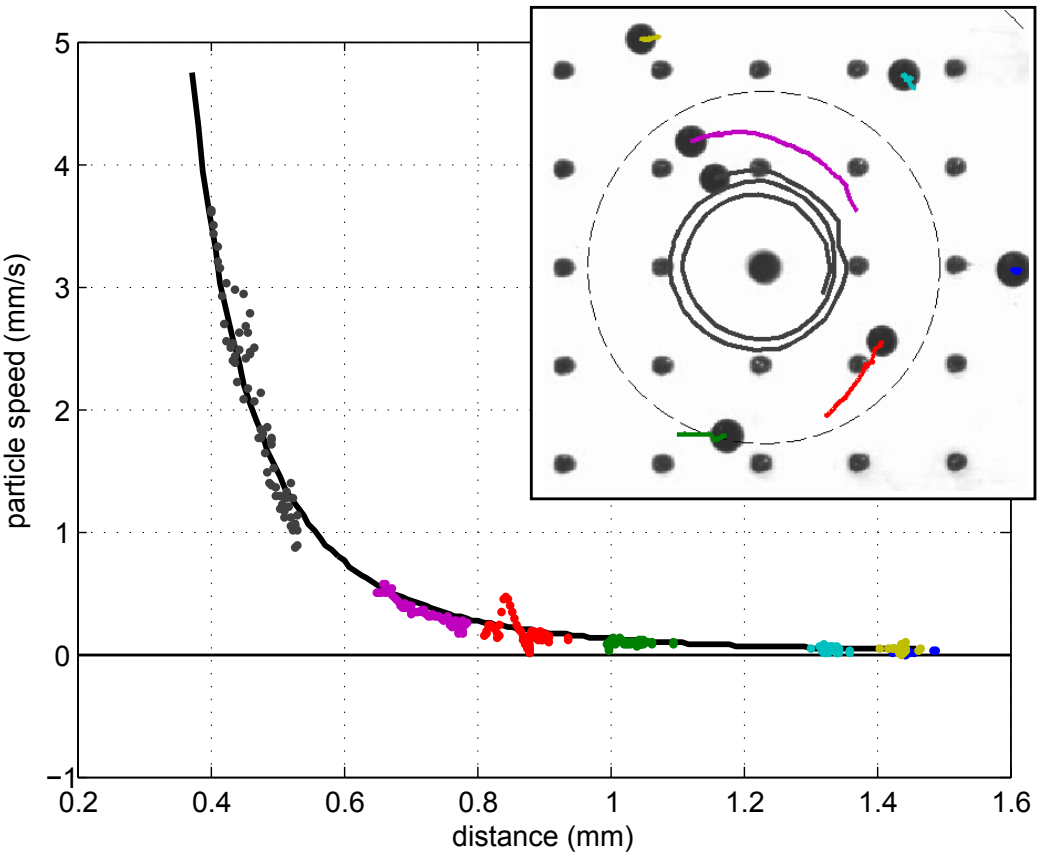

Figure 2.14: Measured microsphere speeds as a function of radial distance from a single 360 µm diameter micro-robot spinning at 50 Hz. The black line is an exponential fit of the form $Cr^{-3.12}$. Datapoints from seven particles are extracted at 10 Hz from 30 s of video. The inset is an image with individual particle paths overlayed as they circle the spinning micro-robot in the center of the image. The dotted circle is 2 mm in diameter and the particles are 200 µm in diameter. Rotation direction is counterclockwise.

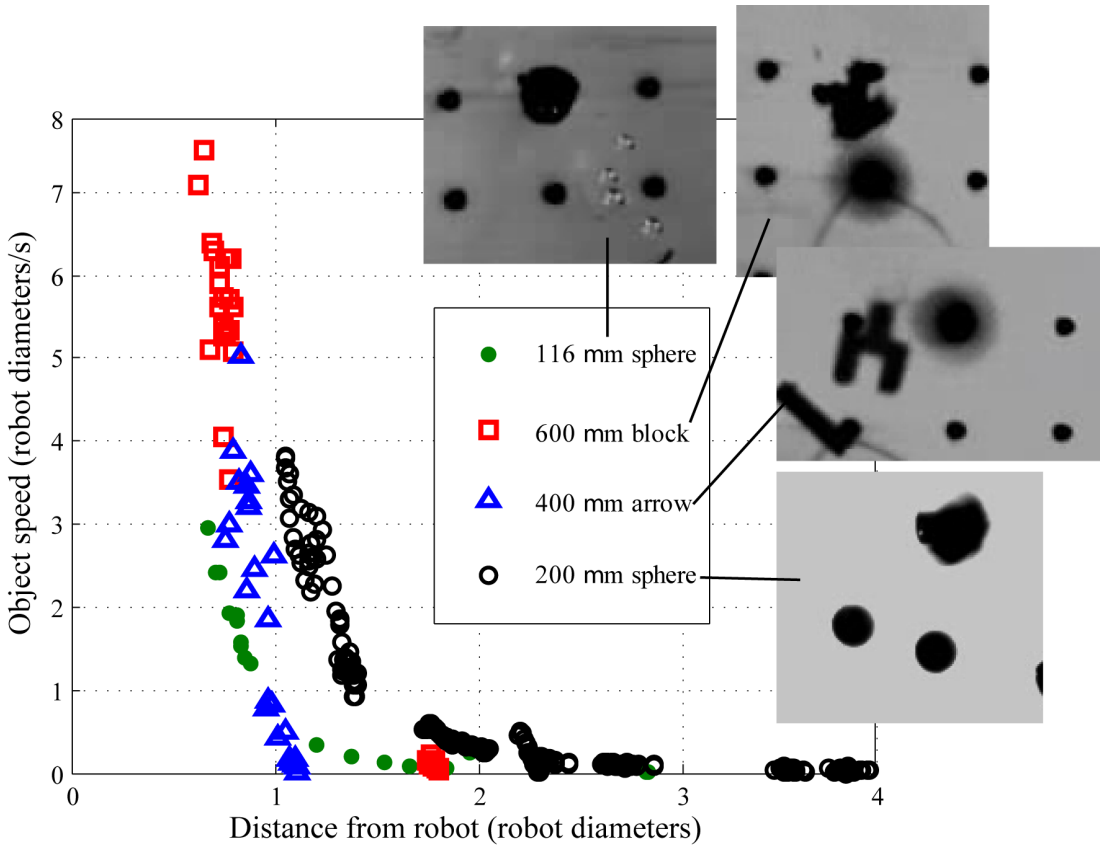

Figure 2.15: Measured micro-object speeds as a function of distance from a single 360 µm-diameter micro-robot spinning at 50 Hz. Data points were extracted at 10 Hz from 30 s of video for each object, and distance is normalized by the robot diameter. Data points stop at the distance when the object speed reaches zero. The insets are an image of each object type being manipulated, taken by optical microscope.

Experimental results suggest a strong influence of the object size and shape on both the satisfaction of the $motion\ criterion$ and the object speed. The previous qualitative force analysis in the Sec. 2.4.4 is helpful to explain these experiment results. First, it is observed that shapes closer to spheres give a larger r_m. This may directly result from the fact that the other shapes tend to lie flat on the substrate, increasing contact area and thus adhesion, leading to the failure for occurrence of lift-off and significant surface friction. Next, at a giving distance r, the larger spherical objects orbit with higher speeds than non-spherical objects for small values of r. This is because, for spherical objects experiencing much less adhesion than the arrows and the blocks, it is possible for them to be lifted off from the substrate when they are placed close to the rotating robot, which is also the center of the rotational flow field. According to the previous analysis, after lift-off occurs, surface friction is no longer present, resulting in higher steady object speeds than that with the presence of surface friction. Thirdly, the smaller sphere moves significantly slower than the larger ones at any given r within the range of experiments. Noticing that F_{lift} is explicitly proportional to a^4, while $P \propto a$ and $G_b \propto a^3$, the lifting effect varies most significantly with object size, which means that a sphere with a larger size is easier to lift off from the surface. Once lift-off occurs, a larger F_{lift} will lead to a wider separation between the object and the substrate; as the separation increases, the influence of the substrate on hydrodynamic effects which retards object movement decreases logarithmically for very small gaps [76, 77]. In addition, because v_θ is a function of z (see Fig. 2.4 (b)), smaller objects are subject to a smaller v_θ and thus weaker overall hydrodynamic propulsion. This may also help to explain why the

smaller spheres move with the lowest speed at very small values of r, within which distance the flow velocity varies drastically with z.

Although not directly shown in Fig. 2.15, it has been observed in the experiments that the object size plays a major role to determine the satisfaction of the $orbiting$ $criterion$. For the larger beads, ejection was observed above a critical distance, while the smaller beads always remained in orbit, an effect predicted in Sec. 2.4.4 from looking at a scaling analysis. In the extreme case where the object's size is significantly smaller than the robot's, the object tends to be drawn to the robot rather than maintaining a stable distance. In fact, in some experiments we have seen the 116 μm-diameter beads even being drawn into contact with the robot. For precise manipulation of fragile or biological micro-objects, it could be disadvantageous if the objects are drawn too close to the robot and eventually in contact.

Micro-Manipulation Demonstration

The capabilities of rotational micro-robot locomotion and non-contact micro-object manipulation are shown in Fig. 2.16 (a), where a 360 μm-diameter magnetic spherical micro-robot transports a 200 μm-diameter polystyrene bead with a density of 1.05 g/cm on a glass substrate. An external magnetic field with strength of 3.5 mT rotating at a frequency of $|\omega| = 30$ Hz was applied to induce the synchronous rotation of the magnetic robot. In this experiment, the rotation tilt angle was kept small ($< 10^{\circ}$), resulting in a translational robot speed of approximately 2.5 robot-diameters/s. During manipulation, the micro-object was trapped in orbit along with the traveling robot as it translated, resulting in a stable "carrying" behavior for long-distance

manipulation.

The concept of using multiple rotating micro-manipulators in parallel to create virtual fluidic channels for non-contact object transportation is illustrated in Fig. 2.16 (b) and (c). Due to the complex flow field generated by multiple manipulators, a critical separation between the polystyrene bead and the closest robot was observed, within which the beads were trapped in orbit around the single robot instead of being passed to the next one. The value of such a critical initial separation depends on the spacing between manipulators. In this experiment, the distance between the spinning manipulators was 1200 μm, resulting in a critical initial separation of about 600 μm. Configurations of micro-manipulators other than a straight line or "L" shape is feasible.

Autonomous Feedback-Control of Spherical Micro-Robot

The position of the spherical micro-robot can be precisely and autonomously controlled while it spins and translates on a surface based on visual feedback. Such capability was demonstrated in two experiments: fixed-point spinning and path following.

Spinning at Fixed Point

The 2D positions of a purely spinning micro-robot ($\phi = 90°$) are shown in Fig. 2.17, where it was observed that an uncontrolled micro-robot wandered quickly from the target spinning position on a non-specialized glass surface. However,

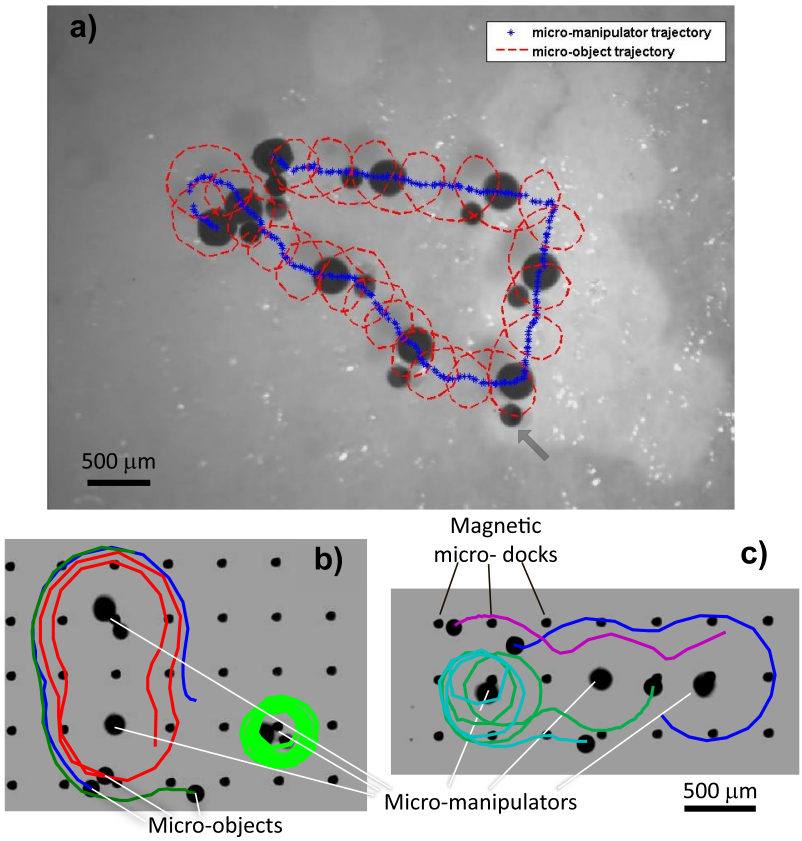

Figure 2.16: a) Top-view optical microscope images of a 360 μm-diameter spherical magnetic micro-robot carrying a 200 μm-diameter polymer bead along an arbitrary path on a glass substrate using rotational flow. Eight frames taken from video of the whole manipulation process, with an equal interval of 1.23 s, were overlaid to show the paths of the robot and bead. The entire duration was 9.87 s. The robot rotated at 30 Hz and translated at a speed of approximately 2.5 robot-diameter/s (900 μm/s). b)–c) The micro-robots were trapped at prescribed positions by magnetic micro-docks embedded in the substrate while rotating at 50 Hz in b) "L"-configuration and c) line-configuration. The images were frames taken from video of the manipulation of multiple micro-objects. The colored lines show the actual trajectories of multiple objects being simultaneously manipulated from different starting positions.

the position of the micro-robot was held close to the target using a piecewise visual-based feedback controller, resulting in an RMS position error of less than 1/10 of the robot's diameter (32.6 μm). The wandering direction was affected by the initial conditions of the impulsively started rotation of the robot [65], but uncontrollable with current experimental setup.

The feedback controller obtained the current position of the micro-robot based on visual image. When the robot was further than the tolerance distance away from the target spinning position, the controller altered the robot's tilt angle ϕ from 90° and rolls the micro-robot towards the target position. The tilt angle was kept smaller when the robot was further away from the target position, resulting in a larger translational speed. The change points of the piecewise controller for tilt angle, in terms of robot's diameter, were 1/50, 1/20 and 1/10, and the corresponding ϕ values were 90°, 84° and 80°.

Path Flowing

The spinning micro-robot also has the capability to follow a complex path using visual-based proportional-derivative (PD) feedback control on a non-specialized glass surface, as shown in Fig. 2.18. The translational speed was controlled by varying ϕ between 80° and 90° while f was kept constant at 60 Hz. By keeping ϕ near 90°, the spinning component $f_s = |\omega_\perp| / 2\pi$ varied less than 2%, which would allow for stable object manipulation during the entire motion. The proportional gain for the controller varied from 130°/mm to 1200°/mm, while the derivative gain from

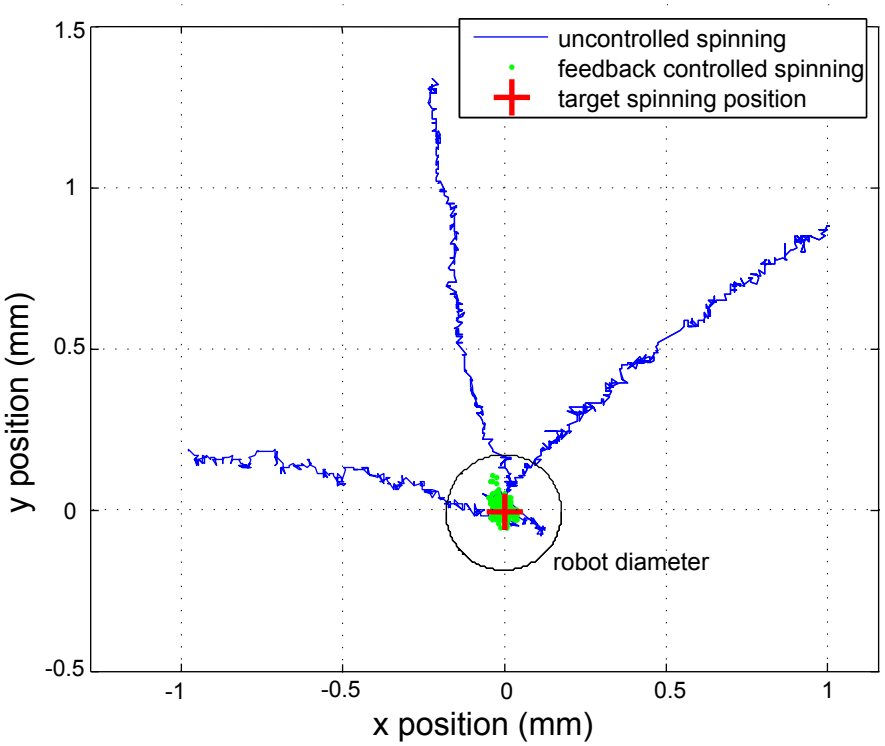

Figure 2.17: Robot trajectories for three uncontrolled spinning and one representative feedback controlled spinning case at $f = 60\,\text{Hz}$. $|\boldsymbol{B}| = 4.40\,\text{mT}$ in spinning mode ($\phi \approx 90°$). The duration of each run was 8.0 s. The black circle indicates size of the spherical micro-robot. For the feedback controlled case, a piecewise controller attempted to maintain the desired micro-robot position using the control parameter ϕ, which was adjusted between three values: 80°, 84° and 90° to control translational speed to reject disturbances. The change points for the controller, in terms of robot's diameter, were 1/50, 1/20 and 1/10. Here the position error was only 32.6 μm (RMS).

0.5°s/mm to 4.9°s/mm, between the smooth segments and sharp-turn segments on the path, and the controller output ϕ was constrained between 80° and 90°. Such results demonstrate the potential of the spinning micro-robots to act as a precision source of rotary flows for micro-object manipulation on arbitrary planar surfaces.

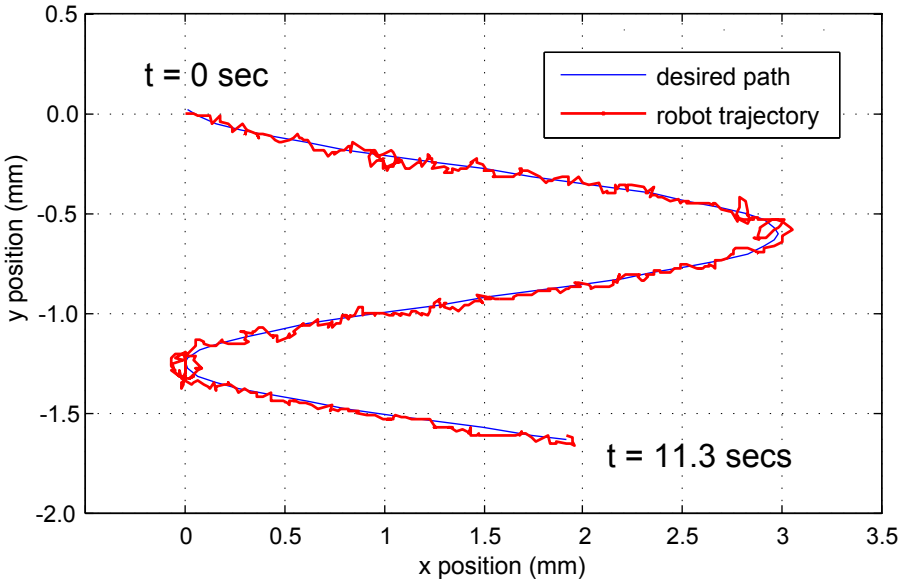

Figure 2.18: Micro-robot path following experiment using vision feedback-based PD controller along a desired path while spinning. The translational speed was controlled by varying ϕ between 80° and 90°. Total traveling time $t = 11.3$ s. The RMS path tracking error in this case for a 360 μm micro-robot was 24 μm.

Automated Micro-Manipulation Using Single Micro-Robot

Automated manipulation of a 200 μm micro-object was also implemented based on visual feedback, with results illustrated in Fig. 2.19. First, the micro-robot slowly

rolled from the initial position to the standby position close to the micro-object (Fig. 2.19 (a)–(b)). Then it started spinning at a high frequency ($f = 30$ Hz), picked up the micro-object (Fig. 2.19 (c)) and carried it along towards the target position in a straight path(Fig. 2.19 (d)). The micro-robot stopped rapid spinning when it approached close to the target position (Fig. 2.19 (e)). To precisely place the micro-object to the target position, the micro-robot span at a low frequency ($f = 6$ Hz) and slowly pushed the object to the target (Fig. 2.19 (f)). The final average position error was less than 20% of object size over five trials.

2.5.2 Micron-Scale Micro-Robots

Experiments with micro-robots less than 50 μm in size were performed to further demonstrate the scalability and versatility of the proposed mechanism for micro-manipulation applications. Demonstration of micro-manipulation of various micro-objects were carried out, including micron-sized PS beads, silica beads, HL60 human myeloid leukemia cells (ATCC #CCL-240, American Type Culture Collection) and multi-flagellated bacteria $Serratia\ marcescens$ (ATCC 274, American Type Culture Collection). Experiments with HL60 cells were performed in the solution of phosphate buffered saline with 1 mM $CaCl_2$ and 1 mM $MgCl_2$, while the medium for experiments with swimming bacteria was the motility medium (0.01 M KH_2PO_4, 0.067 M NaCl, 10^{-4} M EDTA, 0.01 M glucose). All the other experiments were performed in deionized water.

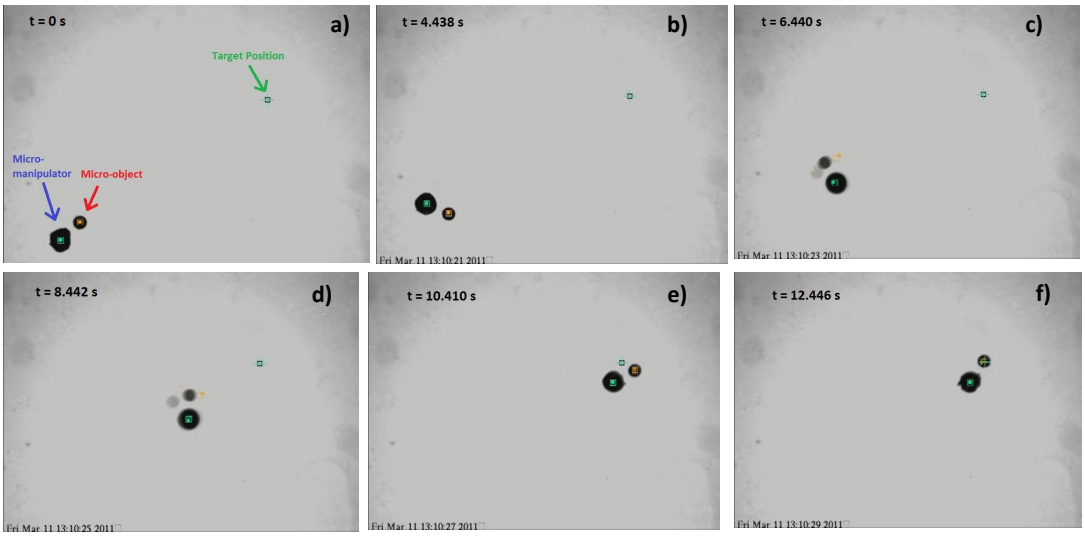

Figure 2.19: Automated manipulation of a 200 μm diameter polystyrene micro-bead using a 360 μm diameter spherical magnetic micro-robot. Five frames were taken from video of the whole manipulation process at different periods. a) Initial position. b) The micro-robot slowly rolled to the standby position which was within 1.5×(robot-radius + object-radius). c)–d) The micro-robot then fast span to pick up and carry the micro-object to the target position. e) It stopped spinning when getting close to the target position, then f) span slowly to precisely push the micro-object to the target position.

Motion Characterization of Micro-Robot

We repeated the motion characterization experiments that had been done at sub-millimeter scale for the micro-sized micro-robot. Measurements of speed of micro-robot translating on the glass substrate were done on 4 μm-diameter micro-robots, and the results are given in Fig. 2.20. Similar to results from sub-millimeter-scale experiments, it is observed that the micro-robot's translational speed increased almost linearly along with rotation speed up to around 100 Hz, but it then saturated at higher rotation speed. Such saturation may result from the increasing hydrodynamic friction and lift force. Figure 2.20 reveals that the relationship between translational speed and tilt angle ϕ previously found on larger robots was maintained at such a small scale.

Manipulation of PS Beads with Different Sizes

Because there is no grasping, clamping or any form of mechanical contact between the micro-robot and the targeted object occurring during manipulation, the only factor that could possibly limit the size of objects that a spherical micro-robot can manipulate is the drag force exerted by the induced rotational flows as discussed in Section 2.4.4. The intensity of the rotational flow field can be adjusted by controlling the rotation speed of the micro-robot, and hence it is possible to use a one-size micro-robot to handle a wide range of object sizes. Experimental demonstration was performed using a 30 μm-diameter spherical magnetic micro-robot to manipulate PS beads with three different diameters: 20 μm, 10 μm and 4.5 μm. The results are plotted in Fig. 2.21. In the experiments, the tilt angle ϕ of the micro-robot was main-

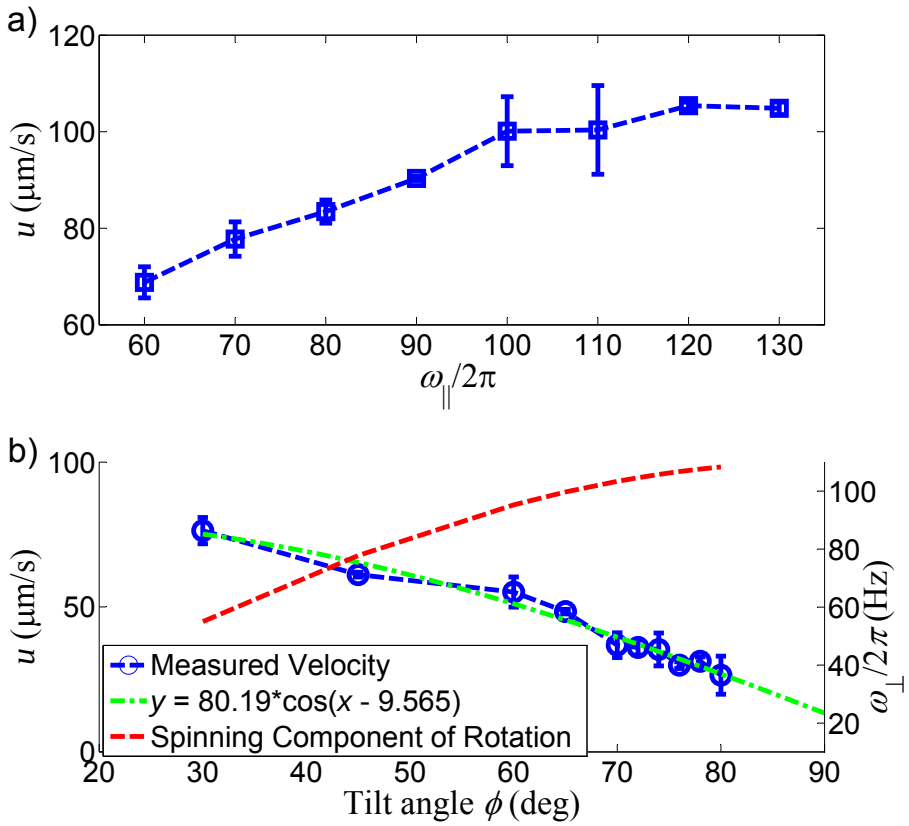

Figure 2.20: Measured translation speed of micro-robot as a function of rotation speed and tilt angle ϕ, respectively. Measurements were done on 4 µm-diameter micro-robots on a glass substrate. a) Translational speed as a function of rotation speed. A rotation with axis parallel to the substrate was applied. b) Translational speed as a function of tilt angle ϕ. A rotation speed of 110 Hz was applied.

tained at 75° or 80° with the rotation speed varying between 15 Hz and 55 Hz. As shown, the same micro-robot could be used to manipulate PS beads varying four-fold in size.

Manipulation of Micro-Objects with High Density and Large Size

Manipulating micro-objects with density close to water, such as polymer beads and biological cells, benefits from buoyancy which eliminates the influence of object weight on manipulation and facilitates manipulation. Hence, it is challenging for micro-robotic systems to perform non-contact manipulation on objects that are significantly denser than water. Such a task becomes even more difficult if the objects are larger than the micro-robots in addition to high density. The proposed micro-manipulation approach can tackle such challenge, as it is capable of manipulating objects that have a density significantly higher than water as well as a size larger than the robot's. Experiments were carried out to manipulate 5 μm-diameter silica beads using a 4 μm-diameter micro-robot in water on a surface, as shown in Fig. 2.22. The silica beads have a nominal density of 2 g/cm^3. In the experiments, a rotation speed of 25 Hz with a tilt angle of 80° was used. The micro-robot was able to stably carry a single large silica bead along different trajectories with a large curvature or sharp turns.

Manipulation of Biological Samples

Micro-manipulation techniques can find important applications in biological and biomedical research, as the ability of harmlessly manipulating micro-scale biolog-

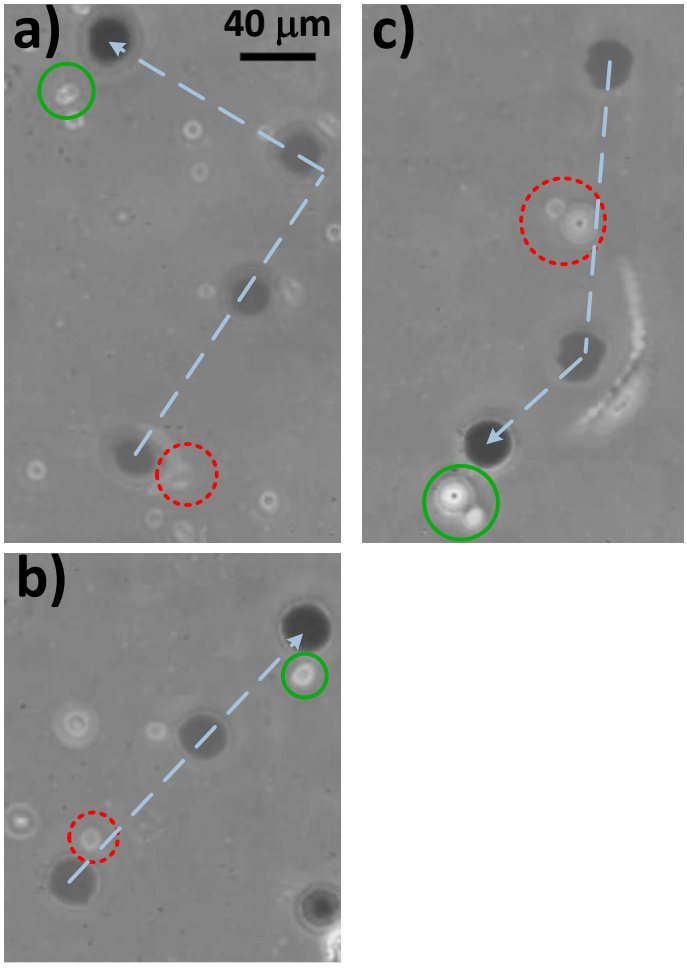

Figure 2.21: Manipulation of PS beads with different sizes using a 30 μm-diameter spherical micro-robot. The red dashed circles and the green solid circles indicate the initial and final positions of the PS beads, respectively, and the dashed lines with arrowheads show the trajectories of the micro-robot. a) Carrying 4.5 μm-in-diameter PS beads with a rotation speed of 20 Hz and a tilt angle of 75°. Duration was 5.0 s. b) Carrying a 10 μm-diameter bead with a rotation speed of 15 Hz and a tilt angle of 80°. Duration was 8.3 s. c) Carrying a 20 μm-diameter bead with a rotation speed of 55 Hz and a tilt angle of 75°. Duration was 1.3 s.

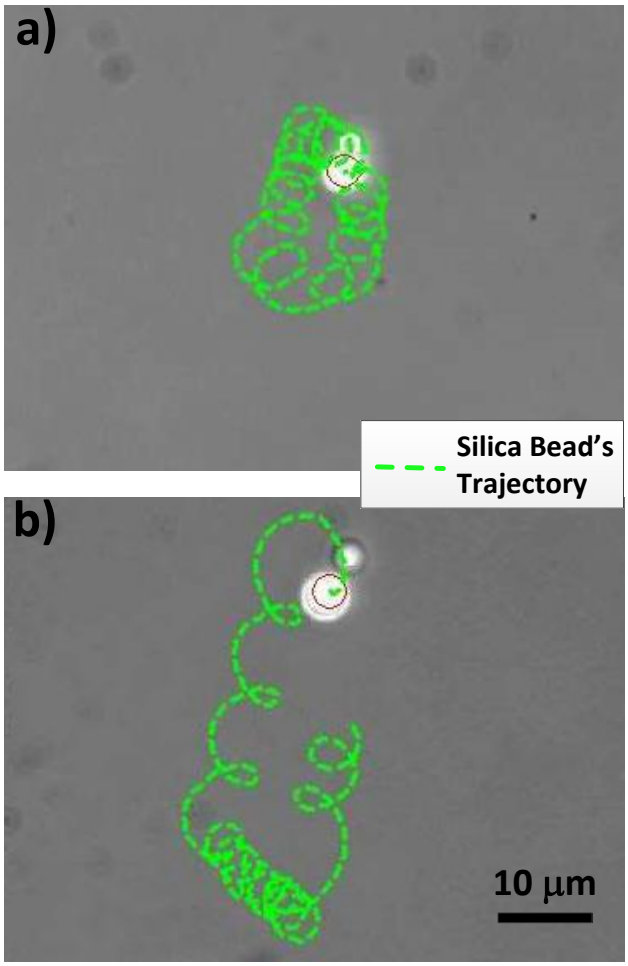

Figure 2.22: Manipulation of single 5 μm-diameter silica beads using a 4 μm-in-diameter micro-robot. In each figure, the larger bright circle shows the silica bead while the smaller circle indicates the micro-robot. a) The micro-robot carried the silica bead along a densely-packed ellipsoidal path. b) The micro-robot carried the silica bead along a long path with sharp turns.

ical samples is highly desired in these fields. The proposed method is also capable of performing non-contact manipulation on biological samples with minimal damage. Experimental demonstrations were carried out to manipulate human myeloid leukemia HL60 cells as well as multi-flagellated swimming bacteria, as shown in Figs. 2.23 and 2.24, respectively.

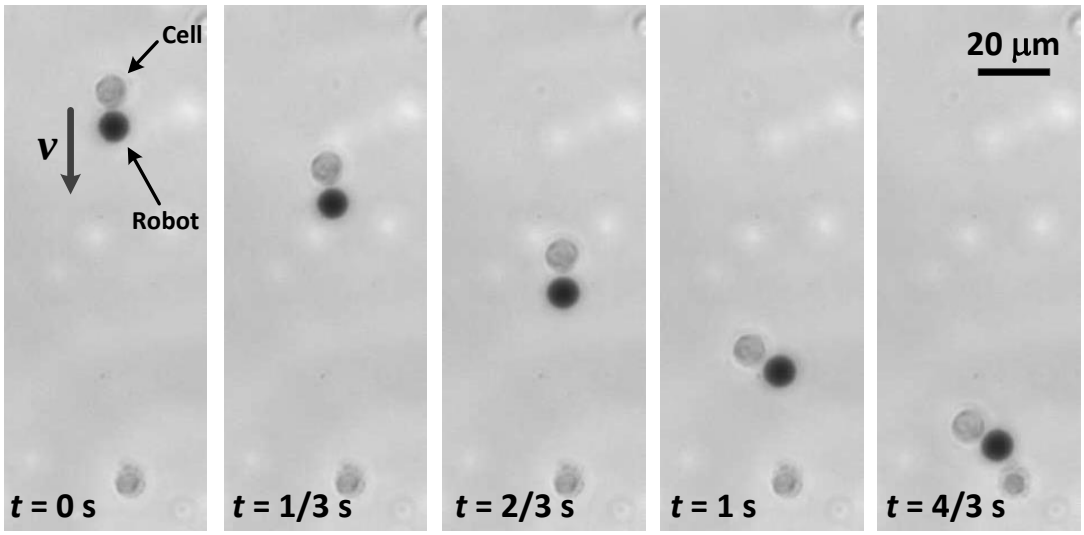

Figure 2.23: Image sequence showing manipulation of a HL60 human cell using a 10 μm-diameter micro-robot. The cell was carried downwards in the image by the micro-robot while orbiting around the micro-robot simultaneously. The rotation speed of the micro-robot was 20 Hz.

In the first experiment, a 10 μm-diameter micro-robot was spun at a speed of 20 Hz with a tilt angle of 78° to perform manipulation of HL60 cells. As shown in Fig. 2.23, a HL60 cell with a size similar to that of the micro-robot was trapped in the induced rotational flows and carried along with the robot to translate on the surface.

According to literature, this type of cell varies from 9 μm to 25 μm in diameter [78]. In fact, not only this type, but most cells show variation in their size, making the proposed method suitable for manipulation of such cells considering its large range of manipulable object sizes. The shear rate, estimated from the results of Sec. 2.4.4, is about 305 /s, with a corresponding shear stress of 0.3 Pa. No damage to animal cells has been reported at such a low shear rate [79], which verifies the safeness of the proposed method for biological micro-manipulation.

In the second experiment, trapping and transport of swimming bacteria was attempted. Such task is even more challenging because a trapping mechanism is necessary to counterbalance the intrinsic motility of the microorganisms to prevent them from escaping. The experiment shows that the proposed method is capable of performing the task. In this experiment, a 5 μm-in-diameter micro-robot was spun at a very high speed of 80 Hz with a tilt-angle of 80° so that a high-intensity rotational flow field could be generated. A bacterium in the vicinity of the rotating micro-robot would experience a strong drag force, which overwhelmed the bacterium's own propulsive force and reoriented the bacterium to align the long axis of its body with the local streamlines. Then the bacterium could be stably trapped around the micro-robot and transported on a surface, as shown in Fig. 2.24. The trapped bacterium could survive the transport process and leave the trap on its own motility once the rotation of the micro-robot stopped.

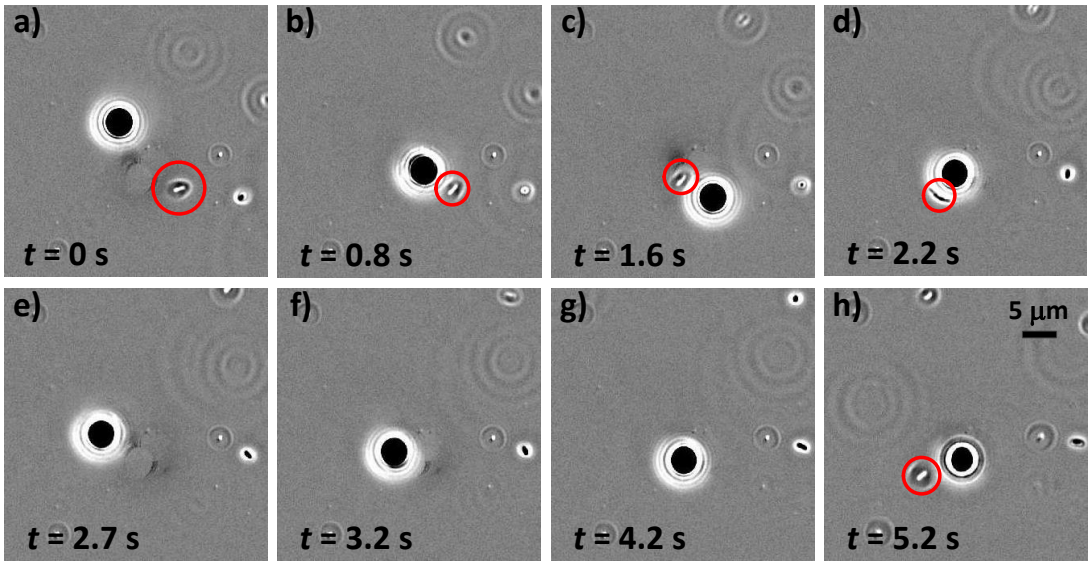

Figure 2.24: Image sequence showing trapping and transport of a multi-flagellated swimming bacterium with a 5 µm-in-diameter micro-robot on a surface. The micro-robot appears as a dark solid circles while the position of the target bacterium is indicated by a red circle on each image if the bacterium is visible. The micro-robot first approached the targeted bacterium by rolling (a)–b)). When it was close to the bacterium, it started rotating at 80 Hz with a tilt-angle $\phi = 80°$, trapping the bacterium in the induced rotational flows and carrying the bacterium along with it when it translated on the surface (c)–f)). After the robot stopped the rotation, the bacterium regained its mobility and swam away (g)–h)). The bacterium stayed close to the micro-robot during transport and merged into its halo on the images, and hence is invisible on e)–g).

2.6 Chapter Summary

This chapter introduced a non-contact 2D micro-manipulation method using rotational flows induced by rotational motion of magnetic micro-robots at low Reynolds number regime. We first proposed that the mechanism could work on two different operating modes. In the first mode, a single mobile micro-robot was used for fast, long-range transportation and fine positioning of one micro-object at a time without a specialized patterned surface. In the second mode, multiple micro-robots were trapped at prescribed positions by the underlying magnetic micro-docks embedded in the substrate and span simultaneously to create virtual fluidic channels for object-manipulation. These virtual fluidic channels could be reconfigured simply by changing the arrangement of the micro-robots. The principles of the proposed method was discussed along with both analytical and numerical analysis of the established physical models. The rotational flows induced by spinning micro-robots with both spherical and non-spherical shapes were investigated, and qualitative analysis was performed on the object behavior in the induced flow region based on the forces it would experience. We experimentally showed that the position of the micro-robot can be precisely controlled by magnetic micro-docks embedded in substrate or by visual-based feedback control on non-specialized surfaces. To verify the proposed method, experimental demonstrations were first carried out at sub-millimeter scale. Manipulation of polystyrene beads using both operating modes were demonstrated. We further implemented automated micro-manipulation using the first operating mode. We also extended the application of first operating mode into micron-scale to verify the scalability and versatility of the proposed method. Various micron-sized objects,

including biological samples of human blood cells and swimming bacteria, were successfully manipulated using the proposed method.

Chapter 3

3D Locomotion by Rotating Flexible Artificial Flagella in Liquids

3.1 Introduction

In the previous chapter, we studied the hydrodynamics of rotating magnetic micro-robots at low Re regime, and used the flows induced by rotational robot motion to implement non-contact micro-manipulation of various micro-object in otherwise quiescent liquids. Sphere is almost the simplest body as it is geometrically isotropic in all directions. When a body with much less symmetry moves inside a liquid, the hydrodynamic interactions become more complex, which may be interesting and useful for other applications. This chapter discusses rotation of a micro-robot with attached elastic artificial flagella inside liquid and the associated hydrodynamics. 3D locomotion of micro-robots is achieved using such appendages based on the hydro-

dynamics.

3D locomotion of miniature robots swimming in liquid has been an ongoing interest for researchers due to its potential applications in biomedicine and microfluidics, such as targeted drug delivery, microsurgery and micro-manipulation [80]. In this chapter, we introduce a 3D propulsion mechanism for magnetic micro-robots to swim in liquid in low Re environments. The cylindrical magnetic micro-robot bodies are attached with flexible artificial flagellum-like propellers. When the magnetic robot body rotates in liquid by an external magnetic field, it conveys the rotation to the attached artificial flagella, which then bend into chiral shapes due to the interaction between elasticity and viscous drags. The chirality of the bent flagella breaks time-reversibility and hence can provide propulsion for the micro-robot body to swim through the liquid.

This mechanism has been adopted by a few other micro-swimmers that are microns in size [21, 81, 82]. While these small swimmers succeed in implementation of 3D locomotion, they only take advantage of one single artificial flagellum as source of propulsion. At a larger scale of several millimeters [83], reported a swimmer that had two flexible wings which used a similar mechanism of rotating these wings to propel itself at low and medium Re. Experiments on meso-scale fixed-end artificial flagella have demonstrated that an increase in number of flagella under some conditions can lead to increase in propulsive force generated [84]. However, real miniature swimming robots taking full advantage of multiple artificial flexible flagella are not yet developed.

In this chapter, we introduce the design and fabrication of the magnetic swim-

ming micro-robot with multiple straight artificial flagella attached. Analytical model is established based on single-flagellum hydrodynamics of straight flagella for analysis of propulsive force generation using numerical method. We further extend this analyzing approach to flagella with intrinsic planar curvatures, which could benefit propulsive force generation and swimming performance. Experimental characterization is eventually performed on swimming performance of fabricated micro-robots.

3.2 Concept

The design of magnetic micro-robots that swim in liquid using propulsion generated by attached artificial multiple flexible flagella is inspired by microorganisms in nature, such as flagellated bacteria. For such flagellated microorganisms, each of their flagella is rotated by an individual micro-motor, and together generate propulsive force for them to swim inside liquid (Fig. 3.1). However, it is difficult to directly duplicate from nature for artificial micro-robots in that fabrication and actuation of micro-robots equipped with multiple, independent micro-motors at small scales remain extremely challenging at present. Therefore, the mechanism of propulsion by rotating flexible flagella is adopted for swimming micro-robots but implemented differently from flagellated microorganisms.

A magnetic swimming micro-robot consists of a cylindrical magnetic body, and flexible non-magnetic artificial flagella of a length of L rigidly attached to the bottom surface of the cylindrical body with a offset distance s_0 and a anchoring angle θ_f from the long axis of the body, as shown in Fig. 3.2. The magnetic robot body

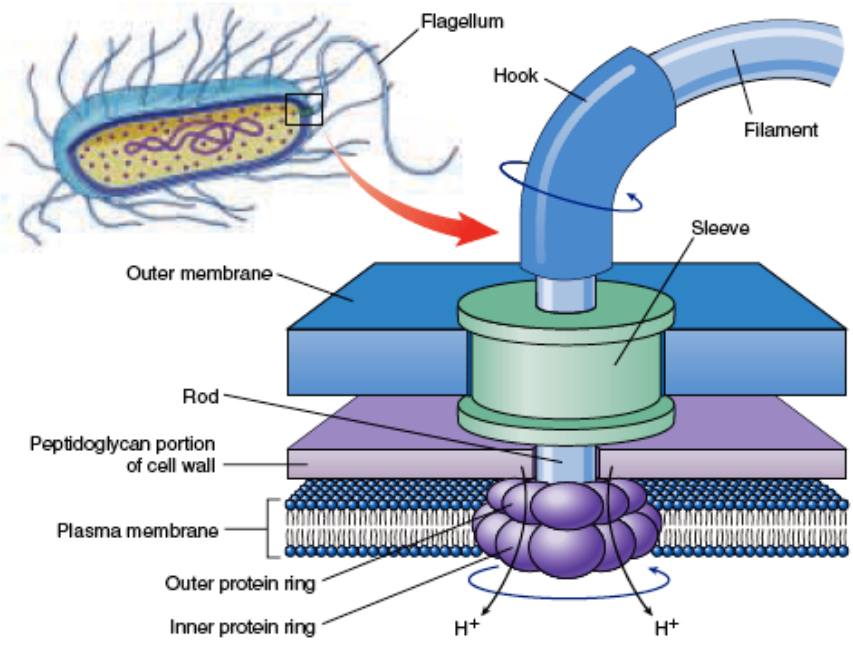

Figure 3.1: The flagellar motor of a gram-negative bacterium. A protein filament, composed of the protein flagellin, is attached to a protein shaft that passes through a sleeve in the outer membrane and through a hole in the peptidoglycan layer to rings of protein anchored in the cell wall and plasma membrane, like rings of ball-bearings. The shaft rotates when the inner protein ring attached to the shaft turns with respect to the outer ring fixed to the cell wall. The inner ring is an H^+ ion channel, a proton pump that uses the passage of protons into the cell to power the movement of the inner ring past the outer one. Figure and caption reprinted from [85].

is magnetized in the direction perpendicular to its long axis. When the swimming micro-robot is exposed to a constantly rotating external magnetic field, its magnetic body responds to the applied field by trying to align its magnetization with the filed direction, which leads to steady rotation of the robot body in a strong enough field. Since the magnetization of the robot body is perpendicular to its long axis, this axis also becomes the axis for rotation of the body. The rotation of the body is conveyed to the attached flagella, which then all rotate in synchrony about the long axis of robot body. Such rotation passively bends the flagella into chiral shapes due to the forces applied from liquid surrounding the flagella. Each of the flagella is a slender body that has a high aspect ratio, and hence the hydrodynamic interactions it experiences in the directions tangential and perpendicular to its surface are different. When deformation of the flagella is fully developed at steady-state, the geometric chirality and the hydrodynamic anisotropy of the flagella together result in a constant net force in the axial direction of the robot body, which can be used to continuously propel the robot body in this direction.

3.3 Experimental Setup

The magnetic swimming micro-robots were actuated and controlled by the six-electromagnetic-coil system introduced in Sec. 2.3.1.

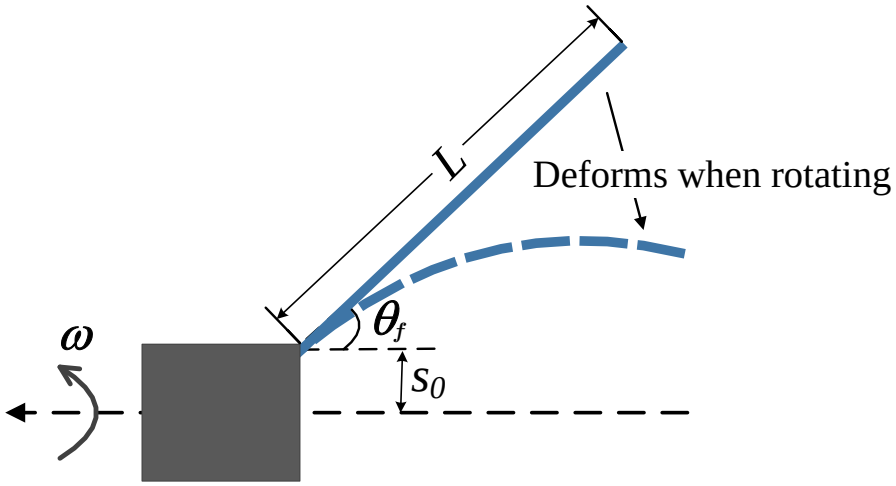

Figure 3.2: 2D side-view schematic of a magnetic single-flagellum swimming robot. The dark square represents the magnetic cylindrical body, while the solid blue line shows the undeformed, non-magnetic artificial flagella. When the robot body rotates, it conveys the rotation to the flexible flagellum which then passively bends into chiral shape, as shown by the curved dotted blue line.

3.3.1 Fabrication of Flagella-Attached Micro-Robots

The miniature swimming robot design in this study consisted of two parts: a magnetic body that could respond to an externally applied magnetic field for actuation and control, and flexible flagella acting as propulsive components during swimming. 3D micro-structures were necessary in order to equip the robots with multiple flexible and tilted flagella, and thus conventional single-step 2D lithography-based fabrication techniques would not be adequate [86]. Therefore, our swimming robots were fabricated by a two-step micro-molding process (Fig. 3.3), which was based on simple and inexpensive planar photolithography methods, micro-molding technique, and manual assembly. The first step was a typical soft-photolithography-based micro-molding process: Photolithography was firstly used to transfer the desired planar patterns that have notches at desired positions for assembling to the SU-8 photoresist substrate; then a mold-making elastomer (silicone rubber, Dow Corning HS II RTV, or polydimethylsiloxane, Dow Corning Sylgard 184) was poured over the patterned substrate to form a negative mold; the planar parts, made of polymer (ST-1060 or ST-1087, BJB Enterprises), were cured and pulled off from the negative mold. After the planar parts were fabricated, we manually assembled them into 3D shapes, each consisting of two to three (only for robots with six flagella) planar parts. Afterwards, a mixture of NdFeB magnet particles (Magnequench MQP-15-7, refined in a ball mill to produce particles under 2 μm in sizech) and polyurethane (TC-892, BJB Enterprises) was poured into another negative rubber mold with blind-ended cylindrical cavities, prepared via a process similar to the first step but using a multi-coating technique to build up a SU-8 layer of 600 μm thickness. The assemblies were then

inserted vertically into the cavities filled with magnetic mixture and allowed to cure for the final 3D shapes. The walls of the cavities as well as the high viscosity of the magnetic mixture helped to maintain the vertical postures of the inserted assemblies. During curing, the negative rubber mold was exposed under a strong magnetic field of 0.3 T parallel to the mold's top surface to magnetize the magnetic robot bodies in the direction perpendicular to their body-axes.

The fabricated swimming robots with straight and flexible flagella can be grouped into three different sets of dimensions and materials. Set I (Fig. 3.4 (a)–(d)) has a cylindrical body of 500 μm (diameter, D) ×600 μm (height, H), and flagella of 120 μm (width, w) ×100 μm (thickness, b) ×1.5 mm (length, L) made of ST-1087 (Youngs modulus of 9.8 MPa, e.g. $E = 9.8$ MPa). Set II (Fig. 3.4 (e)) has the same cylindrical body as Set I, but with flagella of 60 μm (w) ×50 μm (b) ×1 mm (L) made of ST-1060 ($E = 2.9$ MPa). Set III (Fig. 3.4 (f)) has a cylindrical body of 180 μm (D) ×700 μm (H), and flagella of 60 μm (w) ×50 μm (b) ×1 mm (L) made of ST-1060. Besides straight flagella, robots with four planar sinusoidal flagella (Fig. 3.4 (g)) were also fabricated to demonstrate the capability of the proposed fabrication method for creating more complex flagella shapes. Robots with even smaller size could be fabricated through the same process, but the manual assembly process precision would be more challenging, and micro-robotic assembly methods might be required.

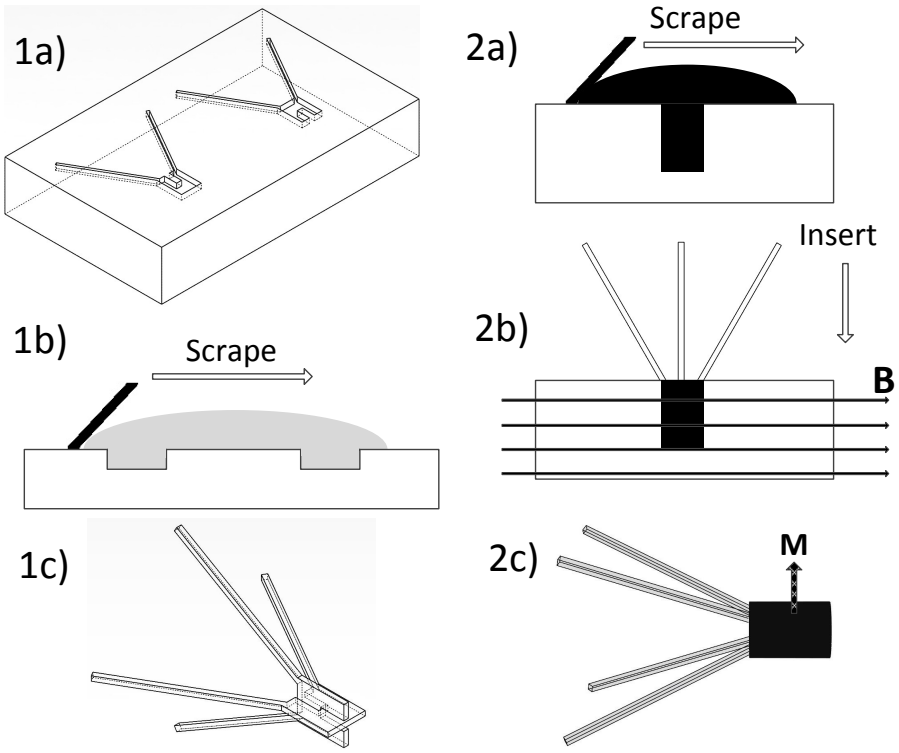

Figure 3.3: Fabrication procedure for the swimming micro-robots with multiple flexible flagella. Step 1: 1a) A flexible negative mold for the planar parts was fabricated via a typical soft-lithography process. 1b) Planar parts were fabricated through a micro-molding process. 1c) Such planar parts were assembled manually into 3D structures. Step 2: 2a) A mixture of magnetic particles (NdFeB) and polyurethane was poured into the cylindrical cavities on another negative mold. 2b) The assembly was vertically inserted into the filled cavities and left to cure. During curing, a horizontal magnetic field is applied to magnetize the robot bodies in the direction perpendicular to their long axes. 2c) The molded robots with multiple flagella were peeled off from the mold.

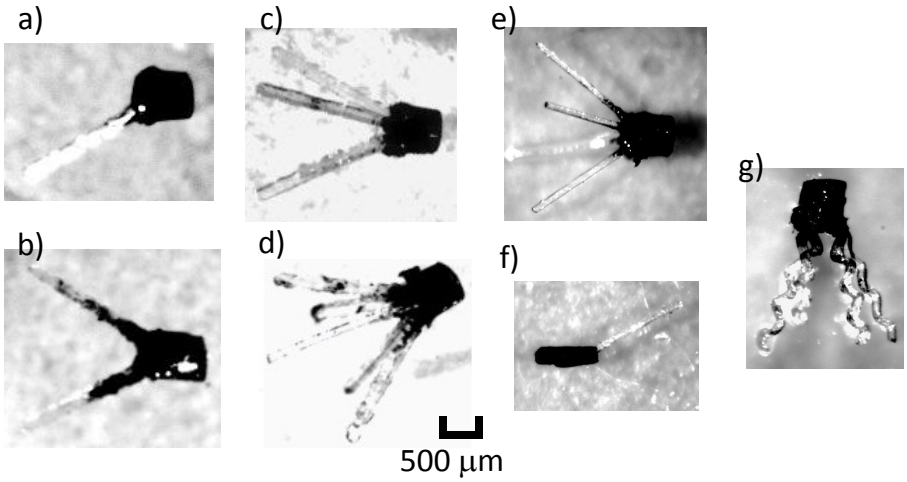

Figure 3.4: Optical microscope images of fabricated swimming micro-robots with different designs. a)–d): Robots with a cylindrical body of 500 µm (D) ×600 µm (H), and flagella of 120 µm (w) ×100 µm (b) ×1.5 mm (L) made of ST-1087 (BJB Enterprises, $E = 9.8$ MPa). e) Robot with a cylindrical body of 500 µm (D) ×600 µm (H), and flagella of 60 µm (w) ×50 µm (b) ×1 mm (L) made of ST-1060 (BJB Enterprises, $E = 2.9$ MPa). f) Robot with a cylindrical body of 180 µm (D) ×700 µm (H), and flagella of 60 µm (w) ×50 µm (b) ×1 mm (L) made of ST-1060 ($E = 2.9$ MPa). (g) Robot with a cylindrical body of 500 µm (D) ×600 µm (H), and sinusoidal flagella made of ST-1087 ($E = 9.8$ MPa).

3.4 Modeling and Simulation

3.4.1 Magnetic Actuation

A swimming micro-robot is rotated along its body axis by an applied rotating magnetic field via magnetic torque. The magnetic torque applied on the robot body is given by eqns. (2.1) and (2.2). Therefore, the maximum magnetic torque can be applied on a cylindrical robot body is

$$|\boldsymbol{T}_{\max}| = V_{\mathrm{m}} |\boldsymbol{M}| |\boldsymbol{B}| \sin\frac{\pi}{2} = \frac{\pi}{4} \frac{D^2 H |\boldsymbol{M}_{\mathrm{NdFeB}}| |\boldsymbol{B}|}{1 + \rho_{\mathrm{NdFeB}} / (\alpha_m \rho_{\mathrm{poly}})}. \tag{3.1}$$

Considering that the planar parts were made of non-magnetic materials in the first step of fabrication, the effective volume V_e of NdFeB in the final robot body would be less than the total body volume V_{m}, typically about 60%$\sim$80% of V_{m}, depending on the geometry of the planar part cross-sections.

3.4.2 Fluidic Drag Force and Torque on Robot Body

The robot body was modeled as a cylinder with a cross-section diameter D and a height H, and the aspect ratio (H/D) is larger than 1. During swimming, the robot body undergoes two simultaneous motions: rotation around its body axis, and translation along the same axis. Due to linearity at low Re, these two motions could be decoupled and analyzed separately, and the complete motion is the linear superposition of the two. The resistive fluidic drag force due to the translational motion of the

cylindrical body is approximated by [87]:

$$\begin{aligned}\boldsymbol{f}_{\text{drag}} &= \\ &-8\pi\mu D\boldsymbol{v}_{\text{swim}}\left(1.0276+0.3963\left(H/D\right)-0.0259\left(H/D\right)^2+0.0014\left(H/D\right)^3\right) \\ &= c_{\text{drag}}\boldsymbol{v}_{\text{swim}},\end{aligned} \tag{3.2}$$

where μ is the viscosity of the fluid and $\boldsymbol{v}_{\text{swim}}$ is the swimming speed of the robot. The resistive fluidic drag torque due to the rotational motion of the cylindrical body is approximated based on the Stokes' law as

$$\boldsymbol{T}_{\text{drag}} = \pi\mu H D^2\boldsymbol{\omega}. \tag{3.3}$$

3.4.3 Elastohydrodynamics of the Straight Flexible Flagellum

When the robot body is rotated by the applied magnetic field about its body axis, it conveys the rotation to the attached flagella that are originally straight. These rotating flagella then experience drag forces from the surrounding viscous fluid as a result of their relative movements to the background liquid. Due to the flexibility of the flagella, they can bend into chiral shapes under these drag forces, and thus produce net thrust. To simplify the problem, we focus only on a single flagellum when formulating the hydrodynamics on the flagellum without considering the hydrodynamic interactions between multiple flagella [88]. Under such an assumption, the total propulsive force or fluidic drag torques of multiple flagella are simply approximated by the linear sum of those generated by each single flagellum. We are also only interested in steady-state motions, and hence the model would be time-invariant. Further ignoring the hydrodynamic interactions between distant parts of

the flagellum, the resistive-force theory gives the viscous drag force per unit length as:

$$\boldsymbol{f}_{\text{vis}} = -\left[\xi_{\perp}\left(1-\boldsymbol{p}_s\boldsymbol{p}_s\right)+\xi_{\parallel}\boldsymbol{p}_s\boldsymbol{p}_s\right]\boldsymbol{u}_{\text{fg}}, \tag{3.4}$$

where $\boldsymbol{p}(s,t)$ is the position vector at arc-length s and time t, and $\boldsymbol{u}_{\text{fg}}(s,t)$ is the velocity of the flagellum at s relative to the background flow $\boldsymbol{v}_b$. If the hydrodynamic interactions between the body and the flagellum are further ignored for simplification and the liquid at distance is assumed quiescent, then $\boldsymbol{u}_{\text{fg}} = \omega\hat{\boldsymbol{z}} \times \boldsymbol{p} - \boldsymbol{v}_b$. $\xi_{\perp}$ and $\xi_{\parallel}$ are the normal and tangential drag coefficients given approximately by resistive-force theory as:

$$\xi_{\perp} = \frac{4\pi\mu}{\log\left(L/a_f\right)+1/2}, \text{and } \xi_{\parallel} = \frac{2\pi\mu}{\log\left(L/a_f\right)-1/2}, \tag{3.5}$$

where a_f is the radius of a flagellum with circular cross-section. Since the flagella on the robots have rectangular cross-sections instead of circular, an effective radius that gives the same cross-section area is used to approximate the drag coefficients:

$$a_{eff} = \sqrt{\frac{b \times w}{\pi}}. \tag{3.6}$$

Since the micro-robot operates inside a container instead of an open space, wall effects are also considered by multiplying the coefficients with a correction term from [89]:

$$\frac{\xi^*}{\xi_{\infty}} = \left(1 - \frac{2.1044\xi_{\infty}L}{6\pi\mu h}\right)^{-1}, \tag{3.7}$$

where ξ_{∞} is the drag coefficient without presence of walls, ξ^* is the drag coefficient adjusted for wall effects, and h is the distance to the walls. The bending force for the elastic flagellum is given by

$$\boldsymbol{F}_{bend} = -A\frac{\partial^3\boldsymbol{p}}{\partial s^3}, \tag{3.8}$$

where A is the bending stiffness of the flagellum. Ignoring the body weight of the flagellum, the steady state shape of the bent flagella is determined by balance of viscous and elastic forces, $\partial \boldsymbol{F}_{bend}/\partial s + \boldsymbol{f}_{\text{vis}} = \boldsymbol{0}$, which gives the governing equation of elastohydrodynamics as

$$\left[\xi_{\perp}\left(1-\boldsymbol{p}_s\boldsymbol{p}_s\right)+\xi_{\parallel}\boldsymbol{p}_s\boldsymbol{p}_s\right]\boldsymbol{u}_{\text{fg}} = -A\frac{\partial^4 \boldsymbol{p}}{\partial s^4}. \tag{3.9}$$

The boundary conditions (b.c.'s) are: i) at the attached end: $\boldsymbol{p}\left(0\right) = \left(s_0, 0, 0\right)$ and $\boldsymbol{p}_s\left(0\right) = \hat{\boldsymbol{x}}\sin\theta_f + \hat{\boldsymbol{z}}\cos\theta_f$; ii) at the free end: both elastic force and torque should be zero, which gives $\boldsymbol{p}_{ss}\left(L\right) = 0$ ($\boldsymbol{p}_{ss} = \partial^2\boldsymbol{p}/\partial s^2$) and $\boldsymbol{p}_{sss}\left(L\right) = 0$ ($\boldsymbol{p}_{sss} = \partial^3\boldsymbol{p}/\partial s^3$).

When the robot body diameter is large or when the rotation frequency is high, the flow generated by the body's rotation would be significant, and hence altering the hydrodynamics on the flagella. A further modification to the previous introduced model can be made to preliminarily examine the effect of hydrodynamic interactions between the robot body and the flagellum when the deflection of flagellum is not significant. The rotational motion of the body induces a rotational flow field around it, and the attached flagellum is also affected by this flow field as the relative velocity of the flagellum to the background liquid is changed. To simplify the problem, we consider a rotational flow field induced by an infinitely long cylinder to approximate the actual flow field:

$$\boldsymbol{v}_b = \omega\frac{\left(D/2\right)^3}{l^2}\hat{\boldsymbol{z}}\times\boldsymbol{e}_l, \tag{3.10}$$

where l is the distance from the axis of the cylinder to the point of interest and $\boldsymbol{e}_l$ is the unit vector in the direction of l. Such an approximation would result in a stronger flow field in the vicinity of the flagellum than the actual field, especially at

the far end away from body, and thus the propulsive force derived would give a lower bound to the actual propulsive force. This modification was only applied to analyze the flagella that are slightly bent during rotation.

3.4.4 Propulsive Force and Drag Torque on the Flagellum

The steady-state deformed shape of the rotating flexible flagellum can be obtained by solving eqn. (3.9) with the given boundary conditions. This is a 3D high-order boundary value problem (BVP), to which the analytical solution is not available. Instead, we use numerical method to obtain approximate solutions. The shooting method similar to [90] is implemented in *MATLAB* to find numerical solutions. The method is structured as follows:

•First, we rewrite the original BVP into an initial value problem (IVP) containing a set of ordinary differential equations with initial conditions given by the original b.c.'s at $s = 0$ and a set of guess values for the unknown b.c.'s.

•A $ode45$ solver is used to solve for the IVP, from which a set of values of b.c.'s at $s = L$ are obtained.

•A function is defined as the difference between the given b.c. values and the values obtained from the previous step at $s = L$.

•A $fsolve$ solver, with the input variables as the guess b.c. values at $s = 0$, is used to find the solutions at which the value of the previously defined function is zero. This indicates that the b.c. values obtained from the $ode45$ solver matches the given b.c.'s at $s = L$, which means the set of solutions we find is a close enough approximation to the true solutions.

After finding the numerical solutions, the propulsive force generated by the deformed flagellum can be obtained from the solutions as

$$\boldsymbol{f}_p = -\boldsymbol{F}_{bend}(0) \cdot \hat{\boldsymbol{z}}, \tag{3.11}$$

while the viscous torque experienced by the whole flagellum is

$$\boldsymbol{T}_f = -A\hat{\boldsymbol{z}} \cdot \boldsymbol{p}_s \times \boldsymbol{p}_{ss}(0) + \hat{\boldsymbol{z}} \cdot \boldsymbol{F}_{bend} \times \boldsymbol{p}(0). \tag{3.12}$$

3.4.5 Swimming Speed

When the robot is swimming with a steady-state speed, the total forces and torques that it experiences should vanish such that

$$\boldsymbol{f}_p + \boldsymbol{f}_{\text{drag}} = \boldsymbol{0} \tag{3.13}$$

and

$$\boldsymbol{T}_{\text{m}} + \boldsymbol{T}_{\text{drag}} + \boldsymbol{T}_f = \boldsymbol{0}. \tag{3.14}$$

Equation (3.14) together with (eqn. 3.1) give the requirement on the strength of the applied magnetic field to rotate the swimming micro-robot in synchrony with the rotating field. In addition, by solving eqn. (3.13) numerically based on eqns. (3.2) and (3.11), we can find the value of steady-state swimming speed $|\boldsymbol{v}_{swim}|$ for every rotation frequency f. To obtain the numerical solution for $|\boldsymbol{v}_{swim}|$, first we notice that when the robot is swimming through an otherwise quiescent liquid with velocity $\boldsymbol{v}_{swim}$, the whole robot sees the background liquid flowing in the opposite direction with velocity of $-\boldsymbol{v}_{swim}$. Then, another $fsolver$ from *MATLAB* with input of $-\boldsymbol{v}_{swim}$ as $\boldsymbol{v}_b$ for eqn. (3.4) is nested outside of the shooting method described in

previous section (Sec. 3.4.4). The function to be solved by this $fsolver$ is the difference between the guessed swimming speed and the $-|\boldsymbol{v}_{swim}|$ calculated through eqn. (3.13). By going through this three-layer algorithm, the swimming speed of a micro-robot at a given f can be obtained numerically.

3.4.6 Flagellum with Intrinsic Planar Curvatures

The proposed fabrication method is capable of fabricating flagella that have much more complex planar shapes other than the simple straight shape. Therefore, it would be helpful if we can model the bending behavior of flexible flagella that have intrinsic planar curvatures and exam the hydrodynamics, as what we have done for the straight ones. We achieved this based on the previous numerical model of the straight and flexible flagellum, but with additional modifications to capture the intrinsic curvatures of the non-straight flagella. The following iteration is established to model the bending of a non-straight flagellum: 1) The original curved flagellum is divided into N_c consecutive segments, labelled from 1^{st} to ${N_c}^{th}$ between the anchoring point of the flagellum on the body ($s = 0$) and the free end ($s = L$). Each segment is treated as a short, straight and flexible flagellum that is fixed at one end and free at the other. 2) The boundary conditions at $s = 0$ of the original curved flagellum is applied onto the 1^{st} segment with a set of guessed boundary conditions applied on the free-end, and then the same governing equations, eqn. (3.9) is solved for this segment. 3) The solutions of $\boldsymbol{p}$, $\boldsymbol{p}_{ss}$ and $\boldsymbol{p}_{sss}$ at the free end of the $(k-1)^{th}$ segment, with $k = 2, 3, \ldots, N_c$, are directly applied as the boundary conditions at the fixed-end for the k^{th} segment, while $\boldsymbol{p}_s$ is revised to capture the intrinsic curvature of the

original flagellum and then added to the boundary conditions. 4) Equation (3.9) is then solved for the k^{th} segment. 5) A shooting method similar to the one introduced in Sec. 3.4.4 is used, iterating from step 1) to step 4), to finally obtain a set of solutions for the ${N_c}^{th}$ segment at the free-end that matches the boundary conditions of the original flagellum at $s = L$. One key step to establish the numerical model for non-straight flagellum is to modify $\boldsymbol{p}_s$ in step 3 of the above iteration to capture the intrinsic curvature of the curved flagellum. This is accomplished by applying to $\boldsymbol{p}_s$ a rotation transformation between the tangential vector at the free-end of the deformed $(k-1)^{th}$ segment and the tangential vector at the fixed-end of the k^{th} segment from the original, undeformed flagellum:

$$ {\boldsymbol{p}_s}^{r} = \boldsymbol{T}_p {\boldsymbol{p}_s}^{on} \tag{3.15} $$

with

$$ \boldsymbol{T}_p = \begin{bmatrix} \frac{\boldsymbol{vr}_x{}^2 + \left(\boldsymbol{vr}_y{}^2 + \boldsymbol{vr}_z{}^2\right)\cos\varphi_r}{|\boldsymbol{vr}|^2} & \frac{\boldsymbol{vr}_x\boldsymbol{vr}_y(1-\cos\varphi_r) - \boldsymbol{vr}_z|\boldsymbol{vr}|\sin\varphi_r}{|\boldsymbol{vr}|^2} & \frac{\boldsymbol{vr}_x\boldsymbol{vr}_z(1-\cos\varphi_r) + \boldsymbol{vr}_y|\boldsymbol{vr}|\sin\varphi_r}{|\boldsymbol{vr}|^2} \\ \frac{\boldsymbol{vr}_x\boldsymbol{vr}_y(1-\cos\varphi_r) + \boldsymbol{vr}_z|\boldsymbol{vr}|\sin\varphi_r}{|\boldsymbol{vr}|^2} & \frac{\boldsymbol{vr}_y{}^2 + \left(\boldsymbol{vr}_x{}^2 + \boldsymbol{vr}_z{}^2\right)\cos\varphi_r}{|\boldsymbol{vr}|^2} & \frac{\boldsymbol{vr}_y\boldsymbol{vr}_z(1-\cos\varphi_r) - \boldsymbol{vr}_x|\boldsymbol{vr}|\sin\varphi_r}{|\boldsymbol{vr}|^2} \\ \frac{\boldsymbol{vr}_x\boldsymbol{vr}_z(1-\cos\varphi_r) - \boldsymbol{vr}_y|\boldsymbol{vr}|\sin\varphi_r}{|\boldsymbol{vr}|^2} & \frac{\boldsymbol{vr}_y\boldsymbol{vr}_z(1-\cos\varphi_r) + \boldsymbol{vr}_x|\boldsymbol{vr}|\sin\varphi_r}{|\boldsymbol{vr}|^2} & \frac{\boldsymbol{vr}_z{}^2 + \left(\boldsymbol{vr}_x{}^2 + \boldsymbol{vr}_y{}^2\right)\cos\varphi_r}{|\boldsymbol{vr}|^2} \end{bmatrix}, \tag{3.16} $$

$$ \boldsymbol{vr} = {\boldsymbol{p}_s}^{op} \times {\boldsymbol{p}_s}^{s}, \tag{3.17} $$

$$ \varphi_p = \arccos\left(\frac{{\boldsymbol{p}_s}^{op} \cdot {\boldsymbol{p}_s}^{s}}{|{\boldsymbol{p}_s}^{op}|\,|{\boldsymbol{p}_s}^{s}|}\right), \tag{3.18} $$

where ${\boldsymbol{p}_s}^{r}$ is the revised $\boldsymbol{p}_s$ for the k^{th} segment, ${\boldsymbol{p}_s}^{op}$ and ${\boldsymbol{p}_s}^{on}$ are the $\boldsymbol{p}_s$ calculated from the original flagellum before deformation of the $(k-1)^{th}$ and k^{th} segment, respectively, and ${\boldsymbol{p}_s}^{s}$ is the $\boldsymbol{p}_s$ at the free-end from solutions of the $(k-1)^{th}$ segment, $k = 2, 3, \ldots, N_c$. $\boldsymbol{vr}_i$ with $i = x, y, z$ denotes the i component of vector $\boldsymbol{vr}$.

The established model was solved for a flagellum of planar sinusoidal shape like that in Fig. 3.4 (g). The peak amplitude of the sinusoidal curve is 75 μm, and there are 3.5 wavelengths within the flagellum with a length of 1500 μm. The propulsive force generated by this non-straight flagellum was compared with the force generated by a straight flagellum that has the same effective length, the same anchoring angle θ_f, and the same bending modulus. The results are plotted in Fig. 3.5. It is observed that, theoretically, an improvement can be achieved in propulsive force generation by having a more complex planar curvature in the flexible flagellum.

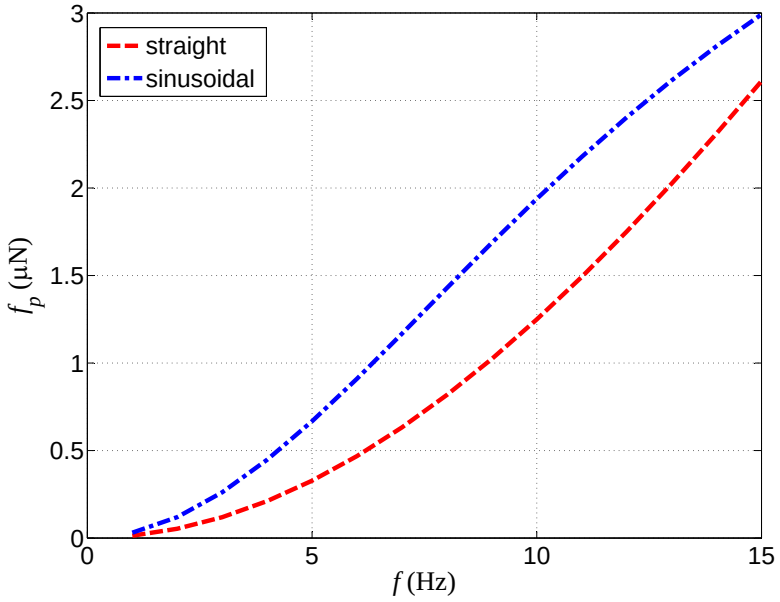

Figure 3.5: Comparison between the propulsive force (f_p) generated by a sinusoidal flagellum and a straight flagellum that differ in shape as a function of rotation frequency. Both results are numerical solutions from the models established in this work.

3.5 Flagellum Design Optimization

The previously established model can be used to find the optimal design of flagellum for the swimming robots. There are various parameters of a flagellum that can be modified, among which the major ones that are easy to adjust are length of the flagella L, anchoring tilt angle at the base θ_f, connection offset distance s_0, and the material elastic modulus E. These parameters could have significant influences on the resulting propulsive force and fluidic drag torque. To find a flagellum design that generates large propulsive force, we first look at how each of these four parameters individually influences propulsive force by varying only one parameter at a time while keeping others constant, and examine the output propulsive forces from numerical calculation. Such results are plotted in Fig. 3.6 (a)–(d), where each subplot shows how the propulsive force generated changes as the value of each of the four parameters varies. It is observed that f_p increases monotonically as s_0 increases. For the other three parameters, f_p shows a peaking behavior as the parameters increase. This means that an optimization search on L, E and θ_f would be necessary. To find the optimal design that gives a global maximum of propulsive force, the $patternsearch$ function built in *MATLAB*, which finds minimum of function using pattern search algorithm, was applied with four input variables L, E, θ_f and s_0. The stopping criteria for the search function were set as: $1e^{-10}$ for tolerance on the minimum distance between the current points at two consecutive iterations and $1e^{-12}$ for the minimum tolerance for the objective function. It should be noted that although f_p increases with s_0, the minimum robot body diameter D required to provide such s_0 becomes larger as well. Therefore, according to eqn. (3.2), the smallest possi-

ble c_{drag} also increases, resulting in a less significant change in swimming speed. This influence of c_{drag} is also considered during the search for the optimal flagellum, and the optimization goal is modified so as to find the largest f_p/c_{drag} based on smallest possible c_{drag}. The optimization search was carried out for two different flagellum cross-section geometries: 120 μm (w)×100 μm (b) and 60 μm (w)×50 μm (b). All of the calculations assume the surrounding liquid has a dynamic viscosity of 0.343 Nsm^{-2}, so as to keep Re satisfying the low Re criterion. The range of rotation frequency f in which the optimization search was carried out is from 0 Hz to 15 Hz. The ranges of L, E, θ_f and s_0 within which the optimization search was carried out were: [0.3 mm, 2.5 mm] for L, [0.05 MPa, 10 MPa,] for E, [0°, 70°] for θ_f and [0, 200 μm] for s_0. The results are listed in Tables 3.1 and 3.2.

Optimization results show that the optimal flagellum would be anchored on the rotation axis of the robot body with zero offset, i.e. $s_0 = 0$. In that case, the maximum swimming speed would be achieved by attaching the flagellum to a robot body with diameter $D = w$. The maximum swimming speed achievable at f =15 Hz would be about 12 mm/s for w =120 μm, and 5 mm/s for w =60 μm. Such performance is comparable to the existing micro-swimmers [21]. However, according to eqn. (3.1), to provide enough driving torque to rotate such optimal flagellum with the hardware currently available, the aspect ratio of the body needs to be greater than 20:1, and hence the fabrication of such body would be difficult. Therefore, in this study, we did not adopt the optimal flagellum design. However, the optimization does give insight to how large an f_p we could possibly obtain by varying flagellum geometry, and could be beneficial to the design of flagellum.

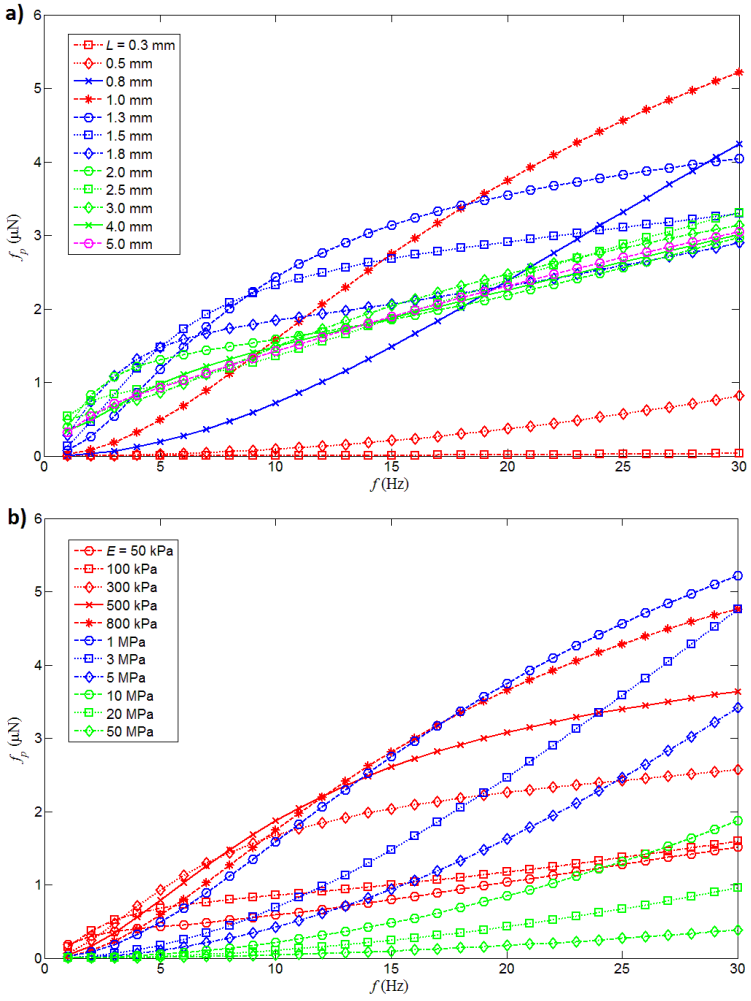
a)
L = 0.3 mm
0.5 mm
0.8 mm
1.0 mm
1.3 mm
1.5 mm
1.8 mm
2.0 mm
2.5 mm
3.0 mm
4.0 mm
5.0 mm
f_p (μN)
f (Hz)
b)
E = 50 kPa
100 kPa
300 kPa
500 kPa
800 kPa
1 MPa
3 MPa
5 MPa
10 MPa
20 MPa
50 MPa
f_p (μN)
f (Hz)

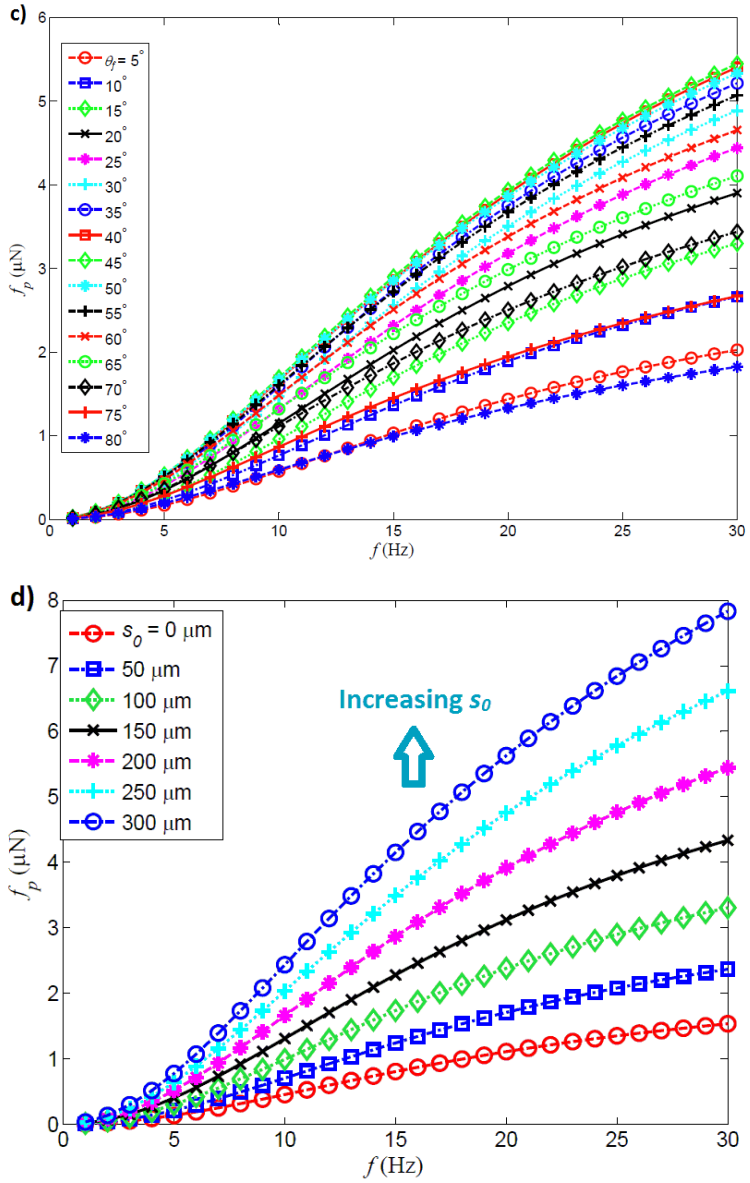

Figure 3.6: Simulation results to show the influence of L, E, θ_f and s_0 on propulsive force. Propulsive force results as a function of rotation frequency when a) changing only L, with $E = 1\,\text{MPa}$, $\theta_f = 35°$ and $s_0 = 190\,\mu\text{m}$; b) changing only E, with $L = 1\,\text{mm}$, $\theta_f = 35°$ and $s_0 = 190\,\mu\text{m}$; c) changing only θ_f, with $L = 1\,\text{mm}$, $E = 1\,\text{MPa}$ and $s_0 = 190\,\mu\text{m}$; and d) changing only s_0, with $L = 1\,\text{mm}$, $E = 1\,\text{MPa}$ and $\theta_f = 35°$.

Table 3.1: Optimal flagellum design for cross-section geometry of 120 μm (w)×100 μm (b).

Rotation frequency f	Flagellum L	Flagellum E	θ_f	s_0	f_p	T_f
15 Hz	2.2 mm	10 MPa	53°	0 μm	4.79 μN	5.78×10^{-5}N·m

Table 3.2: Optimal flagellum design for cross-section geometry of 60 μm (w)×50 μm (b).

Rotation frequency f	Flagellum L	Flagellum E	θ_f	s_0	f_p	T_f
15 Hz	1.1 mm	10 MPa	53°	0 μm	1.15 μN	0.71×10^{-5}N·m

3.6 Experimental Results and Discussion

All experiments are carried out in a cylindrical open-top container with an inner diameter of 33 mm and a height of 37 mm, filled with silicone oils. Actuation of the micro-robots is realized by the rotating magnetic field of $|\boldsymbol{B}|$ =12 mT generated by the electromagnetic-coil system with iron cores inserted into the coils to magnify the field. Three velocity measurements are taken for each set of data, and the errorbars on the result plots indicate standard deviation of the measured values. The micro-robot sinks vertically in the container during swimming horizontally as it is heavier than silicone oil. Therefore, to ensure that robot does not get too close to the bottom surface of the container while the data are taken, the focal plane of optics for the CCD camera on the actuation system is set to be on the upper half of the container. We begin to record videos only when the micro-robot comes into focus. The micro-robot continues to descend, getting out of focus. However, due to the high viscosity of the

silicone oil, the sedimentation of the micro-robot is relatively slow. There will be about a 2 s duration before the robot becomes significantly blurry on the image, and the video recording stops once after this duration. To obtain the swimming speed of the micro-robot, videos of the workspace taken from the CCD camera are imported into *MATLAB* as image frames. The original images are then converted into black-and-white binary images with the threshold adjusted to show the pattern of the robot body. The position of the micro-robot is determined by the center of the pattern of the robot body. The position differentiated over time is used to calculate the average swimming speed of a micro-robot over the video durations.

3.6.1 Verification of the Single-Flagellum Model

An experiment is carried out to examine the validity of previously established single-flagellum model. The comparison of swimming speeds of a single-flagellum micro-robot that are solved from the original model, the model modified with body rotation and obtained from experiments is illustrated in Fig. 3.7. The robots parameters are listed in Table 3.3. All the swimming speed data are normalized by the robot body height H, which is 600 μm. In the experimental result, the swimming speed drops after the rotation frequency reaches 12 Hz because that the rotation of robot body steps out of synchrony with the rotating magnetic field due to lack of enough driving torque.

The comparison shows that the solutions from both models bound the experimental measurements well. This demonstrates that, in the small-deformation case, the original model would give an upper bound to the swimming speed of the swim-

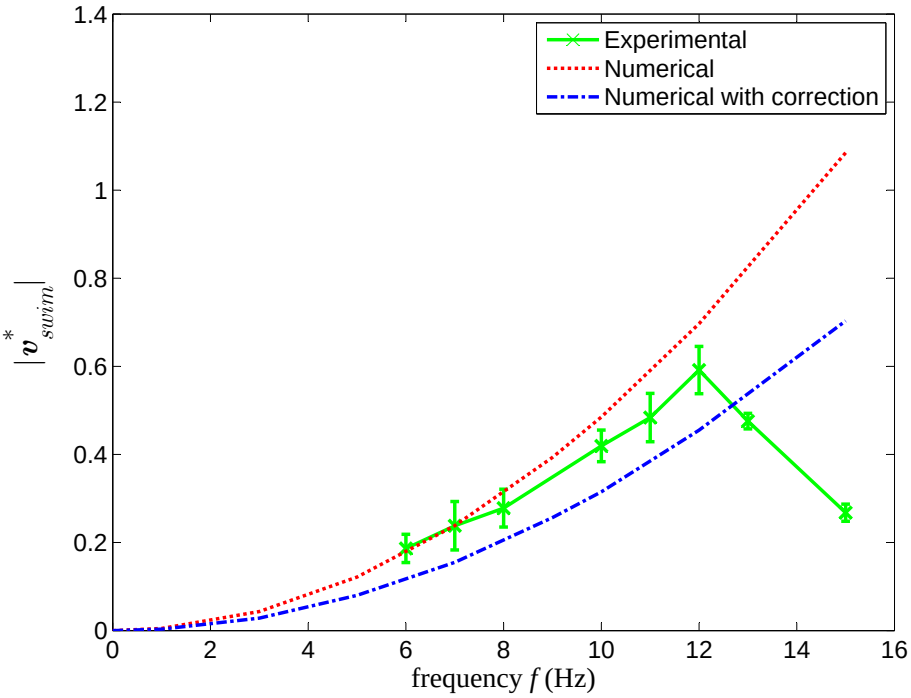

Figure 3.7: Comparison between the swimming speeds solved from the original model, the modified model that includes the body influence, and those obtained experimentally at various rotation frequencies. The swimming speeds are normalized to $|\boldsymbol{v}^*_{swim}|$ by the robot body height H of 600 μm.

Table 3.3: Parameters of the single-flagellum robot, the steady-state swimming speed of which was measured experimentally as well as solved by both the original model and model with background flow modification.

Body H	Body D	Flagellum L	Flagellum w	Flagellum b
600 μm	500 μm	1500 μm	120 μm	100 μm
Flagellum E	θ_f	s_0	μ	-
9.8 MPa	30°	190 μm	0.343 Nsm^{-2}	-

ming micro-robot, while the modified model would give a lower bound.

3.6.2 Effect of Number of Artificial Flagella

Swimming speed measurements were taken on the Set I micro-robots in a silicone oil of 350 cSt viscosity (Re$\sim 10^{-3}$), and the results are plotted in Fig. 3.8. It is observed that the swimming speed is significantly improved by increasing the number of attached flagella (N_{fl}) from one to four. The swimming speed is linearly increasing with N_{fl}, and the experimental results match the numerical solutions. However, as the number of flagella increases to six, the resulting swimming speed decreases significantly. This may be due to the hydrodynamic interactions between flagella becoming stronger as the spacing between flagella becomes smaller. Each flagellum is affected by the fluid flow generated by the motion of nearby flagella, and thus the relative speed $\boldsymbol{u}_{\mathrm{fg}}$ decreases which leads to a lower propulsive force.

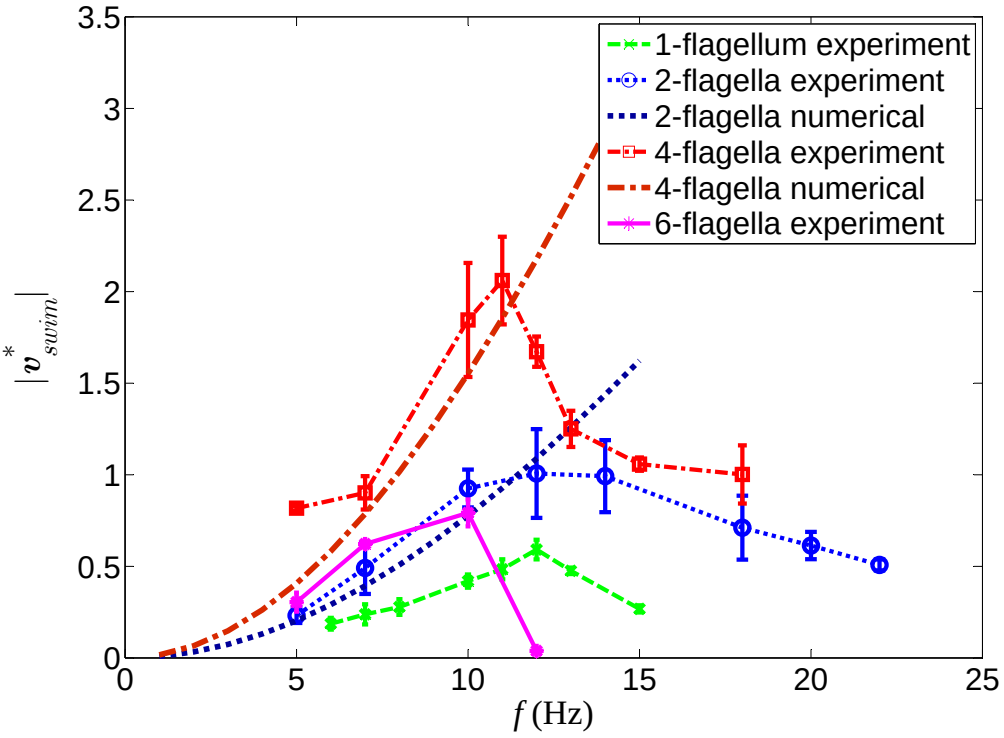

Figure 3.8: Experimental comparison on swimming speed as a function of rotation frequency of micro-robots with 1, 2 and 4 artificial flagella in Set I dimension (Robot body: 500 µm (D) ×600 µm (H); flagella: 120 µm (w) ×100 µm (b) ×1.5 mm (L), and $E = 9.8$ MPa, $\theta_f = 35°$ and $s_0 = 190$ µm). $|\boldsymbol{v}^*_{swim}|$ is the swimming speed, $|\boldsymbol{v}_{swim}|$, normalized by the robot body height H of 600 µm. Swimming speed derived from numerical solutions are also provided for micro-robots with 2 and 4 artificial flagella.

3.6.3 Effect of Flagella Geometry and Reynolds number

Comparisons of the swimming speed of swimming micro-robots with single flagellum in Set I ($L = 1.5$ mm, $E = 9.8$ MPa, $\theta_f = 30^\circ$ and $s_0 = 190$ μm) and Set III ($L = 1$ mm, $E = 2.9$ MPa, $\theta_f = 35^\circ$ and $s_0 = 60$ μm) were also carried out, and the results are illustrated in Fig. 3.9. It can be seen that the swimming speed can be improved by varying the robot design, as analyzed in Sec. 3.5. But even if the dimensions of the body and attached flagellum, as well as the material used for flagellum, are significantly changed, the swimming speed is improved only by a limited margin. In addition, even if the optimal design of flagella is used, by increasing the number of flagella can still significantly improve swimming performance, which is illustrated in Sec. 3.6.2. This demonstrates the advantage of having multiple artificial flagella on a swimming micro-robot.

[htpb] Measurements were also taken for miniature swimming robots in Set II with four flagella in silicone oil with two different kinematic viscosities of 5 cSt and 350 cSt, respectively, and the results are plotted in Fig. 3.10. It is observed that even at mid Re environment (5 cSt oil, Re up to 0.5), the artificial flagella can still generate a strong enough propulsive force for the robot to swim. Therefore, the miniature swimming robots would be potentially capable to work in a wide range of liquids with different viscosities. We also demonstrated that the swimming micro-robot can also swim inside a water-filled glass tube with a diameter of 5.5 mm, as shown in Fig. 3.11.

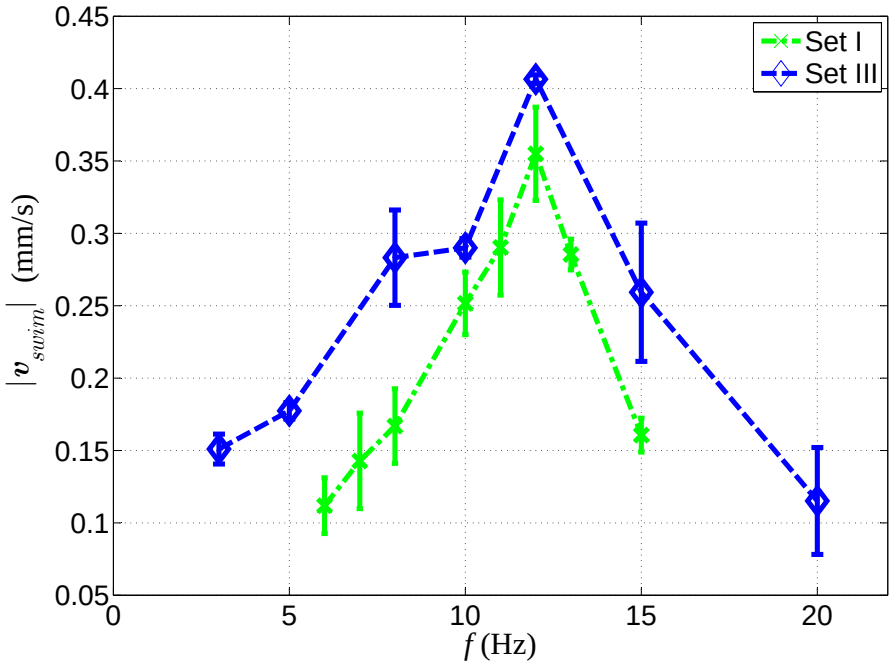

Figure 3.9: Experimental comparison on swimming speed as a function of rotation frequency of single-flagellum micro-robots in Set I (Robot body: 500 µm (D) ×600 µm (H); flagella: 120 µm (w) ×100 µm (b) ×1.5 mm (L), and $E = 9.8$ MPa, $\theta_f = 35°$ and $s_0 = 190$ µm) and Set III (Robot body: 180 µm (D) ×700 µm (H); flagella: 60 µm (w) ×50 µm (b) ×1 mm (L), and $E = 2.9$ MPa, $\theta_f = 35°$ and $s_0 = 60$ µm).

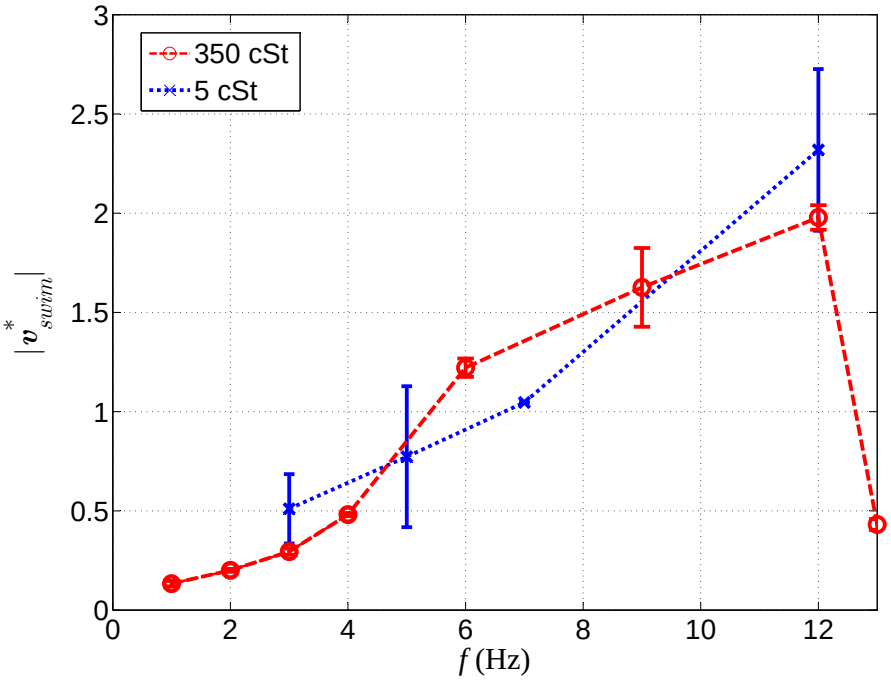

Figure 3.10: Experimental comparison of swimming speed as a function of rotation frequency of swimming robots with four flagella in silicone oil with viscosities of 5 cSt and 350 cSt, respectively.

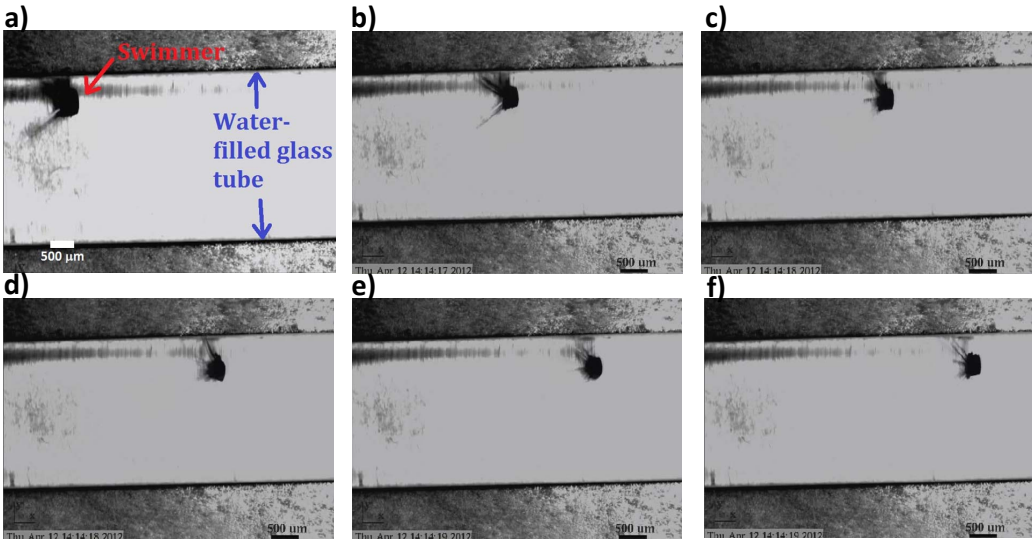

Figure 3.11: Demonstration of a 4-flagellum swimming micro-robot operating inside a water-filled circular-cross-section tube with an inner diameter of 5.5 mm. Images b) to f) are taken from the video demonstration at different frames in sequence with a constant time interval of 0.5 s.

3.6.4 Flagella with More Complex 2D Shape

As previously mentioned, the proposed fabrication method is capable of fabricating more complex planar shapes than the simple straight shape for flagella. Miniature robots with four sinusoidal flagella attached were fabricated, and their swimming speed in 350 cSt silicone oil was measured and compared with that of the robot in Set I with four straight flagella. Figure 3.12 illustrates the experiment results. It shows that the swimming performance could potentially benefit from a more complex flagella design. Considering that the fabrication process for flagella with a non-straight 2D shape is generally identical to the process for straight flagella, robots with non-straight flagella that may have a significantly improved swimming performance can be easily fabricated with the method proposed in this work. In addition, it is possible to locally and drastically adjust the intensity of hydrodynamic interactions between multiple attached flagella by changing the curvature design of them, which provides a potentially powerful tool to study the multiple-flagella hydrodynamic interaction.

3.6.5 Advantages and Limitations of Using Multiple Flagella

The experiment results demonstrated that multiple straight, flexible flagella provide enhanced propulsion. Therefore, one significant advantage of using multiple flagella is that a much higher propulsive force, and hence the resulting swimming speed, can be achieved at a given rotation frequency. In other words, using multiple flagella lowers the rotation frequency required to achieve a desired swimming speed or propulsive force. However, whether or not multiple artificial flagella can improve the maximum swimming speed $max|\boldsymbol{v}_{swim}|$ for miniature robots would need further

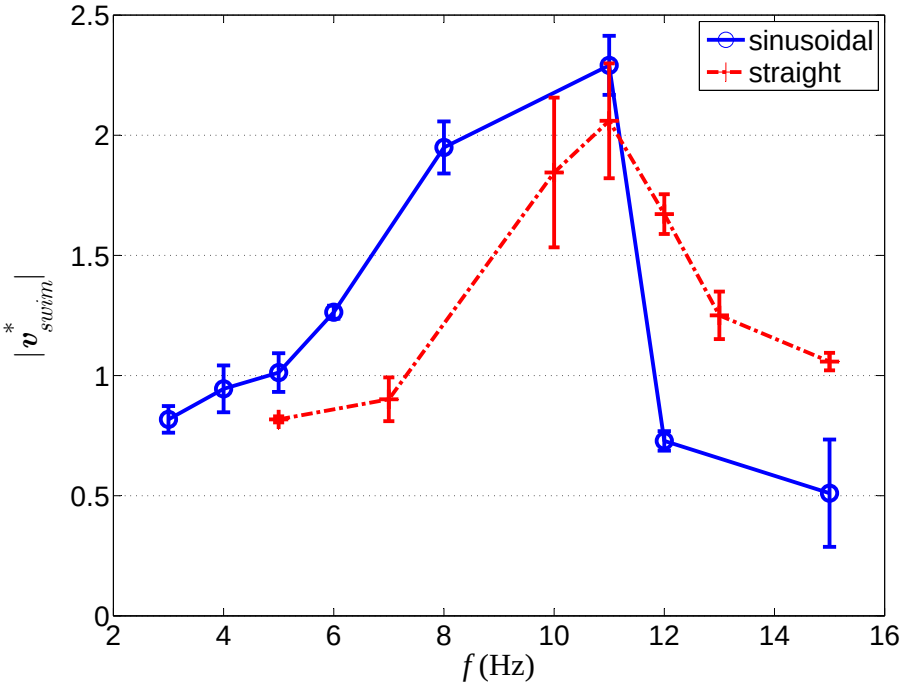

Figure 3.12: Comparison of swimming speed as a function of rotation frequency of the swimming micro-robot with four straight and sinusoidal flagella, respectively.

analysis. While the propulsive force is improved by multiple flagella, the total viscous torque applied on these flagella also increase. As shown by experiments, when hydrodynamic interactions between multiple flagella are not significant, the swimming speed is almost linearly increased by the number of flagella (N_{fl}). Therefore, it is reasonable to assume that the propulsive force and viscous torque also linearly increase with N_{fl}. Previous studies have shown that, for a single straight, flexible flagellum, the relationship between f_p generated and T_f required is $(\log f_p \log T_f)$ >1 [91, 92], which indicates that $f_p = k_{const} T_f^{\beta}$ with β >1. It is also observed in the experiments that when the rotation of robot steps out of synchrony with the rotating magnetic field, the robot begins to oscillate back and forth and its swimming speed begins to drop rapidly as the rotation frequency keeps rising. Therefore, $max|\boldsymbol{v}_{swim}|$ is reached right before stepping-out. Stepping-out occurs when the maximum magnetic torque that can be applied onto the robot is less than the driving torque required to rotate the robot at a given rotation frequency: $|\boldsymbol{T}_{\text{max}}| < (|\boldsymbol{T}_{\text{drag}}| + T_f)$. Therefore, given a limited applied $\boldsymbol{B}$ magnitude, multiple flexible artificial flagella would lead to a significant improvement on $max|\boldsymbol{v}_{swim}|$ when $|\boldsymbol{T}_{\text{drag}}| / (N_{fl} \cdot T_f) \gg 1$. If T_f is comparable to $|\boldsymbol{T}_{\text{drag}}|$, then max$|\boldsymbol{v}_{swim}|$ of a multi-flagella robot could be smaller than that of a single-flagella robot with the same flagella and robot body design. This could be a potential disadvantage of using multiple flagella. In our case, drag torque on the robot body dominates that on the flagella as the step-out frequencies of the robots do not change significantly with number of flagella, and hence we did not expect this potential drawback.

3.7 Chapter Summary

In this chapter, we studied the hydrodynamic interactions on the rotational motion of an elastic, flagellum-like object with surrounding liquid, and introduced a swimming micro-robot design with multiple flexible artificial flagella of number up to six using such interactions to generate propulsion. The fabrication of the micro-robots was inexpensive and relatively simple, including two steps of procedure consisting of soft-lithography, micro-molding and assembly. Numerical models were established to predict the swimming performance of the robots, and optimization was carried out on the flagellum design. Experimental results for robots with straight flexible flagella designs demonstrated that stronger propulsive force, and hence the resulting swimming speed of robots, could be achieved by increasing the number of artificial flagella at a given rotation frequency, as long as the hydrodynamic interactions between flagella are not so significant as to affect the swimming performance. The proposed fabrication method is also shown to be capable of creating more complicated planar flagella designs, such as sinusoidal curves, which may benefit propulsive force generation and swimming performance and could be potentially useful for more sophisticated tasks such as object transportation or manipulation. Increasing the number of artificial flagella has been shown as a promising way to improve swimming performance of swimming micro-robots in liquid environments with a wide range of viscosities.

Chapter 4

Rotational Flows Induced by Micro-Robots inside Microfluidic Channels for Size-Based-Sorting Applications

4.1 Introduction

In previous chapters, we have studied the hydrodynamic interactions between the rotational motion of micro-robots and otherwise quiescent liquids, both when the robots are on planar surfaces and when they are far away from any walls. We have also introduced some direct applications based on these interactions, such as non-contact micro-manipulation and 3D robot locomotion in liquid. In this chapter,

we further extend the previous studies to the case where the liquid surrounding the micro-robots flows at non-zero velocity. This would be a common scene in many applications inside microfluidic channels, in which liquid (and possibly with other micro-objects immersed) needs to be pumped into and then pushed out of the channels continuously. One of the continuous operations that we aim to implement with the rotating magnetic micro-robots in this thesis work is size-based particle-sorting.

When the there is a background flow inside a confined space such as a microfluidic channel, the hydrodynamics on rotating magnetic micro-robots exposed in such flow could be significantly different from the cases of otherwise quiescent liquids that have been studied in previous chapters. The rotational flow generated by a rotating micro-robot will alter the original background shear flow locally in its vicinity. Due to the mobility of the magnetic micro-robot, it can be placed anywhere inside the microfluidic channel. The capability of the mobile magnetic micro-robots to generate local flows at almost any desired locations inside microfluidic channels is one major advantage of this approach comparing to the other existing flow-manipulation methods [93, 94, 95, 96, 97, 98].

The concept of integrating magnetism with microfluidics is particularly attractive because the magnetic fields can be applied at relatively large distances, through insulating, opaque materials, and selectively generate large forces on magnetic materials with no deleterious effects on biological entities. Magnetic forms of separating forces are already widely used in biological science, especially in magnetically activated cell sorting (MACS) [99, 100], magnetophoresis [53], purification of DNA, proteins, and peptides [101, 102], and immunoassays [103]. These methods typically

attach a magnetic particle to a cell or protein via high specificity ligands or covalent immobilization, or require significant difference in intrinsic magnetic properties of samples. While excellent for high-throughput capture of species of interest, these methods typically involve added labeling and label-removal steps, or are applicable for only limited types of samples due to the requirement that the samples need to be magnetically responsive. The integration of magnetic micro-robots with microfluidics is a promising alternative that does not require the samples to directly respond to the externally applied field. Instead, the magnetic forces/torques are only applied on the robots to rotate them to induce rotational flows. The forces for manipulation and separation of samples are provided from the fluid flows around the rotating micro-robots, and hence no magnetic labeling or intrinsically active magnetic properties are necessary for the samples to be handled by the proposed method.

In this chapter, we first introduce the fundamental principles for using the rotational flows induced by rotating magnetic micro-robots inside microfluidic channels for size-based micro-particle sorting. Numerical simulations are performed to study the flow patterns inside microfluidic channel in the presence of both a background flow and the rotational flows induced by magnetic micro-robots. Analysis is carried out on the lateral forces applied on the micro-objects by the surrounding shear flow inside the channel. For holding micro-robots in place inside microfluidic channels, magnetic docking substrates is developed at an order of magnitude smaller than previously introduced in Chapter 2. The proposed method is experimentally demonstrated to be capable of diverting micro-particles from their original paths based on their sizes in continuous flow. We also investigate the use of a new

method of nanofabrication, two-photon polymerization (TPP), for crafting magnetic micro-robots with various shapes from UV curable photoresist polymers containing magnetic nanoparticles (MNP's). We discuss the advantages and limitations of both approaches.

4.2 Proposed Concept

The same mechanism of inducing rotational flows by rotating magnetic micro-robots introduced in Chapter 2 can be borrowed here for microfluidic applications. The key difference is that instead of operating inside an otherwise quiescent liquid far away from the top boundary and side walls, the micro-robot will be placed in a non-zero background flow inside an enclosed space - the microfluidic channel. Due to the wall-effect and the background flow, the hydrodynamic interactions between the rotational motion of the micro-robot and the surrounding liquid are more complex than those in the quiescent liquid case. However, the phenomenon that we observed in Chapter 2 - the size/shape-dependent trapping effect of objects inside rotational flows induced by rotating micro-robots should still remain valid as long as the appropriate robot size and object size are selected and the low Re requirement is satisfied.

When the micro-robot system introduced in Chapter 2 is presented in a background flow, the induced rotational flow can be superimposed onto the background flow given the linear nature of the flows at very low Re. When any micro-objects originally following the background flow enter the region significantly disturbed by the induced rotational flows, they begin to experience the forces arising from the

robot-induced rotational flows, similar to the forces discussed in Section 2.4.4. In this region, not only do these forces change the speed of the objects, but they could also cause migration of objects between streamlines. Since these forces are dependent on the size of objects, the degree of migration is also associated with object size. Therefore, the size-dependent lateral migration enables the generation of size-gradients of micro-objects as they exit the disturbed flow region.

4.3 Experimental Setup

The magnetic micro-robots were driven by magnetic field that was remotely applied by the second electromagnetic-coil system introduced in Sec. 2.3.1. Details of the actuation system can be found in Append. A.2.

4.3.1 Spherical Magnetic Micro-Robots

The spherical magnetic micro-robots were obtained via a procedure introduced in Sec. 2.3.2. We separated the NdFeB powder by size using a stack of four high precision stainless steel sieves (H&C Sieving Systems) with cutoff mesh sizes of 63, 45, 32, and 20 μm (U.S. #230, 325, 450, and 625 respectively). During experiments, the unmagnetized micro-particles could be easily handled and placed onto the substrates or injected into the microfluidic devices. They could then be manipulated into place using the eletromagnetic-coil system, which can induce weak magnetization and motion without causing the micro-robot to significantly agglomerate. Once positioned, the micro-robots were magnetized by placing the substrate or microfluidic

device into a stationary field with a strength of 100–200 mT provided by permanent magnets. After magnetization the micro-robots were far more responsive to external magnetic fields, but also tended to irreversibly attach to nearby robots unless held in place using the magnetic micro-docks built into the surface of the substrate.

4.3.2 Magnetic Micro-Docks

The magnetic micro-docks used here were at an order of magnitude smaller than the ones previously reported in Chapter 2. Since the fabrication techniques used for the larger micro-docks are unable to handle such small structures, other fabrication methods were adopted for preparation of substrates with embedded magnetic micro-docks at small scales.

Nickel docking substrates were fabricated using traditional lithographic techniques and RF plasma sputtering. Glass wafers (4 in. diameter, 0.5 mm thickness, roughness $<$20 Å) were cleaned with acetone and 2-propanol prior to oven-based application of an HMDS adhesion promoter. A negative photoresist (AZ-5214E, MicroChemicals GmbH) was spun on the treated wafer at 6000 rpm for 45 seconds to create a 1.1 µm-thick film. After a 2 minutes, 95°C softbake, the wafer was exposed on a Karl S*ü*ss MA6 aligner for 50 seconds in vacuum contact mode, using a chrome photomask of the desired dock geometries (Photosciences Inc.). Immediately after exposure, the wafer was baked at 105°C for 30 seconds and 115°C for 2 minutes to crosslink the exposed regions (bulk field). Following a 150-second flood exposure (no mask), the wafer was developed in a 1:4 solution of AZ-400K developer diluted in deionized (DI) water, with gentle agitation for 0.8 minutes (48

seconds), then rinsed thoroughly in DI water and dried. Oxygen plasma (100 W forward power, 1 minute) was used to descum the exposed regions before sputtering. RF sputtering of metallic nickel was performed in a Perkin Elmer 8L, using an argon pressure of 12.5 mTorr and 100 W forward power for 60 minutes (with a 10-minute pre-sputtering). The resulting nickel features, after acetone lift-off of the resist layer, were measured with a contact profilometer.

Dock features were fabricated in three geometries (circle, square, and donut) with diameters of 10–40 μm (circle and square) or 5:15–30:90 μm (donut, inner:outer diameter). Docks were arranged in regularly spaced arrays with spacing between docks at 1, 3, 5, and 10 times the diameter, such that all permutations of shape, size, and spacing were represented on each substrate fabricated (see Fig. 4.1). Additional substrates were fabricated in the same manner with docks positioned appropriately for bonding of a polydimethylsiloxane (PDMS) channel such that micro-robot spinning could be evaluated under flow (see Fig. 4.2).

4.3.3 Microfluidic Channels

Microfluidic channels were molded in PDMS using the same procedures as in previous work [104]. Briefly, a silicon wafer was patterned with a protective photoresist, and reactive ion etching was used to create a negative impression of the channel geometry. After etching, the mold was coated in a flourinated silane to facilitate release of cured PDMS. Sylgard 184 (Dow Corning) was mixed in a 10:1 ratio, degassed, and poured over the mold. After curing for 24 hours, the mold was baked for 1 hour at 75°C. The cured channels were diced and removed from the mold prior to bonding.

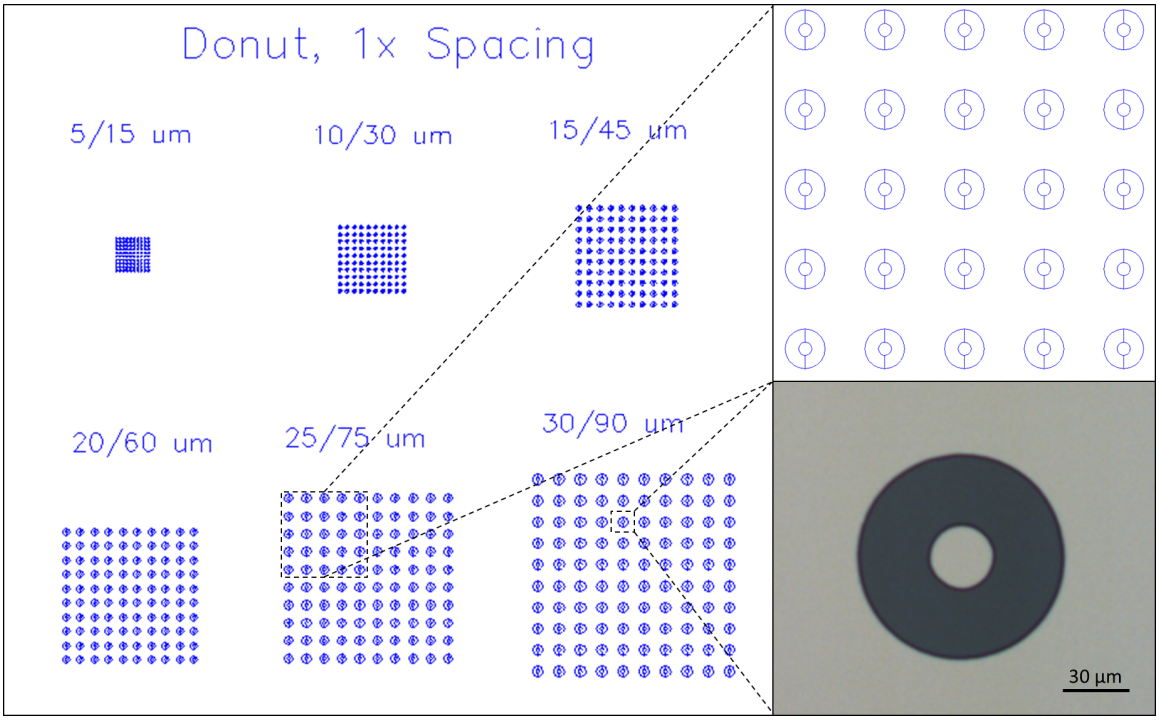

Figure 4.1: AutoCAD model of subsection of magnetic docking arrays, showing donut shaped docks with 1 diameter spacing. Diameters are labeled on the substrate as inner/outer diameter in microns. Brightfield microscope inset of sputtered nickel dock with 30/90 μm dimensions (lower right).

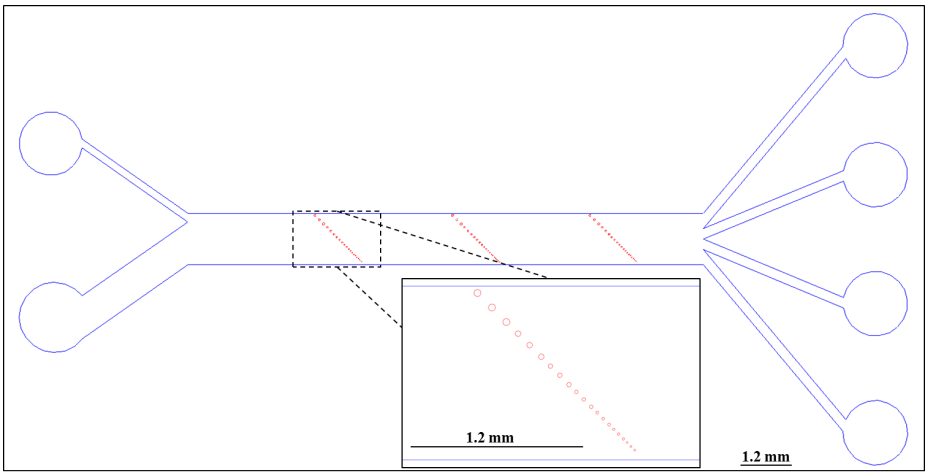

Figure 4.2: AutoCAD design of masks for microfluidic channel (blue outline) and magnetic micro-docks (red circles). The narrow inlet (upper left inlet) concentrates particles along the top of the channel. The micro-docks are arranged to allow spinning micro-robots to hand off captured particles, moving them through the buffer flow (lower left inlet) and toward successively lower outlets (right).

Bonding was performed using 24 seconds of oxygen plasma (International Plasma Corporation, IPC Barrel Etcher) with a forward power of 50 W and 1 Torr O_2. After carefully bringing the PDMS channels into contact with the glass substrates, the bonded devices were heated to 75°C for 2 minutes to strengthen the bond.

Channels were secured in a removable, non-magnetic clamping sandwich that fit snugly into the central workspace of the electromagnetic-coil system on the microscope stage. A 20x objective was used for all flow experiments. Samples were introduced through polyether etherketone (PEEK) tubing inserted into the inlets and outlets of the channel, and flow rates were controlled with two separate syringe pumps (KDS Legato 180, BS-8000 DUAL, Braintree Scientific). Separate pumps allowed us to control the ratio of inlet flow rates and adjust the location of the interface between the micro-robots and buffer streams (see Fig. 4.3).

4.3.4 Magnetic Micro-Robots with Non-Spherical Shapes

Complex 3D structures can be fabricated via the two photon polymerization (TPP) technique at very small scales. TPP is an extension of traditional photolithography, which uses light to selectively excite a photosensitive resist and initiate polymerization [105, 106, 107, 108, 109]. The unusual and defining feature of two photon absorption is the non-linear nature of initiator activation. Rather than polymerization occurring in a linear fashion with increasing power, no polymerization takes place until a critical threshold is exceeded. When a laser is tightly focused into a diffraction-limited spot within a volume of photoresist, photon density exceeds the activation threshold only in that focal region, restricting polymerization to a small

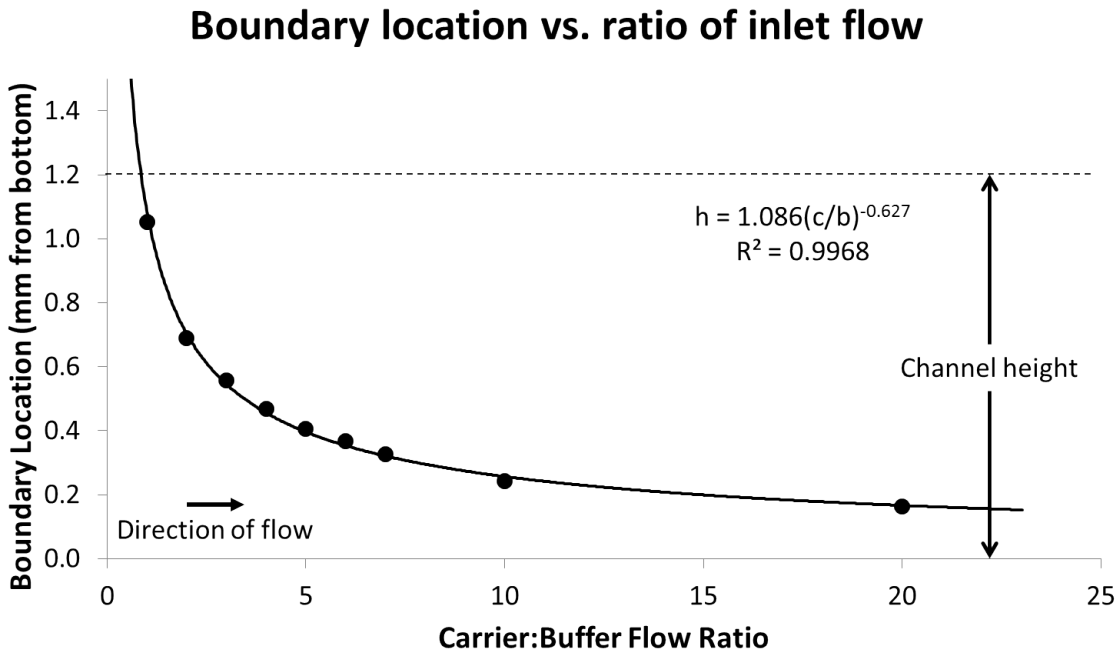

Figure 4.3: The narrow inlet was designated the "top" of the channel, with the wide, buffer inlet at the "bottom". A power fit shows good agreement with the experimental data, allowing us to predict the inlet flows needed to locate the interface at any given dock on the substrate.

volume typically referred to as a "voxel" [110], without causing partial polymerization in areas just outside the focal region. The voxel can be likened to a three dimensional pixel, which can then be scanned through the photoresist to polymerize structures with resolutions below the diffraction limits normally imposed by one photon lithography [106]. Figure 4.4 shows the typical size and shape of a TPP voxel, and Fig. 4.5 shows a schematic and resultant structures of TPP printing.

Magnetic Nanoparticle Composite Resist

To fabricate magnetically responsive micro-robots using TPP, magnetic nanoparticles were mixed into the photoresist used for TPP. Magnetite nanoparticles (Fe_3O_4) were obtained from Chemicell GmbH in a pre-made ferrofluid suspension. Particles were coated in a block copolymer dispersant and suspended in γ-butyrolactone. Nanoparticles were added to IP-G resist (Nanoscribe) to make 6x1 mL samples in a range of concentrations (0%, 0.1%, 0.5%, 1%, 2%, and 4% by volume). Compositions were calculated using eqn. (4.1) with constants from Table 4.1.

$$\frac{\text{mL MNP}}{\text{mL Total}} = \frac{Desired\%}{100} \cdot \frac{\text{1 mL stock}}{\text{125 mg MNP}} \cdot \frac{\text{1000 mg}}{\text{g}} \cdot \frac{\text{1 g}}{\text{5.2} \times 10^{14}\ \text{MNP}} \cdot \frac{\text{1 MNP}}{\text{1.8} \times 10^{-15}\ \text{cm}^3} \cdot \frac{\text{1 cm}^3}{\text{1 mL}}. \tag{4.1}$$

Mixtures were created by adding the appropriate volume of stock ferrofluid to photoresist for 1 mL total volume. The composite was mixed for 15 minutes with a handheld sonication probe (power/frequency here), pulsed at an on/off rate of 10% to prevent heat buildup. Samples were stored at 2–8°C until use. Visual observation

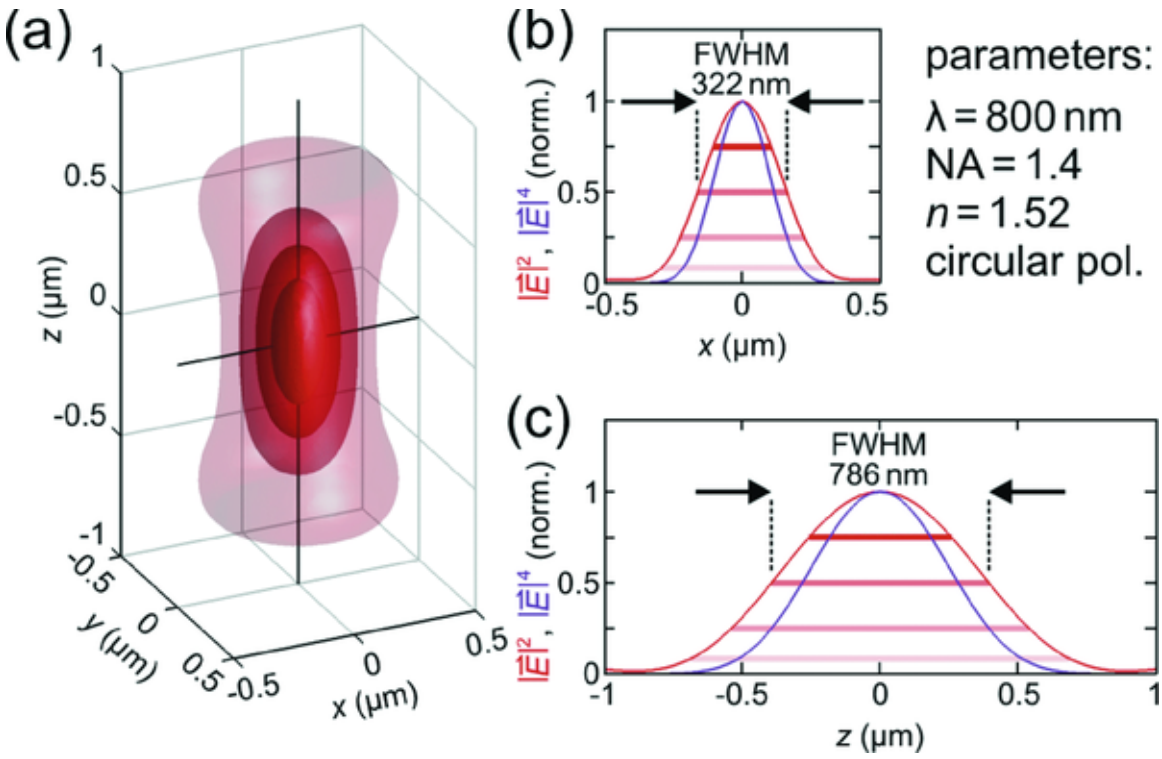

Figure 4.4: Calculated focal intensity distribution of a typical writing spot. (a) Iso-intensity surfaces. The profiles along the two black lines are depicted in b) and c). (b) Lateral profiles of $|\overrightarrow{E}|^2$ (red) and $|\overrightarrow{E}|^4$ (purple) correspond to one-photon exposure and two-photon exposure, respectively. (c) Axial profiles of $|\overrightarrow{E}|^2$ (red) and $|\overrightarrow{E}|^4$ (purple). The horizontal lines in b) and c) correspond to the iso-intensity values of the surfaces in (a). Figure and caption reprinted from [110].

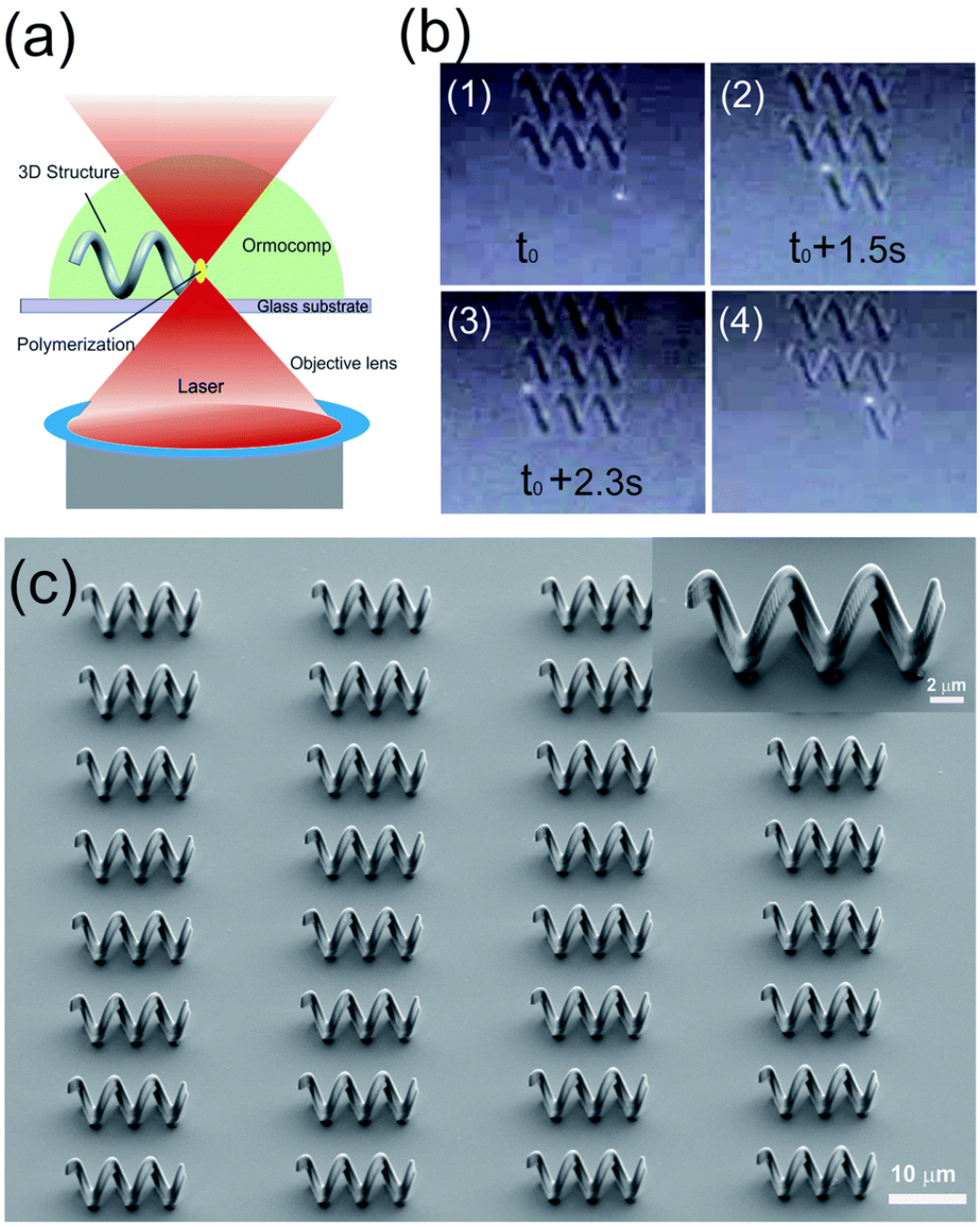

Figure 4.5: Schematic of TPP operation using $ORMOCOMP$ photoresist to fabricate helical microstructures. Figures reprinted from [111].

Table 4.1: Material properties of magnetite nanoparticles used to create composite resists for two photon polymerization. Adapted from materials specifications sheet from Chemicell.

Material Property (Fe_3O_4 MNPs)	Value	Units
Particle size (metallic core)	110-130	nm
Particle size (hydrodynamic)	150	nm
Concentration	125	mg/mL
Particle number	$5.2x10^{14}$	g^{-1}
Ferrorfluid density	1.25	g/cm^3

indicated that the composites remained in stable suspension for over 25 days, but for consistency the suspensions were always resonicated for 2 minutes immediately prior to use.

3D Printing of MNP-Composite Resist

Samples of each composite mixture were drop-cast onto TPP glass substrates (20 μL, 1 cm droplet diam.) and baked on a hotplate. IP-G samples were baked at 100°C for 1.5 hours (ramp rate 20°C/min) to drive out excess solvent and gel the PMMA component ($\sim$3 vol.%). PMMA gelation provides physical support for printed structures that are not attached to the substrate, or have large horizontal overhangs. Without this gelation step, loose structures would drift through the resist during printing, pushed by the momentum imparted on them by absorbed photons near the focal point of the laser. The same effect is utilized in optical tweezers, but in this case creates

undesirable results.

Table 4.2: Laser properties of the Toptica NIR FemtoFiber Pro Erbium fiber laser used for two photon polymerization.

Laser Property	Value	Units
Calibration Power (100%)	50	mW
Wavelength	780	nm
Pulse Duration	80-100	fs
Pulse Frequency	80	MHz
Energy per pulse	0.625	nJ
Photons per pulse	2.45	billion

A Photonic Professional GT (Nanoscribe GmbH) with a FemtoFiber Pro NIR laser (Toptica Photonics, Table 4.2) was used for all two-photon polymerization of resists. Printing was performed using a 60x objective (NA = 1.4) in oil immersion mode. After TPP, IP-G samples were developed in propylene glycol monomethyl ether acetate (PGMEA 99.5%, Sigma-Aldrich) for 15–20 minutes to remove undeveloped resist. Samples were then submerged in 2-propanol to rinse away the PGMEA. Samples intended for SEM imaging were then dried with gentle N_2, while samples intended for magnetic field experiments were maintained in propanol until use. Storage in propanol helps to prevent stiction between the mobile and stationary components of the printed features, which is caused by the surface tension between microstructures during drying. Critical point drying with supercritical CO_2 can also be used to limit stiction from electrostatic forces, hydrogen bonding, and Van der

Waals forces.

4.4 Modeling

4.4.1 Lateral Migration of Micro-Particles Between Local Streamlines

When a particle is exposed in an unidirectional shear flow, two kinds of forces could possibly occur on the object surfaces. The first force is parallel to the direction of the local flow, which is the drag force that acts to accelerate the particle inside the flow until it is force-free in the same direction. The other force is perpendicular to the direction of the flow, which is usually termed as the "lift force". This lift force would cause lateral migration of the particle between streamlines. However, such lift force is not always existent. In fact, theoretical study has shown that under Stokes flow condition where inertia effects are completely negligible, no lateral force would exist in any unidirectional flow due to the linearity of the system [112]. Therefore, inertia effects are necessary for inducing lateral migration of particles between streamlines in shear flows.

Plenty of studies have been carried out on the lateral migration of particles inside confined environments such as microfluidic channels. In such a case, the inertial lift force experienced by a particle arises from two sources: wall effect and the interaction between the particle and the shear gradient of the flow. The former always acts to push the particle away from the wall, while the direction of the latter is more complicated.Two effects can contribute to this part of the lift force. The first effect arises

from any simple shear component of the flow velocity and follows the observation by Saffman [73] that if the the particle lags behind the local undisturbed flow, such force acts to push to the particle up the shear gradient and $vice - versa$. The second effect is due to the curvature of the velocity profile and exists only when there is a gradient of shear [113]. Therefore, the lift force finally experienced by the particle would be the total balance between these three effects. Figure 4.6 shows how these three effects affect the lateral migration of a particle in the presence of a 2D quadratic flow near a wall. In a simple shear flow, the lift force arises due to the Saffman effect can be calculated by eqn. (2.11). In the presence of a nearby wall, such lift force in a linear shear flow is modified to be: [70]

$$F_{l(wall)} = \rho_{fl} a^2 \left(u_c - v_{obj}\right)^2 G(a/\epsilon, a\gamma/\left(u_c - v_{obj}\right)), \tag{4.2}$$

where a is the radius of the particle, ρ_{fl} is the density of the fluid, u_c is the flow velocity at the position of particle's center, v_{obj} is the velocity of the particle, ϵ is the gap between the particle and the wall, γ is the shear rate, and G is a function of a, ϵ and the velocity difference.

For a neutrally buoyant particle that moves freely with the background flow, Saffman effect would not contribute to the overall lateral force [114]. However, the lateral force would still exist if the velocity gradient inside the flow is not constant. The total lift force of a neutrally buoyant particle immersed in a 2D Poiseuille flow in a straight channel has been found as [115]:

$$F_{l(Poiseuille)} = \frac{6a^4 \rho_{fl} {U_{cf}}^2}{\pi W_{ch}^2} f(\epsilon/W_{ch}), \tag{4.3}$$

where U_{cf} is the maximum flow velocity inside the channel, W_{ch} is the width of

the channel, and $f(\epsilon/W_{ch})$ is a factor associated only with particle's lateral position inside the channel. Such a force is hard to observe when Re is very small.

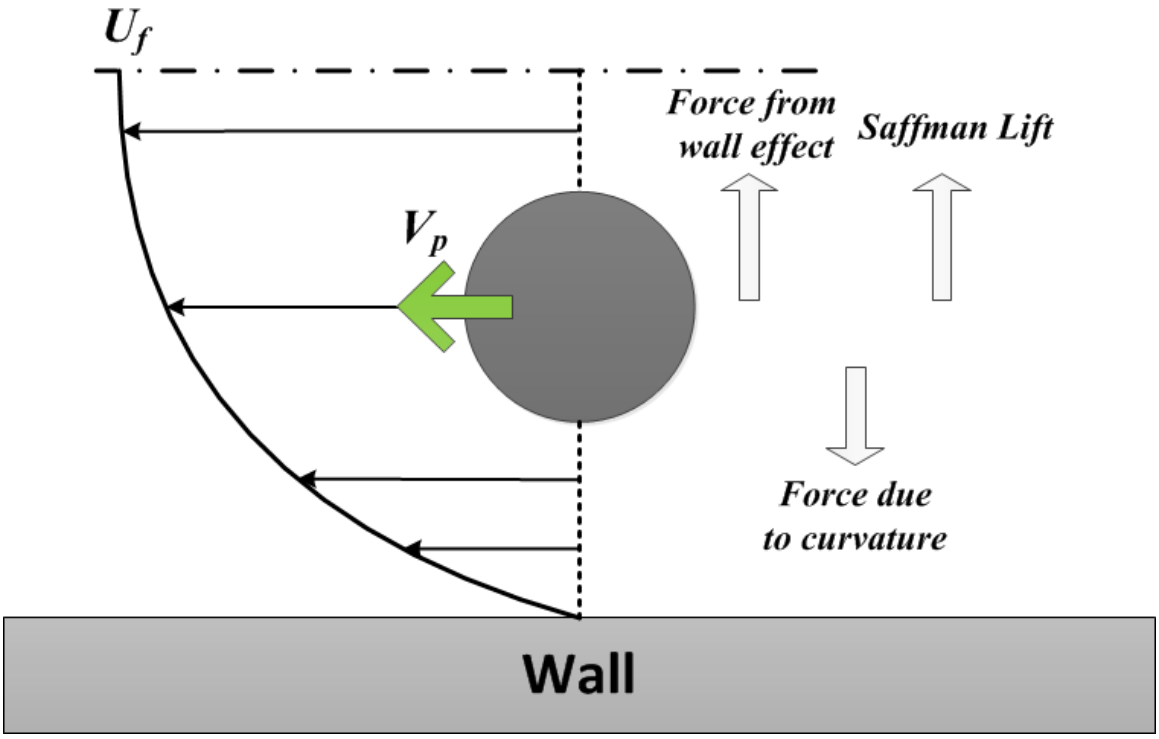

Figure 4.6: Top-view of a spherical object exposed to a 2D quadratic flow near a wall. Three different inertia effects contribute to the lift force experienced by the object in lateral direction.

When the micro-robot spins inside a microfluidic channel in the presence of background flow, it still generates a local rotational flow field around it as seen in Sec. 2.4.2 and 2.4.3. The disturbed flow region can be treated as the linear superposition of the background flow and the induced rotational flow due to the linearity of

the system at very small Re. The inertial lift force on particles still exists inside the disturbed flow region, but could be significantly different than anywhere else inside the channel due to the local rotational flow. The presence of the induced rotational field could generate a large shear gradient inside the flow region, which could significantly amplify the inertial effects, and hence the lift force. In addition, if the micro-robot is placed close to the wall, it also concentrates the streamlines in the gap between it and the wall. Therefore, particles could migrate to another streamline inside the gap much more easily. Such migration would be more observable when the particles leave the disturbed flow region, as the flow cross-section is widen and resumes to normal. When the particles are traveling inside the rotational flow region, they also experienced a centrifugal force due to angular acceleration as they tend to orbit around the rotating robot. Such force acts to push the particles away from the rotating robot. Therefore, the net lateral force the particles experience inside the rotational flow region would be the combination of all previously introduced inertial lift effects plus the centrifugal force. The final migration of particles is determined by this net lateral force.

4.4.2 Rotational Flows Induced by Spinning Spherical Micro-Robots inside Microfluidic Channel

Numerical simulations were carried out to understand the flow pattern inside a microfluidic channel in the presence of a spinning spherical micro-robot. The commercial finite-element software *COMSOL Multiphysics* 4.3 with the laminar flow interface was used for the simulations. The microfluidic channel was modeled as

a rectilinear block with dimensions of 1000 µm (length)× 100µm (width)× 60 µm (height) with three spheres each of a diameter of 20 µm located a the center of its length. Figure 4.7 shows the established model. An average flow velocity of 100 µm was specified on one end of the block as inlet, while the other end was specified as outlet with zero normal stress. Modeling of rotation of the spheres was achieved by respectively specifying the linear velocities on the surfaces of the three spheres according to the desired rotation speed of 15 Hz in clockwise direction from top-view of the channel. A total of 366,957 tetrahedral elements were used in the simulations.

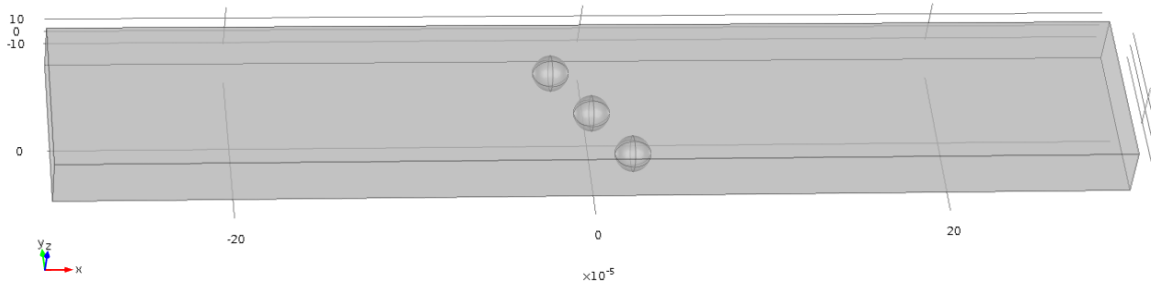

Figure 4.7: The microfluidic channel was modeled as a rectilinear block with dimensions of 1000 μm (length)× 100 μm (width)× 60 µm (height) with three spheres each of a diameter of 20 µm located a the center of its length.

The first set of simulations was to study the influence of gap distance between the sidewall and the nearest robot on the flow pattern. The streamlines of the flow inside the channel for different gap sizes on the equatorial plane of the spheres ($z = 10$ µm) are shown in Fig. 4.8. It is observed that as the gap size increases, the portion of flow that is compressed through the gap increases as well. When the gap is too

small, vortices could form in front of the gap, which is undesirable for the purpose of sorting. To further examine the flow velocity profile at the gap, we plot the velocities in the gap as functions of the width of the channel on $z = 10\,\mu\text{m}$ in Fig. 4.9. The velocity profiles indicate that a narrower gap would result in a larger shear gradient at the gap, which could lead to a more significant lateral force for particle migration as the force is correlated with shear strength. Therefore, there exists an optimal range of gap size for the purpose of sorting. Such range is expected to be around 0.7–1.1 radius of the spherical micro-robot according to the simulation results.

The second set of simulations was to study the influence of separation between robots on the flow pattern. The streamlines of the flow inside the channel for different gap sizes on the equatorial plane of the spheres ($z = 10\,\mu\text{m}$) are shown in Fig. 4.10. As the separation decreases, the overlaps between individual rotational flow induced by each micro-robot increase, which make it easier and easier for micro-particles to be conveyed down the width of the channel with the streamlines once they pass the gap between the first robot and the top wall and get trapped by the rotational flow induced by the first robot. However, since the micro-robots are magnetic, they would snap into each other if the separation is too small. From experimental observation, the minimum separation that could still prevent attraction between robots is about $4\,R$ for the spherical micro-robots used in this work. A separation of $4.5\,R$ or above should be used to achieve stable, separate rotation of each micro-robot inside the channel.

It should be noted that although the above results were obtained for spherical micro-robots, they provide useful insights to predict the flows induced by robots

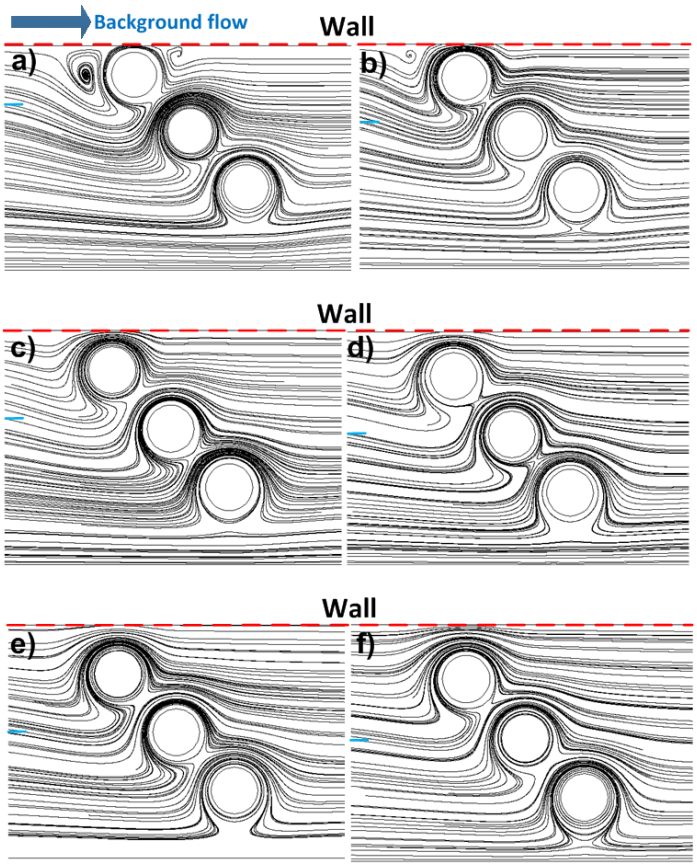

Figure 4.8: Top-view of flow streamlines inside the channel in the presence of rotating micro-robots with varying gap size to the wall. Streamlines were taken on the equatorial plane of the spheres at $z = 10\,\mu$m. Background flows entered the channel from the left of the view. a) Gap size = 0.3 radius of sphere (R). b) Gap size = 0.5 R. c) Gap size = 0.7 R. d) Gap size = 0.9 R. e) Gap size = 1.1 R. f) Gap size = 1.3 R. The short blue solid dash indicates how much flow is compressed through the gap.

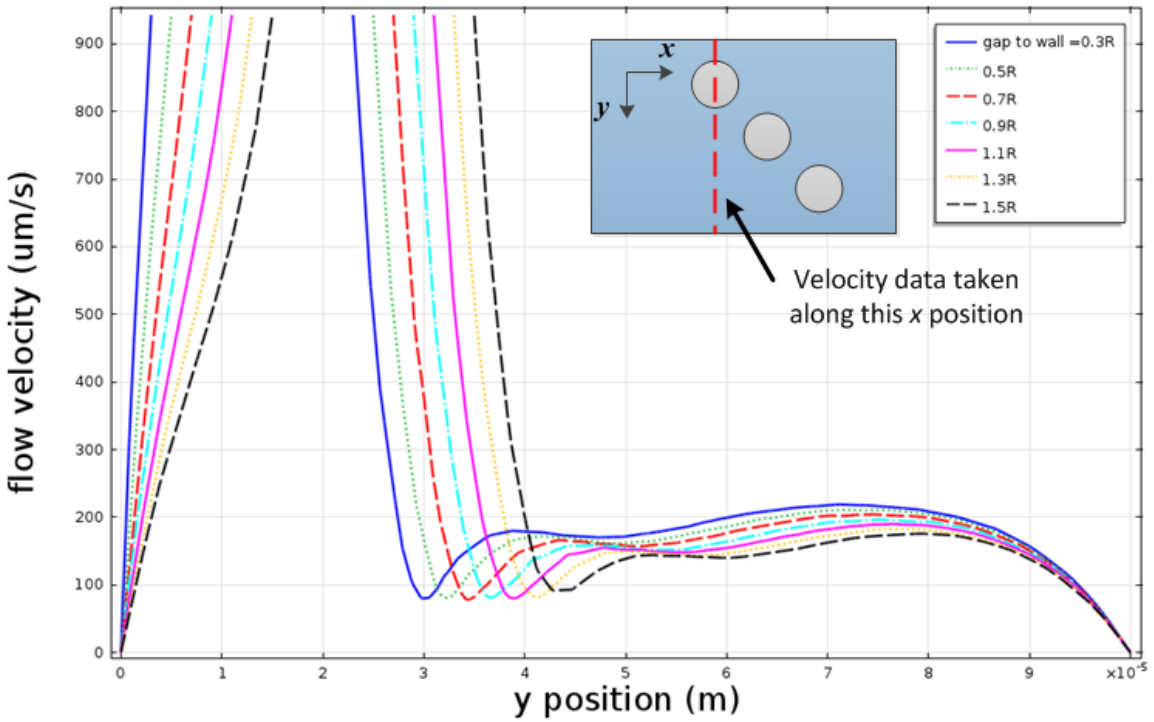

Figure 4.9: Velocity profile of flow in the gap along width of the channel at different gap sizes. The inset is a top view of the channel with three spherical robots inside showing at which x-position the velocity data were taken. The velocity data were taken on the equatorial plane of the spheres at $z = 10\,\mu\text{m}$. The robot occupies a length of $20\,\mu\text{m}$, locating at where each velocity profile breaks.

with other rotationally-symmetric shapes, similar to the discussion in Chapter 2.

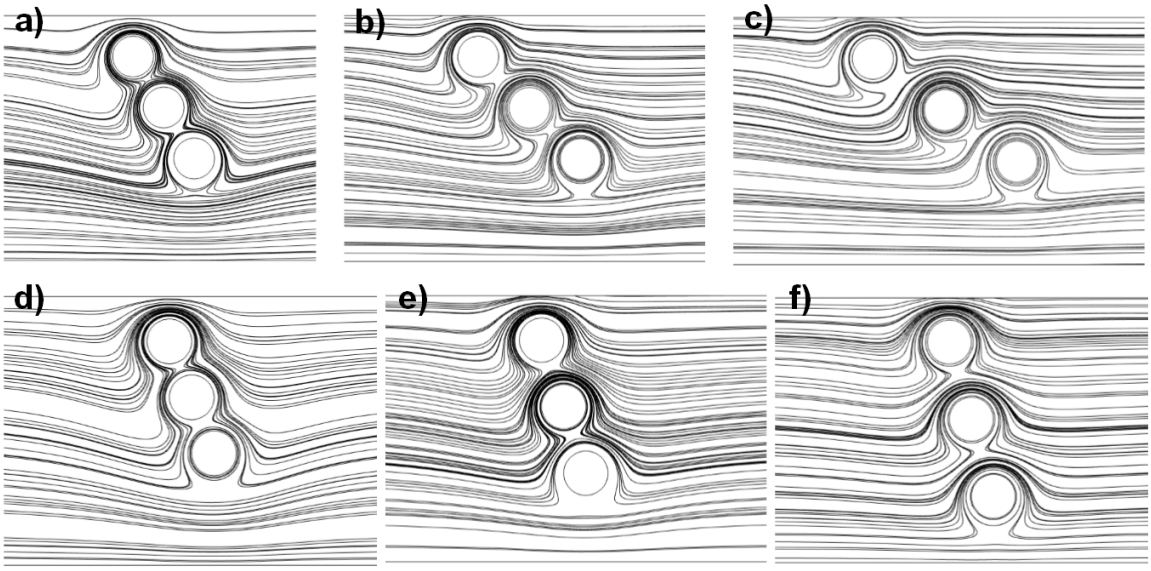

Figure 4.10: Top-view of flow streamlines inside the channel in the presence of rotating micro-robots with varying separation between robots. Streamlines were taken on the equatorial plane of the spheres at $z = 10\,\mu\text{m}$. Background flows entered the channel from the left of the view. For a)–c), the vertical separation was fixed at 2.5 R while horizontal separation varied from 1.5 R for a), 2 R for b) to 2.5 R for c). For d)–f), the horizontal separation was fixed at 1 R while vertical separation varied from 2.5 R for d), 3 R for e) to 3.5 R for f).

4.4.3 Magnetic Docking

Magnetic micro-docks were made of Nickel, which is a soft magnetic material. Such soft magnetic material could only be magnetized when exposed to an external magnetic field, applied by a nearby magnetic micro-robot or by the electromagnetic-coil system in this case. To examine whether or not such magnetic docks are capable of holding the magnetic micro-robots in place under a strong background flow when global magnetic field is applied by the coils, numerical simulations were carried out using the same finite-element package *COMSOL Multiphysics* 4.3 with the AC/DC module. The micro-robot was modeled as a 30 μm-in-diameter sphere placed on top of a dock with an outer diameter of 30 μm and a thickness of 500 nm. Two types of dock shape were examined: disk-shaped and donut-shape with an inner diameter of 10 μm. Figure 4.11 shows the established model. A downward magnetic field (B_z) was applied in the whole space filled with non-magnetic material, while the magnetization of micro-robot was specified on in negative z-direction as the magnetic micro-robot would always tend to align its magnetization with the external field. The material property of relative magnetic permeability of both the Nickel dock and the NdFeB micro-robot was also specified. A total of 1,881,243 tetrahedral elements were used in the simulations.

In the first set of simulations, influence on the interactive force on the micro-robot applied by the micro-dock in z-direction (F_z) of three different parameters were examined: Field strength of B_z, relative permeability of the docking material, and the strength of magnetization of the micro-robot. The results are plotted in Fig. 4.12. It is observed that the in general, disk-shaped dock can provide stronger holding force

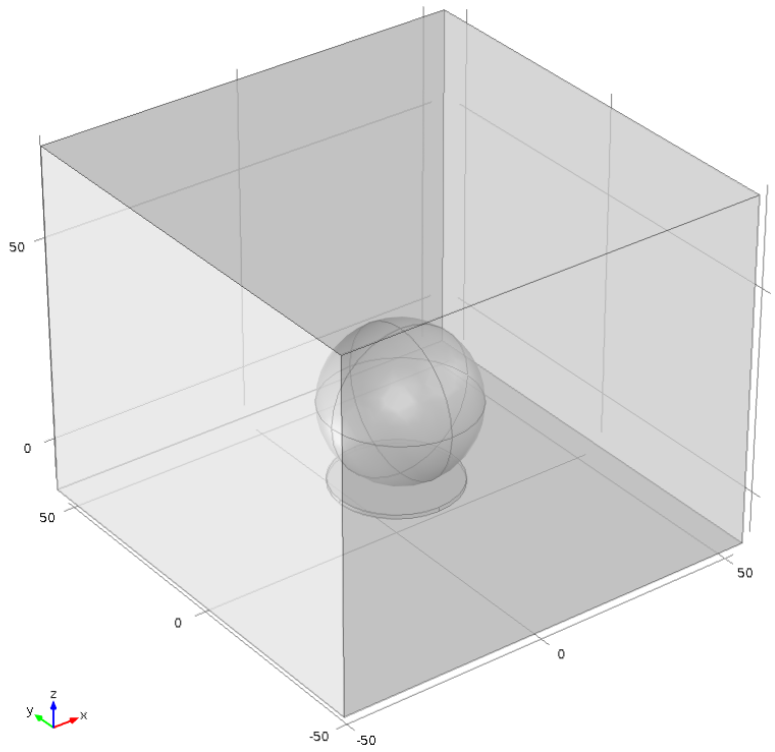

Figure 4.11: The micro-robot was modeled as a 30 µm-in-diameter sphere placed on top of a dock with an outer diameter of 30 µm and a thickness of 500 nm.

F_z than donut-shaped dock, because the former has more substances in the same volume. Another general observation is that all the three parameters have positive effect on F_z. While F_z increases linearly with B_z, it first increases rapidly with an increasing relative permeability, and then approaches saturation after a value of 1000. The magnetization of the micro-robot has a much stronger effect on F_z than the other two parameters.

In the second set of simulations, we examined how the lateral misalignment between the robot and the dock would affect F_z and the lateral interactive force - the centric force (F_{ct}). In these simulations, all the parameters were kept constant except for the lateral position of the micro-robot on the dock. The results are plotted in Fig. 4.13. Unlike in the zero-misalignment case where F_z remains attractive, F_z shift between attractive and repulsive in the non-zero misalignment case. The attractive F_z peaks at a relative misalignment of around $0.6\,R$, and then drops till it becomes repulsive as misalignment increases for both disk-shaped and donut-shaped dock. For the centric force F_{ct}, it remains repulsive when the relative misalignment is smaller than $0.6\,R$, and shifts to attractive as misalignment goes above $0.6\,R$. These results indicate that there could be two possible positions for the micro-robot to stay on the dock in steady state, one is at the center of the dock where the holding force F_z is at its maximum, and the other is at a distance of about $0.6\,R$ from the dock center. However, the robot cannot stay stably on the first position as any small perturbation would results in a radial force that pushes the robot away from this position.

Now it is possible to compare the drag force experienced by a spherical micro-robot under a strong background flow. Under the Stokes drag assumption, the drag

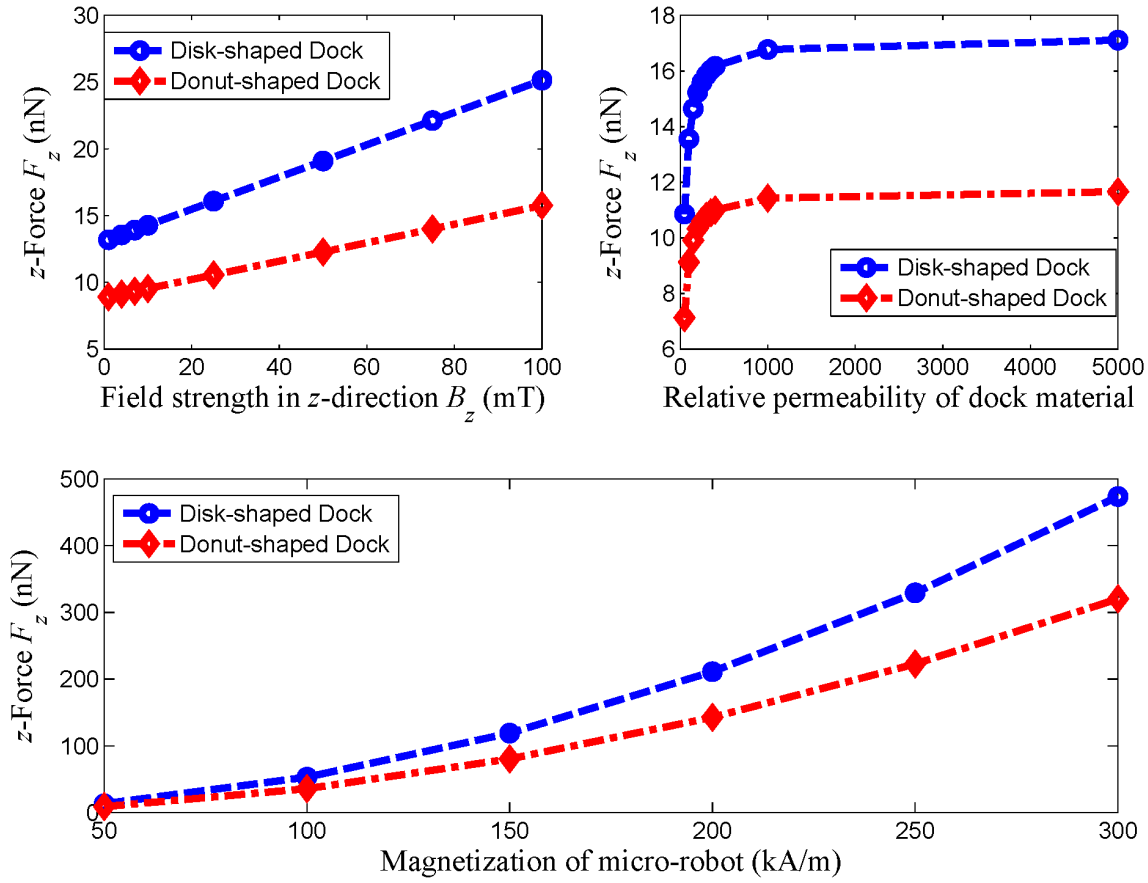

Figure 4.12: a) B_z varied while magnetization of the micro-robot and the relative permeability of dock were kept constant at 50 kA/m and 100, respectively. b) The relative permeability of dock varied while B_z and magnetization of the micro-robot were kept constant at 4 mT and 50 kA/m, respectively. c) Magnetization of the micro-robot varied while B_z and relative permeability of the dock were kept constant at 4 mT and 100, respectively.

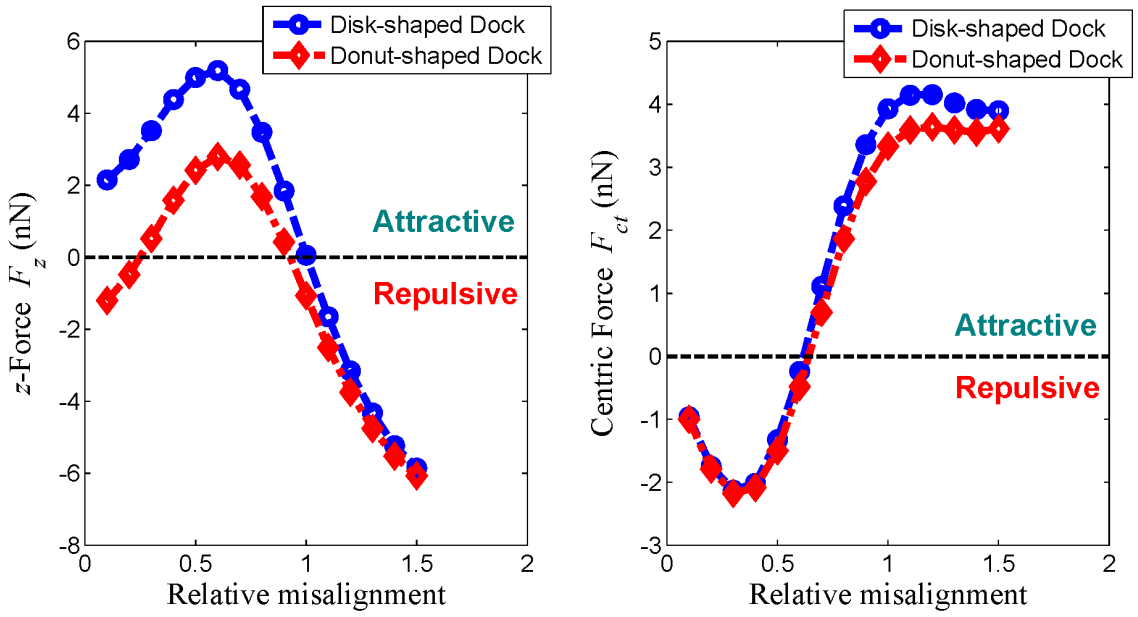

Figure 4.13: B_z, relative permeability of the dock and magnetization of the micro-robot were kept constant at 4 mT, 100 and 50 kA/m, respectively. Lateral misalignments were normalized by radius of the robot. a) Influence on the interactive force in z-direction (F_z) b) Influence on the interactive force in radial direction (F_{ct}).

force experienced by a sphere in a unidirectional flow can be calculated by:

$$F_{drag(stokes)} = 6\pi\rho_{fl}\nu R\left(u_c - v_{obj}\right). \tag{4.4}$$

For a fixed 30 μm spherical robot under a very strong flow of 1 mm/s flow rate in water, the drag force is estimated by eqn. (4.4) to be approximately 0.3 nN, which is less than 0.05 of F_z on a weakly magnetized micro-robot placed at the center of the dock. Therefore, such a robot can stay at the center of the dock as long as the friction coefficient between the robot and the dock is greater than 0.05. In real experiments, the flow rate would not reach the value of 1 mm/s, and hence the Nickel docking should be functional. Increasing the magnetization of micro-robot would be the most practical way to secure the functionality of the Nickel docking.

4.5 Experimental Results and Discussion

4.5.1 Magnetic Docking Substrates

Docking substrates were well formed and consistent in thickness when patterned with RF sputtering. One hour of sputtering time yielded film thicknesses of 490–500 nm, and approached the limitations of lift-off resist patterning with nickel. Longer times often resulted in film cracking or delamination due to internal stress.

Magnetic micro-robots could be successfully localized to individual docks by rolling them along the substrate using rotational fields parallel to the substrate. Once positioned, the micro-robots exhibited a natural tendency toward the dock. The downward force applied by the dock on the particle (holding force) could be in-

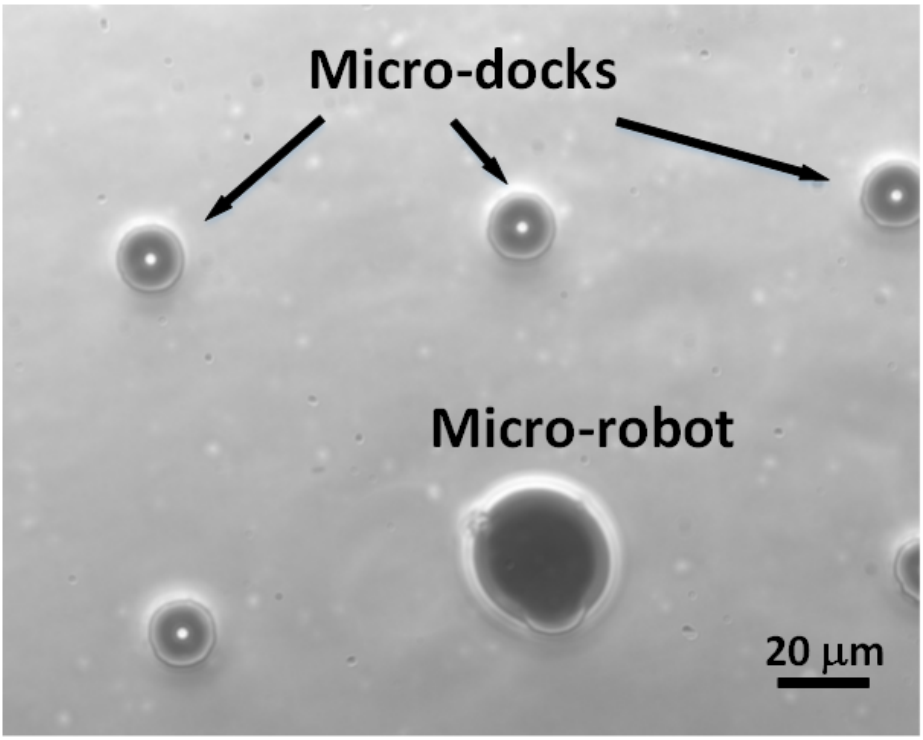

Figure 4.14: A spherical micro-robot was placed on the substrate and attracted onto a magnetic micro-dock.

creased using a magnetic field applied perpendicular to the substrate. Stable rotational speeds of ≥ 40 Hz could be obtained in static liquid environments using field strengths of only 1 mT. Higher speeds are likely possible, but could not be visually confirmed due to the frame rate of the camera used. Under fluid flow, higher vertical fields were required to keep the micro-robots on the docks. Increased downward force, and therefore surface friction, reduced the maximum rotation to ~ 20 Hz with 1.5–3.0 mT rotational field strength.

Stable docking appeared to be more dependent on the structure and magnetization of individual micro-robots placed on the docks, with some robots performing well on all dock sizes and shapes, while others exhibited poor attraction and spinning, even when magnetized in the same field. Microstructural differences are likely responsible for the inconsistent magnetization of the spinners.

4.5.2 3D-Printed Micro-Robots

Characterization of TPP printing parameters was performed using line tests, with details given in Append. D. A variety of magnetic IP-G composite structures were then fabricated using TPP. Printed structures were well-formed and structurally sound in resist composites up to 1 vol% (Fig. 4.15). At concentrations of 2 and 4 vol%, the viable range of printing parameters narrowed considerably, resolution dropped, and layer-to-layer as well as structure-to-glass adhesion was substantially reduced.

Rotation of 1% structures in applied fields up to 8 mT were limited to ~ 1 Hz, with no rotation observed for 0.5% and 0.1% composites. Stiction occurred in the majority of 3D prints, even when post-development drying was avoided, requiring

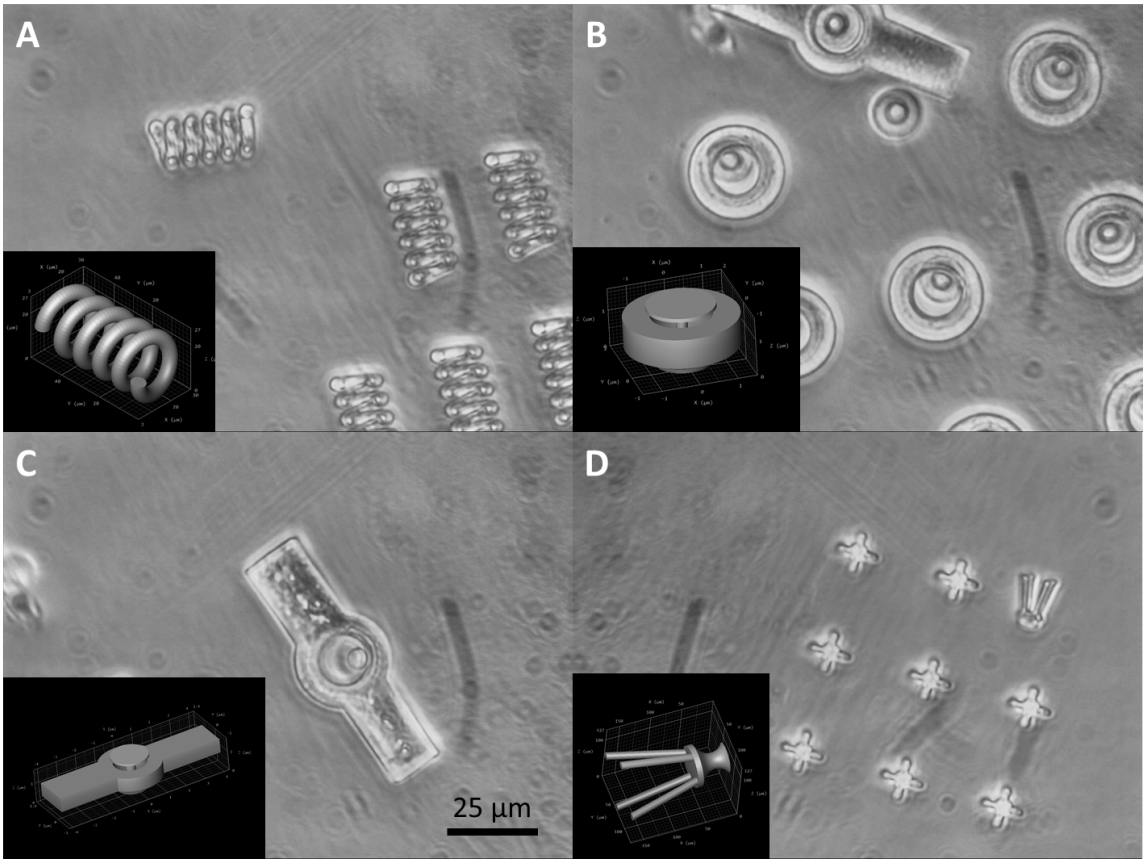

Figure 4.15: Bright-field microscopy of 3D-printed micro-robots in water. Various structures were designed: (A) corkscrew, (B) spinning disk, (C) spinning bar, and (D) flagella/sputnik. Structures were printed in IP-G resist with 1 vol% Fe_3O_4 MNP's. Structures were well formed but could only spin at $\leq$1 Hz. Structures with 2% MNP's were poorly formed and failed to adhere properly to the substrate.

physical detachment by force applied with a glass needle micro-manipulator. These problems made it impossible to use 3D printing as the fabrication method for making magnetic micro-robots for applications inside microfluidic channels in the current work.

4.5.3 Size-Dependent Lateral Migration of Micro-Particles inside Microfluidic Channel

One spherical micro-robot was placed on the topmost nickel dock within the microfluidic channel, and polystyrene beads of 5 μm, 10 μm and 20 μm were injected through the top inlet in separate experiment runs. Buffer flow through the bottom inlet was adjusted to locate the interface of the two inlet flows just above the midpoint of the micro-robot, ensuring that most particles passed between the micro-robot and the channel wall when no magnetic field was applied. After establishing stable flow, a rotational field was applied and the rotational flow around the micro-robot was induced. The polystyrene beads passing through the disturbed flow region displayed different responses to the induced rotational flow based on their sizes and left the flow region with distinguishable differences on their displacements along the width direction of the channel from the their original trajectories. Results from analysis of videos taken from experiments are summarized in Fig. 4.16 to show the size-dependence of vertical displacement Δy of particles before entering and after leaving the region significantly disturbed by induced rotational flow. Both 5 μm and 10 μm polystyrene beads exhibited positive Δy's which means that they were pulled away from the channel sidewall in the rotational flow region, while the 20 μm beads

exhibited a negative Δy, which means they were pushed closer to the sidewall. The results presented here were derived from one successful set of experiments with the same micro-robot and channel. Many factors could affect the quality of experiment, such as the properties of micro-robots and fabrication quality of the channels with Nickel docks. However, the results were able to demonstrate that the size-dependent lateral displacement of particle enlarged by induced rotational flows could potentially enable separation of particles with different sizes in continuous flow.

We also preliminarily showed diverting particles with different sizes in a single mixture into different paths, with details given in Append. E. Real sorting of micro-particles with various sizes will be a future work.

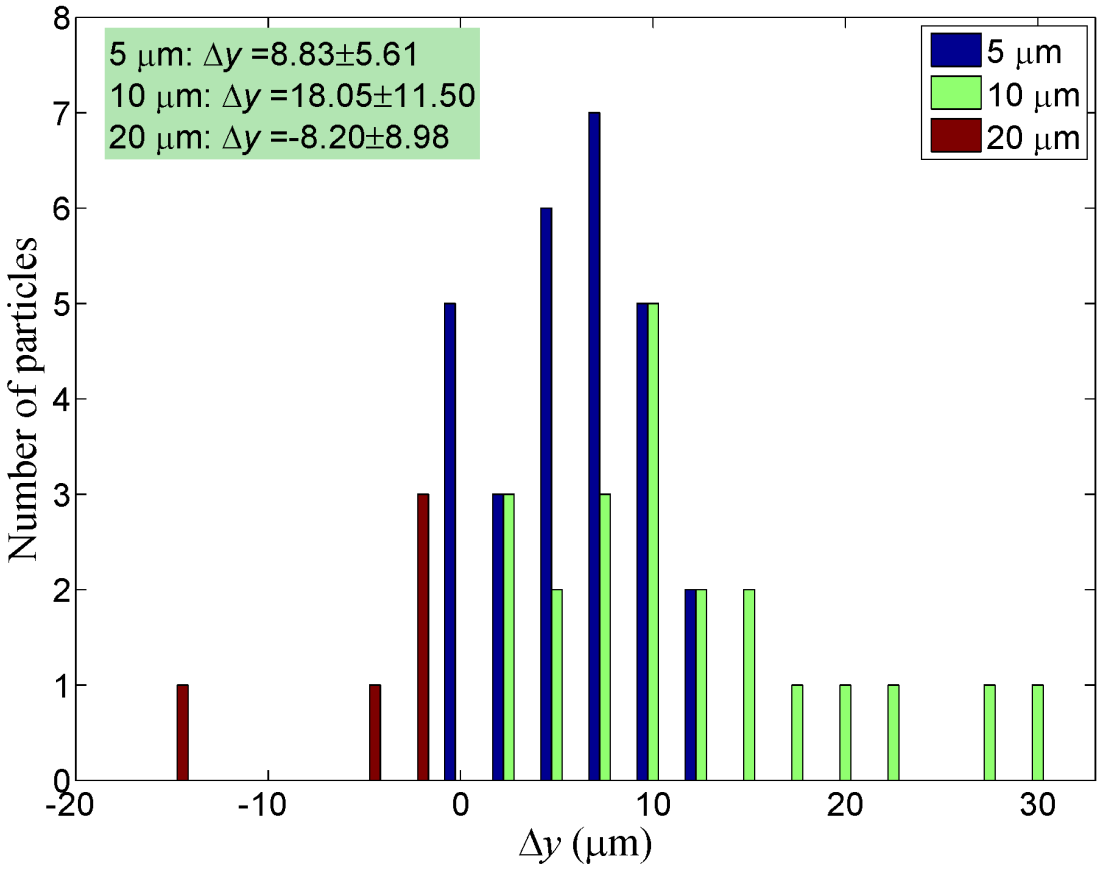

Figure 4.16: Size-dependent vertical migration of particles in induced rotational flow. Flow rate is 4.5 μL/min, field strength = 1.5 mT, rotation frequency = 15 Hz. Magnetic microsphere size was 56 μm in diameter.

4.6 Chapter Summary

In this chapter, we incorporated the rotating magnetic micro-robot system with microfluidic channels to generate rotational flows in the presence of continuous background flows. Magnetic docking substrate was fabricated and utilized to dock the mobile spherical micro-robots while they were spinning to generate rotational flows. The flow patterns inside the system were analyzed with numerical simulations, and the lateral migration of micro-particles was discussed based on physical model established. The induced rotational flows were demonstrated to be capable of diverting micro-particles to separate paths inside the microfluidic channel based on their sizes, which could enable size-based sorting of micro-objects in continuous flows. This approach was effective, but will be difficult to scale up, as each additional micro-robot that must be docked adds setup time and complexity to the system.

TPP method was also proposed to fabricate micro-robots with MNP-composite photoresist. This method could not only allow fabrication of micro-robots with complex 3D shapes, but it would also facilitate integration of a large number of robots into microfluidic channels and enable stable spinning and precise position control the these robots inside the channels. However, it was ultimately proved insufficient due to our specific needs and the physical limitations of the materials.

Chapter 5

Summary and Future Work

This thesis investigated the rotational motion of magnetic micro-robots inside viscous fluids. It was demonstrated that such rotational motion would locally induced rotational flows in the vicinity of robots, and the surrounding liquid in return would apply forces and torques on the rotating robots. Analysis was performed on the properties of the induced rotational flows as well as the interactions between the rotating robot with its environment at low Reynolds number regime. Three applications were proposed and implemented using rotating magnetic micro-robots in both quiescent liquid and continuous flow.

For the first application in quiescent liquid, a versatile two-dimensional non-contact manipulation method was developed using the rotational flow induced by robot motion at low Reynolds number regime. Controllable rotation of a spherical micro-robot on a substrate was successfully achieved to simultaneously achieve translation of robot on the substrate and local generation of rotational flow around

the robot that could trap objects present in the flow region. Versatility and scalability of the manipulation method using a single rotating micro-robot was demonstrated by performing manipulation at both sub-millimeter and micron- scales using the method for various micro-objects, including biological samples such as human blood cells and flagellated bacteria. Automated manipulation based on the developed method was also implemented with the assistance of visual feedback. In addition, parallel manipulation of multiple objects using rotational flows generated by a team of micro-robots was also implemented on a specially prepared substrate embedded with magnetic micro-docks.

The second application was also implemented in quiescent liquid based on the hydrodynamic interactions between rotating flexible slender bodies and the surrounding liquid to achieve three-dimensional locomotion of magnetic micro-robots. A micro-robot design equipped with multiple artificial flexible flagella was proposed and fabricated. Such micro-robot was experimentally demonstrated to be capable of 3D locomotion, and benefited from the improved propulsion provided by multiple flagella.

In continuous flow, it was demonstrated that the rotational flows induced by magnetic micro-robots were able to create size-dependent lateral migration of micro-objects between local streamlines. Such effect was adopted to implement size-based separation of micro-particles under continuous flow. A downsized version of the magnetic docking substrate was used to incorporate the mobile micro-robot system with microfluidic channels. Micro-robots with complex 3D structures were fabricated using two-photon-polymerization technique from a MNP-composite photore-

sist. The fabricated micro-robots were demonstrated to be able to respond to remotely applied magnetic field. However, the responses were proven to be insufficient for applications in microfluidic channel under continuous flow.

During the implementation of this work, new physical phenomenon was found, and novel fabrication methods for magnetic micro-robots were developed. The induced rotational flows were found to be able to trap micro-objects on stable orbits, which phenomenon was not seen before at higher Re and larger scales. Micro-robots with multiple flagella were fabricated via a new yet inexpensive multi-step micro-molding process based on traditional photolithography and manual assembly. Fabrication of magnetic micro-robots with complex structures at micron-scale was achieved by 3D nano-printing method using specially prepared photoresit mixed with MNP's.

5.1 Current Challenges and Potential Applications

5.1.1 Fabrication of Magnetic Micro-Robots at Micron-Scale

Fabrication of magnetic micro-robots with complex 3D structures requires novel fabrication methods that are more more suitable than traditional photolithography and micro-molding techniques to handle structures at micron-scale. TTP is a potential and competitive candidate, but there are problems remaining for using this technique for magnetically strong micro-robots, as seen from this work. An extremely strong magnetic field is required to actuate micro-robots fabricated from MNP-composite photoresist by TTP at high speed due to their weak magnetic properties. Such a

strong magnetic field is not ideal for many biological and biomedical applications. In addition, the need for strong magnetic field increases the complexity of electromagnetic system for generation of such field.

It has been reported that structures fabricated by TTP can be coated with magnetic materials to achieve stronger magnetic properties [111]. However, such approach is not readily applicable for making active magnetic micro-parts, such as micro-spinners, inside microfluidic device. This is because the coating of magnetic materials occurs on the whole substrate, making bonding of microfluidic channels to the substrate difficult.

Therefore, it remains challenging for fabrication of arbitrary 3D micro-structures at micron-scale with strong magnetic properties.

5.1.2 Experimental Characterization of Fluidic Forces on Objects inside Induced Rotational Flow

In this work, we used numerical simulations to study the fluidic forces, such as drag force and radial forces (discussed in Sec. 2.4.4), exerted on spherical objects inside rotational flows induced by rotating micro-robots. Although the method of numerical simulation has been proved valid and widely adopted for fluid mechanics problems [116], the results of numerical simulations will be better supported with experimental observations provided. In the current work, the experimental characterization of the fluidic forces experienced by a spherical objects inside the induced rotational flow was not performed due to the constraints on hardware equipment. However, with improved experimental equipment, it is possible to measure such fluidic forces from

experiments directly.

Characterization of the viscous drag force exerted on a fixed spherical particle inside the rotational flow induced by a rotating micro-robot can be done with the assistance of optical tweezers. Both the particle and the robot need to be held in place near a bottom substrate by two separate laser beams. A magnetic filed will be applied to spin the robot to create the rotational flow around it. The particle held close to the robot will experience two forces in flow direction: the viscous drag force and the optical trapping force. By measuring the displacement of the particle inside the optical trap in the flow direction in steady state, we can correspondingly derive the viscous drag force exerted on the particle.

Directly measuring the radial forces is a much more difficult task not only because such forces are significantly smaller in magnitude than the drag force, but also because that the measurement needs to be done while the particle is actually orbiting the rotating micro-robot. One possible approach to estimate such forces via experiment also requires the use of optical tweezers. The micro-robot needs to be held in place by a laser beam constantly while another laser beam is used to move a particle close to the robot. Once the robot is rotated by an applied magnetic field and the rotational flow created, the laser beam holding the particle should be turned off to let the particle move freely on the substrate. The particle would eventually orbit around the rotating robot with a stable distance. By measuring the distance and the traveling speed of the particle, we can estimate the centripetal force required to hold the particle in orbit, and hence the corresponding radial forces considering that the radial forces exerted on the particle should compensate such centripetal force in steady

state.

5.1.3 Size-Based Sorting of Micro-Particles with Various Sizes

In this work, we demonstrated that the rotational flow induced by rotating micro-robots could cause significant size-dependent lateral migration of particles in continuous flow inside microfluidic channel. We also showed preliminary results of diverting micro-particles with various sizes into different paths. However, systematic analysis of the sorting performance using the proposed method is not yet achieved due to the limited time constraints and the difficulty to control the fabrication quality of the microfluidic channels with Nickel docks embedded. In addition, reliable and consistent sorting results are also an on-going work. We aim to achieve these in the near future. After implementing consistent size-based sorting of micro-particles, the proposed method could be further used for sorting of living cells with different sizes.

5.1.4 3D Non-Contact Manipulation

In this work, non-contact manipulation was only implemented in 2D, where a bottom substrate was required to achieve translation of micro-robots in 2D. On the other hand, 3D locomotion of micro-robots was also demonstrated using rotational motion of micro-robots. Therefore, it could be possible to synthesize the two approaches to achieve non-contact manipulation of micro-objects in 3D. A micro-robot consisting of a body with specially designed geometry and attached flagella maybe able to generate proper rotational flow in 3D by the rotation of its body to trap nearby micro-objects, while using the rotation of flagella to generate propulsion for 3D locomotion.

A possible robot design is shown in Fig. 5.1.

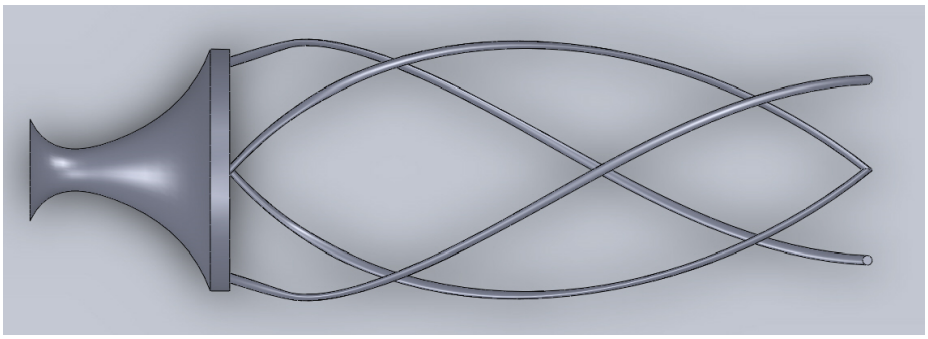

Figure 5.1: A possible integrated micro-robot design capable of 3D non-contact micro-manipulation.

Another approach to achieve 3D non-contact micro-manipulation is to simultaneously implement rotation and gradient-pulling by the external magnetic field. Such an actuation technique has been previously demonstrated [22]. By using a robot body with specific geometries, it is possible for a micro-robot to move in a controllable manner in 3D while still being able to generate proper rotational flow for trapping of objects by its rotation.

5.1.5 Robot Geometry Optimization

In this work, we preliminarily studied the influence of robot shape on the induced rotational flow for several different typical shapes. We concluded that rotationally symmetric robot shape would be more ideal more manipulation purpose based on the observations from Sec. 2.4.3. However, it is inadequate to draw complete conclusion on the optimal robot geometry for this specific purpose. A more comprehensive and

complete optimization should be perform to find the optimal robot geometry. In addition, such optimization could be expanded to other applications as well, such as micro-mixing, particle-sorting and etc.

Two requirements need to be satisfied in order to perform such optimization. The first requirement is the proper optimization goal (metrics) for different application purposes. For example, an uniform flow field is desirable for manipulation purpose, while a more chaotic flow field would result in more efficient mixing. Therefore, it is important to set proper measurements for performance of induced rotational flows for different purposes based on the flow velocity data. The second requirement is a feasible procedure to carry out the optimization. Here we propose two possible procedures:

1) Firstly, a large set of different robot geometries are generated, modeled and meshed. The numerical fluid-dynamics solver is then used to solve for the flow field induced by each geometry in the set. Optimal robot geometry is eventually found from the set based the the flow velocity data and the given metrics. This is not a complete optimization method, and involves multiple separate steps. However, it is less complicated and could be implemented very efficiently.

2) Integrating the numerical solver, geometry generation and an optimization algorithm into one package. Once this integration is ready, complete optimization can be easily carried out for various application purposes. However, the high complexity of integration process makes it more difficult to implement than the first procedure.

5.1.6 Integration of Magnetic Micro-Robots with Microfluidics

In this work, we preliminarily introduced one application of the rotating micro-robot for microfluidics. In fact, given the capability of micro-robots to induce local flows, there are numerous potential applications in microfluidics awaiting for investigation. For example, we envision a narrow channel with micro-vortex-generators arranged in configurations that might allow a single cell to be circulated continuously while moderate flow introduces nutrients and chemical signals, creating a nanobioreactor to study single cell growth in suspension (Fig. 5.2). More aggressive speeds and shapes might also allow on-chip mechanical cell lysis to be incorporated into lab-on-a-chip operations.

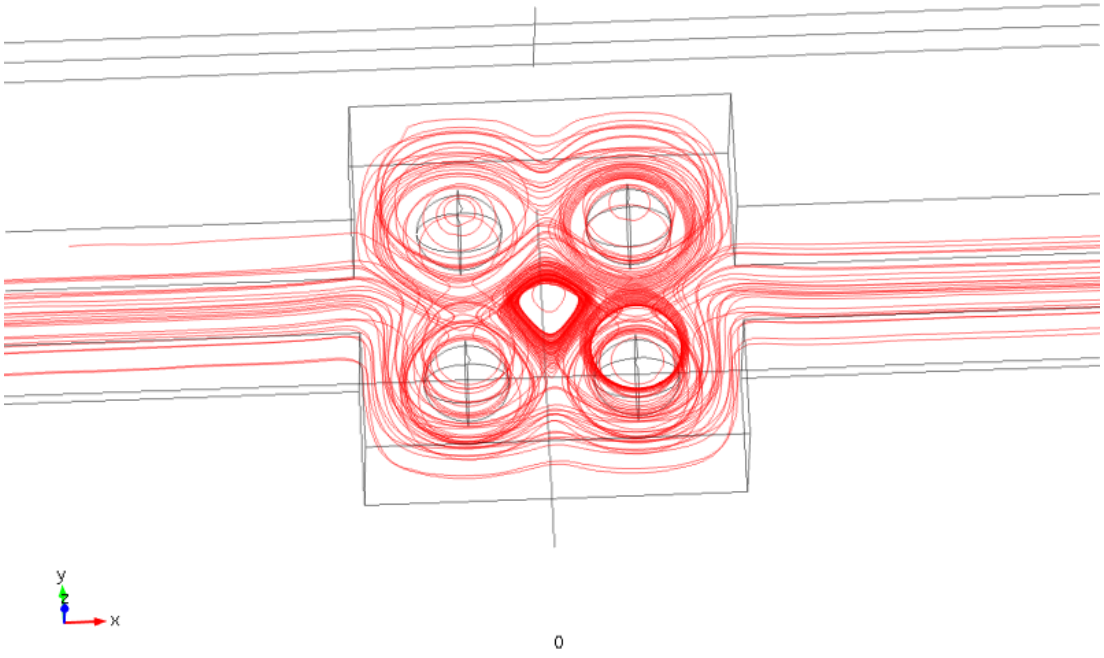

Figure 5.2: Multiple rotating micro-robots creating a circulating flow inside the microfluidic chamber.

Appendix A

Electromagnetic-Coil System for Micro-Robot Actuation

A.1 Six-Electromagnetic-Coil System

To actuate magnetic micro-robots of hundreds of microns in size, described in Chapter 2 and 3, we fabricated computer-controlled six-electromagnetic-coil system which is shown in Fig. A.1. The system consists of six electromagnetic coils, aligned to the faces of a cube approximately 8.2 cm on a side. Depending on the required magnetic fields and gradients, the coils can contain either an air core or an iron core. The system is capable of applying magnetic fields and field gradients to the workspace, which is contained within the coils. Properties of the electromagnetic system are provided in Table A.1. Maximum fields or gradients correspond to using two coaxial coils on opposite sides driven at maximum current, and are measured

using Hall-effect sensors placed in the micro-robot workspace.

Table A.1: Properties of the 6-coil electromagnet system.

Property	**Value**	**Units**
Workspace size	75	mm
Number of turns	140	-
Wire diameter	1.15	mm
Coil length	3.2	cm
Resistance	0.4	Ω
Coil impedance	32	mH
Inner diameter	5.1	cm
Distance to workspace	4.1	cm
Max driving current	19	A
Core length	10.1	cm
Max field at workspace (air core)	12.0	mT
Max gradient at workspace (air core)	0.44	T/m
Max field at workspace (Fe core)	49	mT
Max gradient at workspace (Fe core)	2.2	T/m

Table A.2: Properties of the 5-coil electromagnet system.

Property	In-plane Coils	Out-of-plane Coil
Number of turns	120	90
Resistance (Ω)	0.3	0.2
Wire diameter (mm)	1.024	1.024
Coil length (mm)	28	40
Inner diameter (mm)	23	35
Maximum driving current (A)	9	9
Maximum field at the center (mT)	3.5	8.0

A.2 Five-Electromagnetic-Coil System

To actuate magnetic micro-robots of a few to tens of microns in size, described in Chapter 2 and 4, we fabricated a second computer-controlled five-electromagnetic-coil system which is shown in Fig. A.2. A maximum in-plane magnetic field of 3.5 mT could be achieved, with a maximum out-of-plane magnetic field of 8 mT. The in-plane magnetic field is measured to be uniform within 7.5$\%$ of the nominal value. Properties of the electromagnetic-coil system are provided in Table A.2.

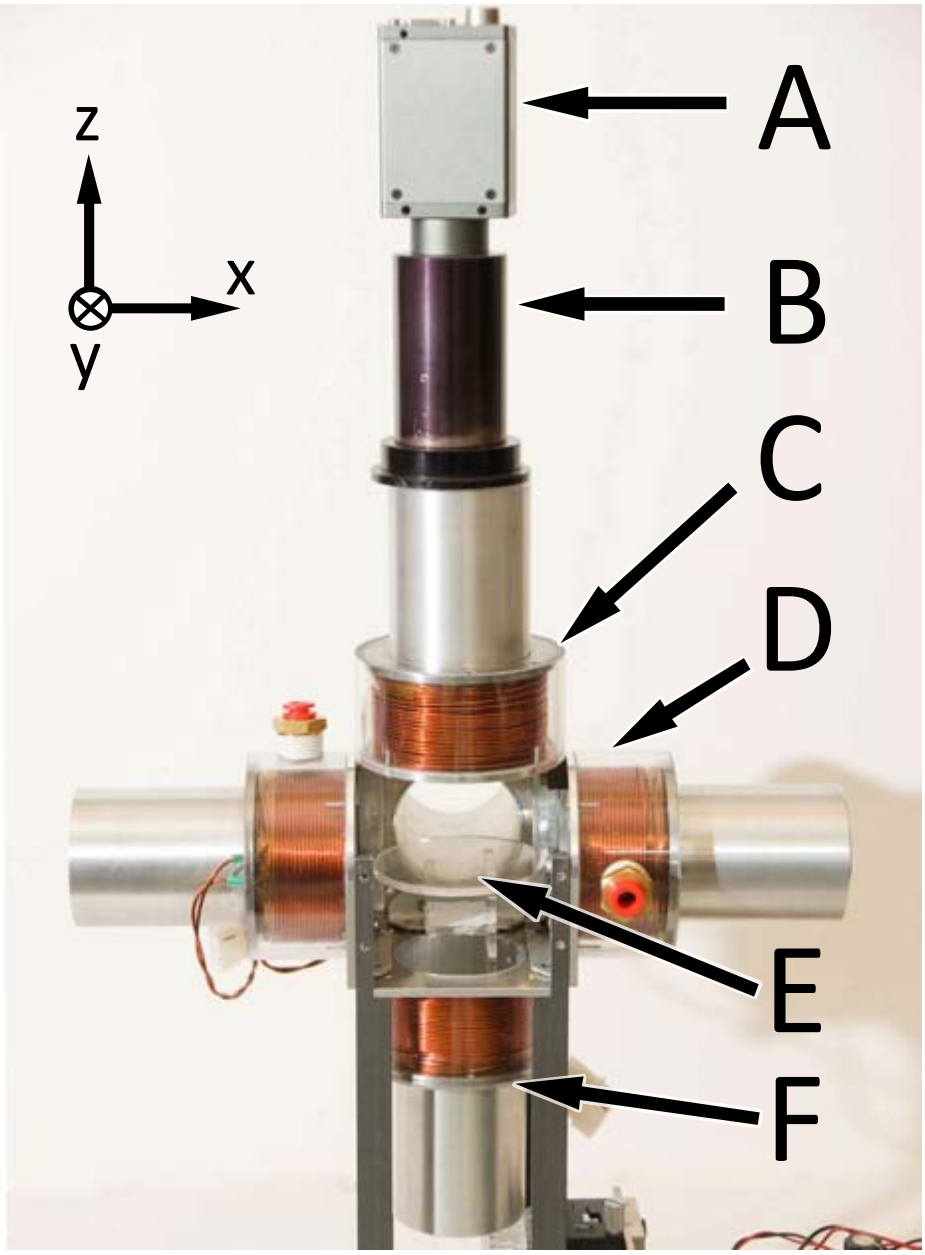

Figure A.1: A: camera for top-view vision feedback, B: microscope lens, C: top +z coil, D: +x coil (one of four horizontal coils), E: experiment workspace, and F: bottom -z coil. The -y coil is removed to allow viewing of the workspace.

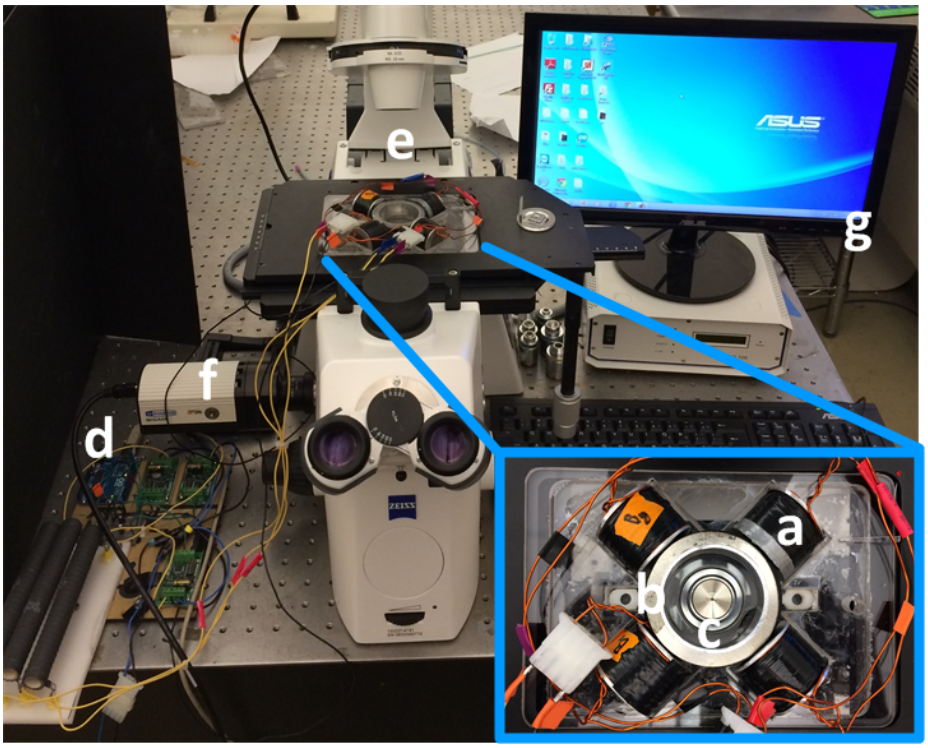

Figure A.2: (a) Four orthogonally oriented iron-core electromagnets were used to generate in-plane uniform magnetic field. (b) A vertically placed solenoid was used to generate out-of-plane uniform magnetic field. (c) The workspace in the center of the solenoid is 40 mm in diameter. (d) The coil current is controlled with an Arduino Uno microcontroller board. (e) The samples were imaged using a 63x objective in an inverted phase contrast microscope (Axio Observer, Carl Zeiss). (f) Images of the samples were captured at 19 frames/s with a CCD digital camera (QICAM 12-bit, QImaging). (g) A desktop computer with customized user interface program communicated with the microcontroller board for real-time adjustment of magnetic field parameters.

Appendix B

Numerical Simulation

B.1 Rotational Flows Induced by A Sphere Spinning on A Surface

Numerical simulations were carried out with commercial package *COMSOL Multiphysics* 4.0a. The laminar flow module built in *COMSOL* is used for modeling. Robot surfaces were modeled as moving walls with a velocity field derived based on the robot's rotating speed. Tetragonal elements are used for meshing over all domains. The meshing of the models is nonuniform, with much higher element density in the neighboring domain of the spinning sphere and lower in the regions far away from it. The maximum number of total element used for simulations is 672,902. Time-dependent solver with absolute/relative tolerance of 10^{-3} is used for all simulations. Once the solving process is complete, simulation results are output directly from *COMSOL* and then analyzed with *MATLAB* 2010a. The $cftool$

toolbox in *MATLAB* is used to find the fitting power function for the flow velocity data.

Results

Multiple simulations are carried out with the same physics model in two cases in order to examine the influence of effective Reynolds number (Re) on velocity falloff. In the first case, the kinematic viscosity ν of the liquid varies while the radius of the spinning sphere R is kept constant at 180 μm. In the other case, radius R varies while the viscosity ν is kept constant at 50 cSt. Velocity data taken from the equatorial plane of the sphere are fitted into a power function with the following form:

$$|\boldsymbol{v}| = \omega_{\perp} R \left(\frac{r}{R}\right)^{c}, \tag{B.1}$$

where c is the unknown parameter to be determined. The fitting results are listed in Table. B.1.

Table B.1: Fitting results of the velocity data from simulations with different effective Re.

Parameter	Viscosity ν (cSt)				Radius R (μm)	
Value	500	50	12.2145	5	180	36
Effective Re	2.44×10^{-2}	2.44×10^{-1}	1	2.44	2.44×10^{-1}	9.76×10^{-3}
c value	-2.43	-2.43	-2.43	-2.53	-2.43	-2.43
R-square of fitting	0.9975	0.9987	0.9974	0.9988	0.9987	0.9980

B.2 Rotational Flows Induced by A Rotating Sphere on A Surface with Non-Zero Translational Speed

Numerical simulations were carried out with commercial package *COMSOL Multiphysics* 4.3. The laminar flow module built in *COMSOL* is used for modeling. The robot was modeled as a 5 μm-diameter sphere immersed in a liquid with a density of 1000 kg/m^3 and a dynamic viscosity of 10^{-3} Pa·s near a substrate. A open-top container enclosed the robot and the object in a space of 100 μm$\times$100 μm$\times$100 μm. Non-slip boundary condition was specified on the sidewalls as well as on the bottom surface of the container. Robot surfaces were modeled as moving walls with a velocity field derived based on the robot's rotation. A constant flow with the same translation speed of the micro-robot but in the opposite direction was imposed onto the whole model to emulate the influence of robot's translation. Tetragonal elements are used for meshing over all domains. The meshing of the models is nonuniform, with much higher element density in the neighboring domain of the spinning robot and lower in the regions far away from it. Time-dependent solver with absolute/relative tolerance of 10^{-3} is used for all simulations.

B.3 Rotational Flows Induced by Rotating Non-Spherical Micro-Robots on A Surface

A customized solver - *stkSolver* was used for this study. This solver uses the Boundary Element Method to solve for Stokes flow problems. Details of implementation

of the solver can be found in [117].

The *stkSolver* does not provide either modeling or meshing function, and hence these two steps were done using other readily available software. Models of robot geometry were first built using a commercial FEA software *ADINA* 9.0 as well as a separate model of underlying substrate. In the next step, structured meshing was generated on the surfaces of the robot models and the substrate separately using three-node triangular elements. The meshed surfaces were then exported to another software - *gmsh* 2.8.4 to turn the three-node triangular elements into six-node triangular elements by adding midway points onto each edge of the elements. Finally, the complete meshing was loaded into *MATLAB* to rearrange the order of nodes inside each elements and combine the robot surface and the substrate so that the output meshing was readable by *stkSolver*. Input files were generated by *MATLAB* based on the imported meshing and the problem being investigated and then solved with *stkSolver*. After solutions were obtained, velocity data in the space was exported to be analyzed on *MATLAB*.

B.4 Forces on A Sphere Inside Rotational Flow Induced by A Spherical Micro-Robot

Numerical simulations were carried out with commercial package *COMSOL Multiphysics* 4.3. The laminar flow module built in *COMSOL* is used for modeling. The robot was modeled as a 30 μm-diameter sphere while the object was modeled as a second sphere fixed at certain distance from the robot. A open-top container enclosed

the robot and the object in a space of 300 μm×300 μm×150 μm. Non-slip boundary condition was specified on the sidewalls as well as on the bottom surface of the container. Robot surfaces were modeled as moving walls with a velocity field derived based on the robot's rotating speed. Tetragonal elements are used for meshing over all domains. The meshing of the models is nonuniform, with much higher element density in the neighboring domain of the spinning robot and object and lower in the regions far away from it. Time-dependent solver with absolute/relative tolerance of 10^{-3} is used for all simulations. A snapshot of the model is given in Fig. B.1.

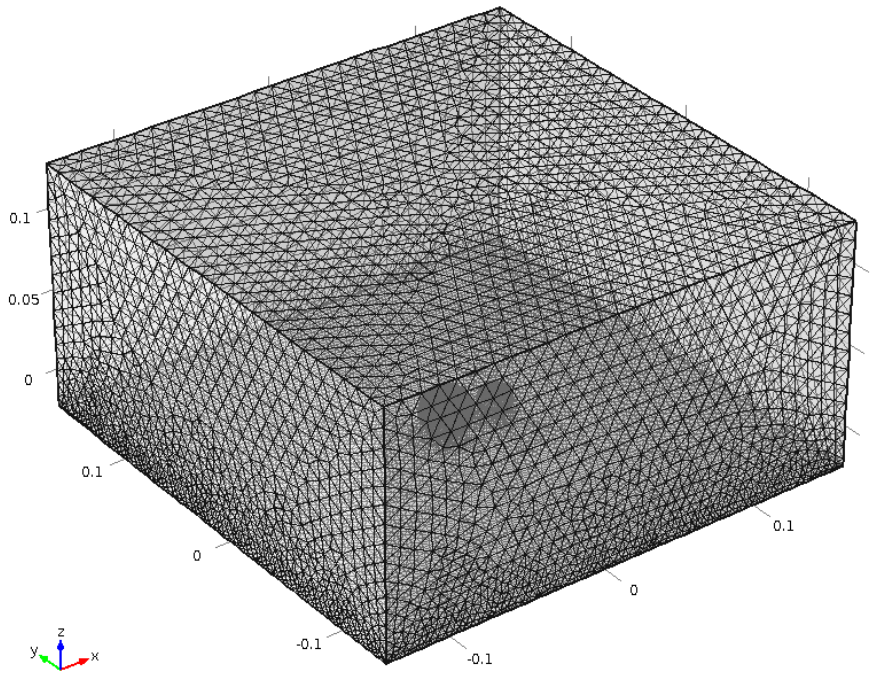

Figure B.1: Model built on *COMSOL* for numerical study on the forces applied a sphere inside rotational flow induced by a spherical micro-robot.

For study of the drag force, a total number of 390,534 element was used. The

object was modeled as a sphere fixed in place with zero translational velocity. Non-slip boundary condition was specified on the surface of object. After a converging solution was reached, integral of the stress was performed over the robot surface in tangential direction to obtained the drag force experienced by the object. For study of the radial forces, a total number of 1,872,155 element was used. The object was modeled as a sphere moving with non-zero translational velocity. To find the steady-state traveling of object, different velocity values were specified in an iterative manner until the drag force obtained approached zero. Then two simulations were carried out, one under Stokes flow condition, the other solving the full Navier-Stokes equations. Both simulations were done using *COMSOL*'s built-in function.

Appendix C

Electroplated Nickel Docks

Using sputtering to create magnetic features imposes some undesirable limitations that we sought to overcome as we further explored the use of docking substrates. Sputtering is expensive and slow, depositing approximately 8 nm/min. Above thicknesses of 500 nm, the stress generated within the deposited film can cause cracking and delamination, making lift-off resists an ineffective approach. We therefore concomitantly fabricated electroplated versions of the magnetic docking arrays to overcome the thickness limitations associated with sputtering.

Glass wafers were cleaned and coated with a 100 nm copper seed layer (CVC Connexion Sputtering System, 250 W forward power). The copper layer was then masked with a thick ($\sim$15 μm) layer of AZ-4620 photoresist, spun at 1000 rpm for 120 seconds, and softbaked for 5 minutes at 95°C. The wafer was exposed in vacuum contact mode with the chrome photomask for 135 seconds at 5 mW/cm^2, then developed in 1:4 AZ-400K developer solution for 5 minutes. Prior to electroplating,

a 1 minute, 100 W plasma descum was performed to remove any remaining residue and ensure good electrical conduction in the exposed regions.

Electroplating was performed using a commercially available nickel electroplating kit (Caswell #NP3). The prepared wafer was attached to an acrylic holder using copper tape. Tape was applied to the edges of the wafer where the protective resist layer had been removed with an acetone soaked cotton swab. A digital multimeter was used to confirm good electrical contact between the copper seed layer on the wafer and the power supply connector. Before introducing the wafer to the electroplating solution, it was sonicated in DI water for 3 minutes to remove air bubbles trapped in the resist features and ensure uniform plating. After sonication, the wet wafer was transferred to the electroplating bath, which was maintained at 50°C during plating. A sacrificial nickel anode was submerged on the opposite side of the bath, and connected to the positive terminal. The wafer was then connected to the negative terminal of the power supply. Electroplating of the docks was performed at 100 mA forward current and a voltage of 1.52 V for 10 minutes. After plating the wafer was removed and rinsed thoroughly with DI water, then dried with nitrogen.

The plated wafer was rinsed in acetone to remove the photoresist layer. The copper layer was then removed by etching for 20 seconds in Aluminum A Transene etchant. The etch time was formulated to completely remove the copper seed layer around the nickel docks, but avoid undercutting them and compromising their adhesion. After etching, the wafer was rinsed with DI water, dried, and diced into individual substrates for use in experiments.

Electroplated docks were less uniform than sputtered docks, and exhibited thick-

nesses ranging from (get numbers from lab notebook) to (blank) within single docks. Thickness was greater at the edges of the features, creating a concave structure that might benefit from ”cradling” the micro-robots by conforming to a semi-spherical shape. However, we found little difference between sputtered and electroplated docks in practice. The performance of sputtered docks was even more stable in general, which may be attributed to the more well formed structures.

Appendix D

Line-Test for 3D Printing

Characterization of printing parameters was performed using line tests, as seen in Fig. D.1. The TPP laser was rapidly scanned through a wide range of power and speed parameters, creating narrow lines of polymerized resist on the glass surface that could be imaged via SEM. Line tests for scan speeds from 100-10,000 μm/s and powers from 0-100% were performed for all 6 concentrations of IP-G composite to indicate the range of feasible parameters for printing. We found SU-8 adhesion to glass too weak to reliably perform and image line tests or print 3-dimensional structures. We therefore chose to perform the remaining experiments using IP-G composites.

Line tests, when compiled into a contour plot (Fig. D.2), indicate the effects of resist composition on ideal printing parameters. There is a general trend toward a narrowing of parameter space as increased volume fractions of magnetic nanoparticles are used. This is to be expected, as scattering, absorption, and localized heat-

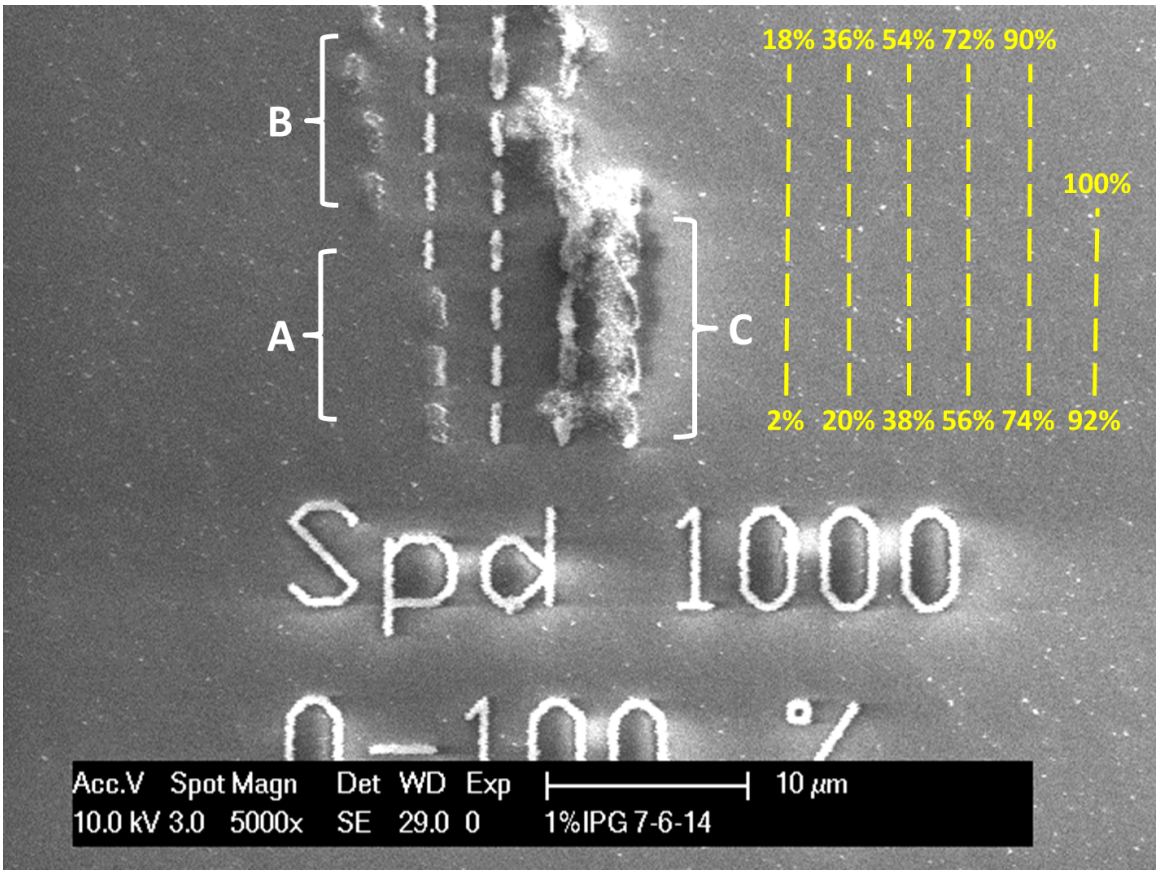

Figure D.1: Sample SEM image of the line test used to characterize writing parameters. Sample is IP-G resist containing 1 vol.% magnetite MNPs. Lines are written with increasing power from left to right, bottom to top, in a snaking fashion, with power changing in 2% increments from 0-100%. On the left-hand side, lines are missing (A) or poorly polymerized (B) due to insufficient power and poor adhesion. On the right, excessive power caused localized heating, monomer degradation, and gas formation that destroyed the feature resolution (C).

ing increase along with particle concentration. Slight inconsistencies of this pattern are likely attributable to high variability when working near the limits of speed and power, as well as run-to-run variability in substrate cleanliness and surface adhesion. Fischer et al. performed similar characterization plots of polymerization and damage thresholds, comparing pulse energy and repetition rates for a number of other photoresists [118].

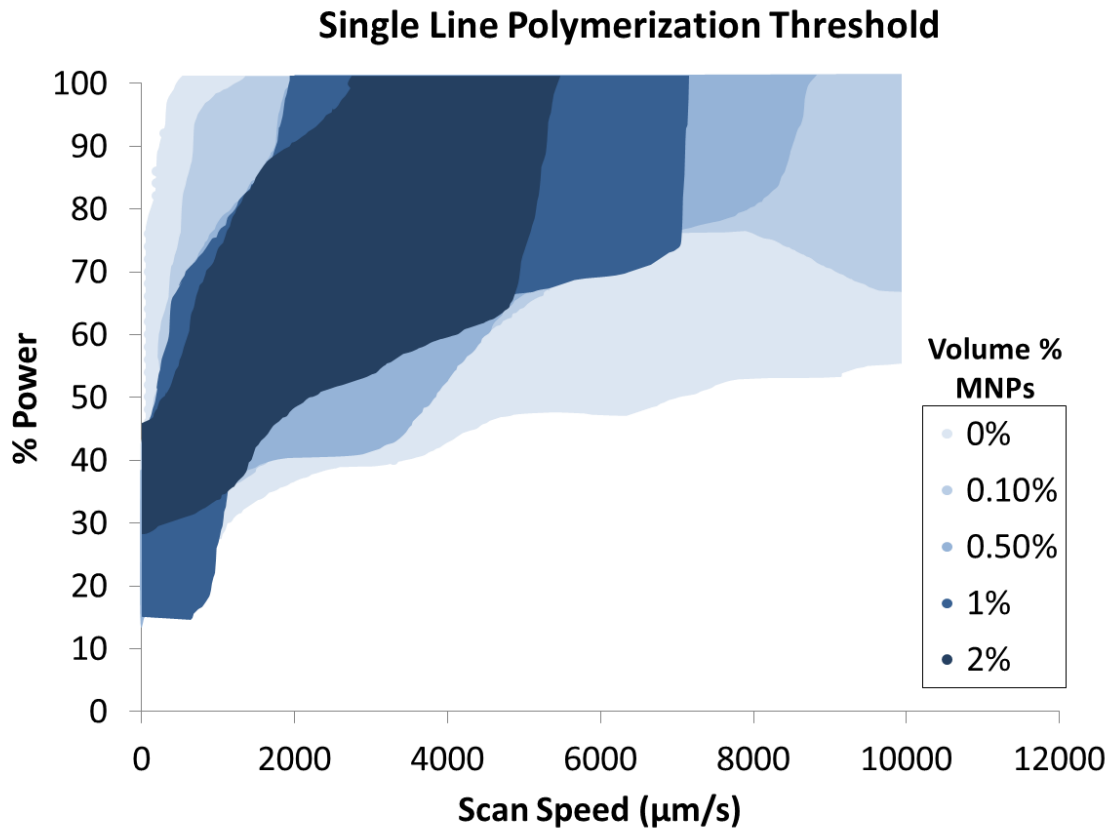

Figure D.2: Polymerization threshold of IP-G magnetic nanoparticle composite. Colored regions highlight combinations of laser power and scan speed that create well-formed lines on the surface of glass substrates. Parameters above these contours result in localized heating, monomer degradation, and gas evolution. Parameters below the contours result in insufficient polymerization and/or weak adhesion. Increasing concentrations of magnetic nanoparticles (vol.%) are shown in successively darker shades.

Appendix E

Preliminary Size-Based Particle-Sorting in Microfluidic Channels

Two spherical micro-robots were arranged consecutively onto the nickel docks within microfluidic channels, and polystyrene beads of varying sizes were injected through the top inlet. Buffer flow through the bottom inlet was controlled to adjust the interface of the two inlet flows just above the midpoint of the first micro-robot. By ensuring that most particles passed between the micro-robot and the channel wall when no field was applied, we ensured that the particles would be forced to pass within capture range. After establishing stable flow, a rotational field was applied, and particles were deflected from their normal paths, with some particles exchanging orbits from one micro-robot to the next (hand-off).

We observed a gradual increase in mean and median lateral migration with increase in particle size. Two tailed student t-tests assuming equal variances indicated

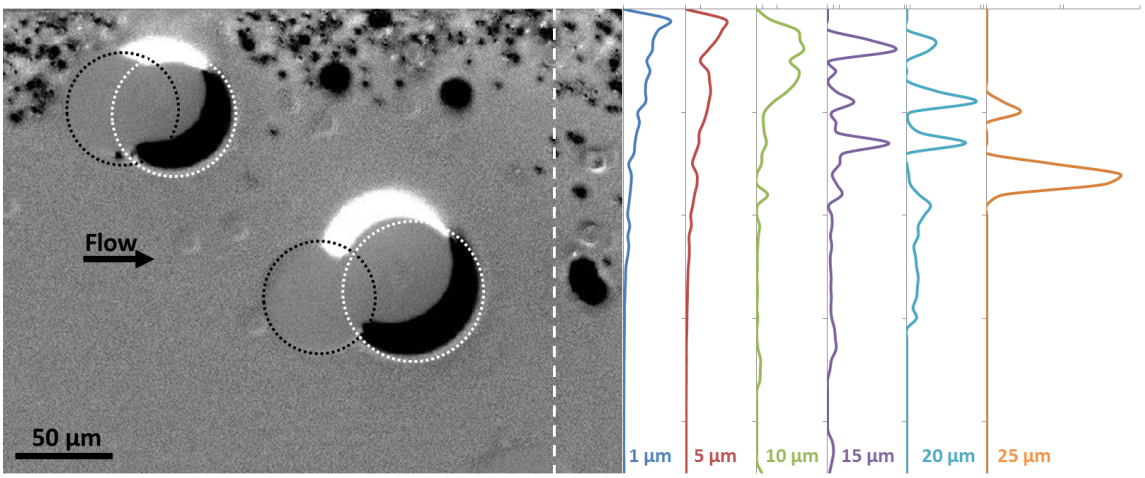

Figure E.1: Freezeframe of high-speed footage of spinning microspheres (white dotted outline) on magnetic docks (black dotted outline) with polystyrene beads of various sizes. Vertical distribution (in 5 µm increments) of particle sizes are shown for bins around discrete microsphere diameters. Distributions are normalized to the total number of particles in each bin. Flow rate is 3.03 µL/min, number of frames combined = 3,654. Field strength = 1.5 mT, rotation frequency = 20 Hz.

that the mean particle displacement of all groups were statistically different from one another ($p<0.01$) with the exception of the comparisons between the 20 and 25 μm size groups. This may be the result of lower particle counts for larger PS beads. However, this observation seems not to be in complete agreement with the results from Sec. 4.5.3. Such seeming discrepancy could arise due to two reasons. First, a portion of the beads could enter the induced rotational flow region in between the two micro-robots instead of between the first robot and the wall. Although the boundary of the flows from two inlets was adjusted to be close to the center of the first robot, the lateral forces naturally appearing in shear flows, as discussed in Sec. 4.4.1, could cause the particles to cross the boundary already before they entered the disturbed flow region. Such lateral forces could be more significant on beads with larger size, which resulted in a more apparent lateral migration in the undisturbed flow region for larger beads. Beads affected by such effect were not filtered out from the beads that were actually diverted by the rotational flows as we were only looking at the final y-position of the beads when they left the field of view. The second, but more plausible reason is that such discrepancy may arise from the differences in flow rate and spinning speed for the two experiments. A lower flow rate and a higher spinning speed were used in this experiment. This resulted in stronger shear gradients inside the induced rotational flows, and slower flow velocities everywhere else inside the channel. Higher shear gradients could lead to more significant inertia-induced lateral forces, while the centrifugal force is sensitive to the traveling speed of particle. Therefore, it would be expected to be easier for the larger particles to migrate between streamlines towards the rotating robot with the higher spinning speed and

lower flow rate, which agrees with the observation. According to the experimental results from Sec. 4.5.3 and this section, the size-dependent lateral migration of particles inside the induced rotational flow can be tuned by adjusting the spinning speed and the flow rate to change significantly. In fact, this could be a potential advantage of the proposed approach as it is possible to achieve different size-dependent migration behavior without physically change the structure of the system. This feature is not easily achievable for many other sorting methods.

Bibliography

[1] M. Sitti, "Voyage of the microrobots," *Nature*, vol. 458, pp. 1121–1122, 2009. 1.2.1

[2] M. Sitti, "Microscale and nanoscale robotics systems [grand challenges of robotics]," *IEEE Robotics and Automation Magazine*, vol. 14, pp. 53–60, 2007. 1.2.1

[3] B. Donald, C. Levey, and I. Paprotny, "Planar microassembly by parallel actuation of mems microrobots," *Journal of Microelectromechanical Systems*, vol. 17, pp. 789–808, 2008. 1.2.1, 1.1

[4] M. Sakar, E. Steager, D. Kim, A. Juliusz, M. Kim, V. Kumar, and G. Pappas, "Modeling, control and experimental characterization of microbiorobots," *The International Journal of Robotics Research*, vol. 30, pp. 647–658, 2011. 1.2.1, 1.1

[5] C. Pawashe, S. Floyd, and M. Sitti, "Modeling and experimental characterization of an untethered magnetic micro-robot," *International Jounral of Robotics Research*, vol. 28, pp. 1077–1094, 2009. 1.2.1, 1.1, 2.2.2, 2.4.1

[6] K. Vollmers, D. Frutiger, B. Kratochvil, and B. Nelson, "Wireless resonant magnetic microactuator for untethered mobile microrobots," *Applied Physics Letters*, vol. 92, p. 144103, 2008. 1.2.1, 1.1

[7] L. Zhang, Y. Lu, L. Dong, R. Pei, J. Lou, B. Kratochvil, and B. Nelson, "Noncontact manipulation of ni nanowires using a rotating magnetic field," in *IEEE International Conference on Nanotechnology*, (Italy), pp. 487–490, 2009. 1.2.1, 1.1

[8] A. Yamazaki, M. Sendoh, K. Ishiyama, K. I. Arai, R. Kato, M. Nakano, , and H. Fukunaga, "Wireless micro swimming machine with magnetic thin film," *J. of Mag. and Mag. Mat.*, vol. 272–276, pp. 1741–1742, 2004. 1.2.1

[9] E. Steager, M. Sakar, C. Magee, M. Kennedy, A. Cowley, and V. Kumar, "Automated biomanipulation of single cells using magnetic microrobots," *The International Journal of Robotics*, vol. 32, pp. 346–359, 2013. 1.2.1, 1.2.1, 1.1, 1.2.2, 2.1

[10] O. Sul, M. Falvo, R. Taylor, S.Washburn, and R. Superfine, "Thermally actuated untethered impact-driven locomotive microdevices," *Applied Physics Letters*, vol. 89, p. 203512, 2006. 1.2.1, 1.1

[11] A. Buzas, L. Kelemen, A. Mathesz, L. Oroszi, G. Vizsnyiczai, T. Vicsek, and P. Ormos, "Light sailboats: Laser driven autonomous microrobots," *Applied Physics Letters*, vol. 101, p. 041111, 2012. 1.2.1, 1.1

[12] W. Hu, K. Ishii, and A. Ohta, "Micro-assembly using optically controlled bubble microrobots," *Apply Physics Letters*, vol. 99, p. 094103, 2011. 1.2.1, 1.2.1, 1.1, 1.2.2, 2.1

[13] A. Solovev, Y. Mei, E. B. Ureña, G. Huang, and O. Schmidt, "Catalytic microtubular jet engines self-propelled by accumulated gas bubbles," *Small*, vol. 5, pp. 1688–1692, 2009. 1.2.1, 1.2

[14] G. Hwang, R. Braive, L. Couraud, O. A. a. Cavanna, I. Robert-Philip, a. Beveratos,

I. Sagnes, S. Haliyo, and S. Régnier, "Electro-osmotic propulsion of helical nanobelt swimmers," *The International Journal of Robotics Research*, vol. 30, pp. 806–819, 2011. 1.2.1, 1.2

[15] R. Dreyfus, J. Baudry, M. Roper, M. Fermigier, H. Stone, and J. Bibette, "Microscopic artificial swimmers," *Nature*, vol. 437, pp. 0862–865, 2005. 1.2.1, 1.2

[16] O. Ergeneman, G. Dogangil, M. P. Kummer, J. Abbott, M. Nazeeruddin, and B. Nelson, "A magnetically controlled wireless optical oxygen sensor for intraocular measurements," *IEEE Sensors Journal*, vol. 8, pp. 2022–2024, 2008. 1.2.1

[17] S. Martel, O. Felfoul, J.-B. Mathieu, A. Chanu, S. Tamaz, M. Mohammadi, M. Mankiewicz, and N. Tabatabaei, "Mri-based medical nanorobotic platform for the control of magnetic nanoparticles and flagellated bacteria for target interventions in human capillaries," *International Journal of Robotics Research*, vol. 28, pp. 1169–1182, 2009. 1.2.1, 1.2.1, 1.2, 2.1

[18] L. Zhang, J. Abbott, L. Dong, B. Kratochvil, D. Bel, and B. Nelson, "Artificial bacterial flagella: Fabrication and magnetic control," *Applied Physics Letters*, vol. 94, p. 064107, 2009. 1.2.1, 1.2, 2.1

[19] A. Ghosh and P. Fischer, "Controlled propulsion of artificial magnetic nanostructured propellers," *Nano letters*, vol. 9, pp. 2243–2245, 2009. 1.2.1, 1.2

[20] M. Kummer, J. Abbott, B. Kratochvil, R. Borer, A. Sengul, and B. Nelson, "Octomag: An electromagnetic system for 5-dof wireless micromanipulation," *Robotics, IEEE Transactions on*, vol. 26, pp. 1006–1117, 2010. 1.2.1, 1.2.1, 1.2

[21] O. Pak, W. Gao, J. Wang, and E. Lauga, "High-speed propulsion of flexible nanowire

motors: Theory and experiments," *Soft Matter*, vol. 7, pp. 8169–8181, 2011. 1.2.1, 1.2, 3.1, 3.5

[22] E. Diller, J. Giltinan, and M. Sitti, "Independent control of multiple magnetic microrobots in three dimensions," *International Journal of Robotics Research*, vol. 32, no. 5, pp. 614–631, 2013. 1.2.1, 5.1.4

[23] B. Behkam and M. Sitti, "Bacterial flagella-based propulsion and on/off motion control of microscale objects," *Applied Physics Letters*, vol. 90, p. 023902, 2007. 1.2.1, 1.2

[24] D. Kim, P. Kim, A. Julius, and M. Kim, "Three-dimensional control of tetrahymena pyriformis using artificial magnetotaxis," *Applied Physics Letters*, vol. 100, p. 053702, 2012. 1.2.1, 1.2

[25] V. Magdanz, S. Sanchez, and O. Schmidt, "Development of a sperm-flagella driven micro-bio-robot," *Advanced Materials*, vol. 25, pp. 6581–6588, 2013. 1.2.1, 1.2

[26] K. Peyer, L. Zhang, and B. Nelson, "Localized non-contact manipulation using artificial bacterial flagella," *Applied Physics Letters*, vol. 99, p. 174101, 2011. 1.2.1, 1.2.2, 2.1

[27] S. Floyd, C. Pawashe, and M. Sitt, "Two-dimensional contact and non-contact micromanipulation in liquid using an untethered mobile magnetic micro-robot," *IEEE Transactions on Robotics*, vol. 25, pp. 1332–1342, 2009. 1.2.1, 1.2.2, 2.4.1

[28] T. Petit, L. Zhang, K. Peyer, B. Kratochvil, and B. Nelson, "Selective trapping and manipulation of microscale objects using mobile microvortices," *Nano Letters*, vol. 12, pp. 156–160, 2012. 1.2.1, 1.2.2, 2.1

[29] E. Diller and M. Sitti, "Three-dimensional programmable assembly by untethered magnetic robotic micro-grippers," *Advanced Functional Materials*, vol. 24, pp. 4397–4404, 2014. 1.2.1, 1.2.2, 2.1

[30] E. Diller, N. Zhang, and M. Sitti, "Heat-based bonding for modular micro-robotic assemblies," *Journal of Micro-Bio Robotics*, vol. 8, pp. 121–131, 2013. 1.2.1

[31] C.-J. Kim, A. Pisano, and R. Muller, "Silicon-processed overhanging microgripper," *Journal of Microelectromechanical Systems*, vol. 1, no. 1, pp. 31–36, 1992. 1.2.2

[32] D.-H. Kim, B. Kim, and H. Kang, "Development of a piezoelectric polymer-based sensorized microgripper for microassembly and micromanipulation," *Microsystem Technologies*, vol. 10, no. 4, pp. 275–280, 2004. 1.2.2

[33] L. Kremser, D. Blaas, and E. Kenndler, "Capillary electrophoresis of biological particles: Viruses, bacteria, and eukaryotic cells," *Electrophoresis*, vol. 25, pp. 2282–2291, 2004. 1.2.2

[34] P. Chiou, A. Ohta, and M. Wu, "Massively parallel manipulation of single cells and microparticles using optical images," *Nature*, vol. 436, pp. 370–372, 2005. 1.2.2

[35] D. Grier, "Review article a revolution in optical manipulation," *Nature*, vol. 424, pp. 810–816, 2003. 1.2.2

[36] Y. Jiang, Y. Matsumoto, and Y. Hosokawa, "Trapping and manipulation of a single micro-object in solution with femtosecond laser-induced mechanical force," *Applied Physics Letters*, vol. 90, p. 061107, 2007. 1.2.2

[37] H. Lee, A. Purdon, and R. Westervelt, "Manipulation of biological cells using a microelectromagnet matrix," *Applied Physics Letters*, vol. 85, p. 1063, 2004. 1.2.2

[38] X. Ding, S.-C. Lin, B. Kiraly, H. Yue, S. Li, I.-K. Chiang, J. Shi, S. Benkovic, and T. Huang, "On-chip manipulation of single microparticles, cells, and organisms using surface acoustic waves," *Proceedings of the National Academy of Sciences of the United States of America*, vol. 109, pp. 11105–11109, 2012. 1.2.2

[39] A. Masuda, T. Yamakawa, and L. Zimin, "Micromanipulation system based on local vibration," *in SICE Annual Conference*, vol. 2, pp. 1747–1750, 2008. 1.2.2

[40] M. Eglin, M. A. Eriksson, and R. Carpick, "Microparticle manipulation using inertial forces," *Applied Physics Letters*, vol. 88, p. 091913, 2006. 1.2.2

[41] S. Chung and S. Cho, "On-chip manipulation of objects using mobile oscillating bubbles," *Journal of Micromechanics and Microengineering*, vol. 18, p. 125024, 2008. 1.2.2

[42] G. Whitesides, "The origins and the future of microfluidics," *Nature*, vol. 442, pp. 368–373, 2006. 1.2.2

[43] L. Yeo, H.-C. Chang, P. Chan, and J. Friend, "Microfluidic devices for bioapplications," *Small*, vol. 7, pp. 12–48, 2011. 1.2.2

[44] N. Pamme, "Magnetism and microfluidics," *Lab on a Chip*, vol. 6, pp. 24–38, 2006. 1.2.2

[45] S. Choi, J. M. Karp, and R. Karnik, "Cell sorting by deterministic cell rolling," *Lab on a Chip*, vol. 12, pp. 1427–1430, 2012. 1.2.3

[46] J. Bulte, D. Kraitchman, A. Mackay, M. Pittenger, A. Arbab, G. Yocum, H. Kalish, E. Jordan, S. Anderson, A. Khakoo, E. Read, and J. Frank, "Chondrogenic differentiation of mesenchymal stem cells is inhibited after magnetic labeling with ferumox-

ides," *Blood*, vol. 104, pp. 3410–3412, 2004. 1.2.3

[47] M. Chabert and J.-L. Viovy, "Microfluidic high-throughput encapsulation and hydrodynamic self-sorting of single cells," *Proc. Natl. Acad. Sci. U. S. A.*, vol. 105, pp. 3191–3196, 2008. 1.2.3

[48] M. Godin, F. Delgado, S. Son, W. Grover, A. Bryan, A. Tzur, P. Jorgensen, K. Payer, A. Grossman, M. Kirschner, and S. Manalis, "Using buoyant mass to measure the growth of single cells," *Nature Methods*, vol. 7, pp. 387–390, 2010. 1.2.3

[49] S. Shim, P. Gascoyne, J. Noshari, and K. Hale, "Dynamic physical properties of dissociated tumor cells revealed by dielectrophoretic field-flow fractionation," *Integrative Biology*, vol. 3, pp. 850–862, 2011. 1.2.3

[50] A. Kose, B. Fischer, L. Mao, and H. Koser, "Label-free cellular manipulation and sorting via biocompatible ferrofluids," *Proc. Natl. Acad. Sci. U. S. A.*, vol. 106, pp. 21478–21483, 2009. 1.2.3

[51] Y. Xu, C. X. Zhang, D. Janasek, and A. Manz, "Sub-second isoelectric focusing in free flow using a microfluidic device," *Lab on a Chip*, vol. 3, pp. 224–227, 2003. 1.2.3

[52] I. Doh and Y. Cho, "A continuous cell separation chip using hydrodynamic dielectrophoresis (dep) process," *Sensors and Actuators, A*, vol. 121, pp. 59–65, 2005. 1.2.3

[53] N. Pamme and C. Wilhelm, "Continuous sorting of magnetic cells via on-chip free-flow magnetophoresis," *Lab on a Chip*, vol. 6, pp. 974–980, 2006. 1.2.3, 4.1

[54] F. Shen, H. Hwang, Y. Hahn, and J.-K. Park, "Label-free cell separation using a

tunable magnetophoretic repulsion force," *Analytical Chemistry*, vol. 84, pp. 3075–3081, 2012. 1.2.3

[55] T. Laurell, F. Petersson, and A. Nilsson, "Chip integrated strategies for acoustic separation and manipulation of cells and particles," *Chemical Society Reviews*, vol. 36, pp. 492–506, 2007. 1.2.3

[56] M. P. MacDonald, G. Spalding, and K. Dholakia, "Microfluidic sorting in an optical lattice," *Nature*, vol. 426, pp. 421–424, 2003. 1.2.3

[57] X. Wang, S. Chen, M. Kong, Z. Wang, K. Costa, R. Li, and D. Sun, "Enhanced cell sorting and manipulation with combined optical tweezer and microfluidic chip technologies," *Lab on a Chip*, vol. 11, pp. 3656–3662, 2011. 1.2.3

[58] J. Takagi, M. Yamada, M. Yasuda, and M. Seki, "Continuous particle separation in a microchannel having asymmetrically arranged multiple branches," *Lab on a Chip*, vol. 5, pp. 778–784, 2005. 1.2.3

[59] R. Jäggi, R. Sandoz, and C. Effenhauser, "Microfluidic depletion of red blood cells from whole blood in high-aspect-ratio microchannels," *Microfluid. Nanofluid.*, vol. 3, pp. 47–53, 2007. 1.2.3

[60] P. Sethu, A. Sin, and M. Toner, "Microfluidic diffusive filter for apheresis (leukapheresis)," *Lab on a Chip*, vol. 6, pp. 83–89, 2006. 1.2.3

[61] D. Frutiger, K. Vollmers, B. Kratochvil, and B. Nelson, "Small, fast, and under control: Wireless resonant magnetic micro-agents," *The International Journal of Robotics Research*, vol. 29, pp. 613–636, 2010. 2.1

[62] H. Maruyama, T. Fukuda, and F. Arai, "Laser manipulation and optical adhesion

control of a functional gel-microtool for on-chip cell manipulation," in *IEEE/RSJ International Conference on Intelligent Robots and Systems*, (St. Louis, MO, USA), pp. 1413–1418, 2009. 2.1

[63] C. Pawashe, S. Floyd, E. Diller, and M. Sitti, "2-d autonomous micro-particle manipulation strategies for magnetic micro-robots in fluidic environments," *Robotics, IEEE Transactions on*, vol. 128, pp. 467–477, 2012. 2.1

[64] E. Diller, S. F. C. Pawashe, and M. Sitti, "Control of multiple heterogeneous magnetic micro-robots in two dimensions," *IEEE Transactions on Robotics*, vol. 28, pp. 172–182, 2012. 2.2.2

[65] Q. Liu and A. Prosperetti, "Wall effects on a rotating sphere," *Journal of Fluid Mechanics*, vol. 657, pp. 1–21, 2010. 2.4.1, 2.4.2, 2.5.1, 2.5.1

[66] G. Jeffery, "On the steady rotation of a solid of revolution in a viscous fluid," *Proceedings of the London Mathematical Society*, vol. 14, pp. 32–338, 1915. 2.4.1

[67] B. Sumer and M. Sitti, "Rolling and spinning friction characterization of fine particles using lateral force microscopy based contact pushing," *Journal of Adhesion Science and Technology*, vol. 2, pp. 481–506, 2008. 2.4.1

[68] J. Happel and H. Brenner, *Low Reynolds Number Hydrodynamics: with special applications to particulate media*. Springer, 1973. 2.4.2

[69] E. Nierop, S. Luther, J. Bluemink, J. Magnaudet, A. Prosperetti, and D. Lohse, "Drag and lift forces on bubbles in a rotating flow," *J. Fluid Mech.*, vol. 571, pp. 439–454, 2007. 2.4.4

[70] P. Cherukat and J. Mclaughlin, "The inertial lift on a rigid sphere in a linear shear

flow field near a flat wall," *J. Fluid Mech.*, vol. 263, pp. 1–18, 1994. 2.4.4, 4.4.1

[71] G. Krishnan and J. D. Leighton, "Inertial lift on a moving sphere in contact with a plane wall in a shear flow," *Phys. Fluids*, vol. 7, p. 2538, 1995. 2.4.4, 2.4.4, 2.4.4

[72] L. Landau and E. Lifshitz, *Fluid Mechanics*. Pergamon, 1987. 2.4.4

[73] P. Saffman, "The lift on a small sphere in a slow shear flow," *J. Fluid Mech.*, vol. 22, pp. 385–400, 1965. 2.4.4, 2.4.4, 4.4.1

[74] J. Israelachvili, *Intermolecular and Surface Forces*. Academic Press, 1992. 2.4.4

[75] K. Fuller and D. Tabor, "The effect of surface roughness on the adhesion of elastic solids," *Proc. R. Soc. Lond. A*, vol. 345, pp. 327–342, 1975. 2.4.4

[76] L. Pasol, A. Sellier, and F. Feuillebois, "A sphere in a second degree polynomial creeping flow parallel to a wall," *Q. J. Mech. Appl. Math.*, vol. 59, pp. 587–614, 2006. 2.4.4, 2.5.1

[77] M. Chaoui and F. Feuillebois, "Creeping flow around a sphere in a shear flow close to a wall," *Q. J. Mech. Appl. Math.*, vol. 56, pp. 381–410, 2003. 2.4.4, 2.5.1

[78] R. Fleck, S. Romero-Steiner, and M. Nahm, "Use of hl-60 cell line to measure opsonic capacity of pneumococcal antibodies," *Clinical and Vaccine Immunology*, vol. 12, pp. 19–27, 2005. 2.5.2

[79] Y. Chisti, "Hydrodynamic damage to animal cells," *Critical Reviews in Biotechnology*, vol. 21, pp. 67–110, 2001. 2.5.2

[80] B. Behkam and M. Sitti, "Design methodology for biomimetic propulsion of miniature swimming robots," *ASME Journal of Dynamic Systems, Measurement, and Con-*

trol, vol. 128, pp. 36–43, 2006. 3.1

[81] U. Cheang, D. Roy, J. Lee, and M. Kim, "Fabrication and magnetic control of bacteria-inspired robotic microswimmers," *Apply Physics Letters*, vol. 97, p. 213704, 2010. 3.1

[82] W. Gao, S. Sattayasamitsathit, K. Manesh, D. Weihs, and J. .Wang, "Magnetically powered flexible metal nanowire motors," *Journal of the American Chemical Society*, vol. 132, p. 14403, 2010. 3.1

[83] P. Garstecki, P. Tierno, D. Weibel, F. Sagues, and G. Whitesides, "Propulsion of flexible polymer structures in a rotating magnetic field," *Journal of Physics: Condensed Matter*, vol. 21, pp. 204110–204117, 2009. 3.1

[84] J. Singleton, E. Diller, T. Andersen, S. Régnier, and M. Sitti, "Micro-scale propulsion using multiple flexible artificial flagella," in *IEEE/RSJ International Conference on Robots and Intelligent Systems*, (San Francisco, CA, USA), pp. 1687–1692, 2011. 3.1

[85] P. Raven, G. Johnson, K. Mason, J. B. Losos, and S. Singer, *McGraw-Hill Connect Biology*. McGraw-Hill Education, 2014. 3.1

[86] B. Korgel, "Nanosprings take shape," *Science*, vol. 309, pp. 1683–1684, 2005. 3.3.1

[87] T. Ui, R. Hussey, and R. Roger, "Stokes drag on a cylinder in axial motion," *Physics of Fluids*, vol. 27, pp. 787–795, 1984. 3.4.2

[88] V. Arabagi, B. Behkam, E. Cheung, and M. Sitti, "Modeling of stochastic motion of bacteria propelled spherical microbeads," *Journal of Applied Physics*, vol. 109, p. 114702, 2011. 3.4.3

[89] C. Brennen and H. Winet, "Fluid mechanics of propulsion by cilia and flagella," *Annual Review of Fluid Mechanics*, vol. 9, pp. 339–398, 1977. 3.4.3

[90] R. Butt, *Introduction to Numerical Analysis Using MATLAB*. Infinity Science Press, 2007. 3.4.4

[91] B. Qian, T. Powers, and K. Breuer, "Shape transition and propulsive force of an elastic rod rotating in a viscous fluid," *Physical Review Letters*, vol. 100, p. 078101, 2008. 3.6.5

[92] N. Coq, O. du Roure, J. Marthelot, D. Bartolo, and M. Fermigier, "Rotational dynamics of a soft filament: Wrapping transition and propulsive forces," *Physics of Fluids*, vol. 20, p. 051703, 2008. 3.6.5

[93] "Flow control in microfluidics: are the workhorse flows adequate?," *Lab on a Chip*, vol. 8, pp. 383–387, 2008. 4.1

[94] D. Beebe, J. Moore, J. Bauer, Q. Yu, R. Liu, C. Devadoss, and B. Jo, "Functional hydrogel structures for autonomous flow control inside microfluidic channels," *Nature*, vol. 404, pp. 588–590, 2000. 4.1

[95] B. Evans, A. Shields, R. L. Carroll, S. Washburn, M. Falvo, and R. Superfine, "Magnetically actuated nanorod arrays as biomimetic ciliam," *Nano Letters*, vol. 7, pp. 1428–1434, 2007. 4.1

[96] K. Sharp, S. Yazdi, and S. Davison, "Localized flow control in microchannels using induced-charge electroosmosis near conductive obstacles," *Microfluid Nanofluid*, vol. 10, pp. 1257–1267, 2011. 4.1

[97] M. Hagiwara, T. Kawahara, and F. Arai, "Local streamline generation by mechanical

oscillation in a microfluidic chip for noncontact cell manipulations," *Applied Physics Letters*, vol. 101, p. 074102, 2012. 4.1

[98] Y. Kim, S. Joshi, L. Davidson, P. LeDuc, and W. Messner, "Dynamic control of 3d chemical profiles with a single 2d microfluidic platform," *Lab on a Chip*, vol. 11, pp. 2182–2188, 2011. 4.1

[99] S. Miltenyi, W. Müller, W. Weichel, and A. Radbruch, "High gradient magnetic cell separation with macs," *Cytometry*, vol. 11, no. 2, pp. 231–238, 1990. 4.1

[100] R. Molday, S. Yen, and A. Rembaum, "Application of magnetic microspheres in labelling and separation of cells.," *Nature*, vol. 268, no. 5619, p. 437, 1977. 4.1

[101] C. Elkin, H. Kapur, T. Smith, D. Humphries, M. Pollard, N. Hammon, and T. Hawkins, "Magnetic bead purification of labeled dna fragments for high-throughput capillary electrophoresis sequencing," *Lawrence Berkeley National Laboratory*, 2001. 4.1

[102] I. Safarik and M. Safarikova, "Magnetic techniques for the isolation and purification of proteins and peptides," *BioMagnetic Research and Technology*, vol. 2, no. 1, p. 7, 2004. 4.1

[103] V. Kourilov and M. Steinitz, "Magnetic-bead enzyme-linked immunosorbent assay verifies adsorption of ligand and epitope accessibility," *Analytical biochemistry*, vol. 311, no. 2, pp. 166–170, 2002. 4.1

[104] C. Edington, H. Murata, R. Koepsel, J. Andersen, S. Eom, T. Kanade, A. C. Balazs, G. Kolmakov, C. Kline, D. McKeel, Z. Liron, and A. J. Russell, "Tailoring the trajectory of cell rolling with cytotactic surfaces," *Langmuir*, vol. 27, no. 24,

pp. 15345–15351, 2011. 4.3.3

[105] H.-B. Sun, S. Matsuo, and H. Misawa, "Three-dimensional photonic crystal structures achieved with two-photon-absorption photopolymerization of resin," *Applied Physics Letters*, vol. 74, no. 6, pp. 786–788, 1999. 4.3.4

[106] S. Kawata, H.-B. Sun, T. Tanaka, and K. Takada, "Finer features for functional microdevices," *Nature*, vol. 412, no. 6848, pp. 697–698, 2001. 4.3.4

[107] M. Straub and M. Gu, "Near-infrared photonic crystals with higher-order bandgaps generated by two-photon photopolymerization," *Optics letters*, vol. 27, no. 20, pp. 1824–1826, 2002. 4.3.4

[108] K. K. Seet, S. Juodkazis, V. Jarutis, and H. Misawa, "Feature-size reduction of photopolymerized structures by femtosecond optical curing of su-8," *Applied physics letters*, vol. 89, no. 2, p. 024106, 2006. 4.3.4

[109] J.-F. Xing, X.-Z. Dong, W.-Q. Chen, X.-M. Duan, N. Takeyasu, T. Tanaka, and S. Kawata, "Improving spatial resolution of two-photon microfabrication by using photoinitiator with high initiating efficiency," *Applied physics letters*, vol. 90, no. 13, pp. 131106–131106, 2007. 4.3.4

[110] J. Fischer and M. Wegener, "Three-dimensional optical laser lithography beyond the diffraction limit," *Laser & Photonics Reviews*, vol. 7, no. 1, pp. 22–44, 2013. 4.3.4, 4.4

[111] F. Qiu, L. Zhang, K. E. Peyer, M. Casarosa, A. Franco-Obregón, H. Choi, and B. J. Nelson, "Noncytotoxic artificial bacterial flagella fabricated from biocompatible ormocomp and iron coating," *Journal of Materials Chemistry B*, vol. 2, no. 4, pp. 357–

362, 2014. 4.5, 5.1.1

[112] F. Bretherton, "The motion of rigid particles in a shear flow at low reynolds number," *Journal of Fluid Mechanics*, vol. 14, no. 2, pp. 284–304, 1962. 4.4.1

[113] J. Feng, H. Hu, and D. Joseph, "Direct simulation of initial value problems for the motion of solid bodies in a newtonian fluid. part 2. couette and poiseuille flows," *Journal of Fluid Mechanics*, vol. 277, pp. 271–301, 1994. 4.4.1

[114] J. Matas, J. Morris, and E. Guazzelli, "Lateral forces on a sphere," *Oil & Gas Science and Technology Rev. IFP*, vol. 59, no. 1, pp. 59–70, 2004. 4.4.1

[115] B. Ho and L. Leal, "Inertial migration of rigid spheres in two-dimensional unidirectional flows," *Journal of Fluid Mechanics*, vol. 65, pp. 365–400, 1974. 4.4.1

[116] J. Ferziger and M. Perić, *Computational Methods for Fluid Dynamics*. Springer, 2002. 5.1.2

[117] C. Fernández, *stkSolver v1.0 User Manual*. Institute of High Performance Computing, Singapore, 2006. B.3

[118] J. Fischer, J. B. Mueller, J. Kaschke, T. J. Wolf, A.-N. Unterreiner, and M. Wegener, "Three-dimensional multi-photon direct laser writing with variable repetition rate," *Optics express*, vol. 21, no. 22, pp. 26244–26260, 2013. D